NASA Contractor Report 177611

15-2504
p 139

Computation of Rotor Aerodynamic Loads in Forward Flight Using a Full-Span Free Wake Analysis

Todd R. Quackenbush, Donald B. Bliss, Daniel A. Wachspress, Alexander H. Boschitsch, and Kiat Chua

CONTRACT NAS2-13838
October 1990

(NASA-CR-177611) COMPUTATION OF ROTOR AERODYNAMIC LOADS IN FORWARD FLIGHT USING A FULL-SPAN FREE WAKE ANALYSIS (Continuum Dynamics) 139 p

N93-24058

Unclas

G3/02 0159804

National Aeronautics and Space Administration

NASA Contractor Report 177611

Computation of Rotor Aerodynamic Loads in Forward Flight Using a Full-Span Free Wake Analysis

Todd R. Quackenbush, Donald B. Bliss, Daniel A. Wachspress, Alexander H. Boschitsch, and Kiat Chua

Continuum Dynamics, Inc.
P. O. Box 3073
Princeton, New Jersey 08543

Prepared for
Ames Research Center
CONTRACT NAS2-13838
October 1990

National Aeronautics and
Space Administration

Ames Research Center
Moffett Field, California 94035-1000

TABLE OF CONTENTS

Section		Page
	TABLE OF CONTENTS	iii
	NOMENCLATURE	v
1.	INTRODUCTION	1
2.	BACKGROUND ON AIRLOAD PREDICTIONS IN FORWARD FLIGHT	3
3.	FULL-SPAN FREE WAKE MODELING	6
	3.1 Curved Vortex Elements in Free Wake Models	6
	3.2 Representation of Full-Span Wakes	7
	3.2.1 Wake Structure	17
	3.2.2 Filament Release Points	20
	3.2.3 Wake-Induced Velocity Calculations	24
	3.2.4 Vortex Core Modeling and Self-Induction Cutoff Distance Selection	26
	3.3 Far Wake Modeling	27
	3.4 Implementation of Vortex Elements Using ANM	30
	3.4.1 Results of Test Runs	31
	3.4.2 Discussion of Parameter Selection for ANM	35
4.	VORTEX LATTICE MODELING OF ROTOR BLADE AERODYNAMICS	39
	4.1 Background on Vortex Lattice Models	39
	4.2 Outline of the Vortex Lattice Layout Procedure	40
	4.3 Computation of Aerodynamic Loads	43
	4.4 Prediction of Sectional Profile Drag and Profile Torque	45
	4.5 Compressibility	47
	4.6 Stall	48
	4.7 Overlap Near Wake	49
	4.8 Yawed Flow	52

PRECEDING PAGE BLANK NOT FILMED

TABLE OF CONTENTS (Cont'd)

Section		Page
5.	MODELS OF ROTOR BLADE DYNAMICS AND DEFORMATION	55
	5.1 Finite Element Structural Model of the Helicopter Blade	55
	5.1.1 Assumptions	57
	5.1.2 Blade Geometry	58
	5.1.3 Elastic Degrees of Freedom	60
	5.1.4 Derivation of the Element Strains and Stresses	63
	5.2 Derivation of Mass and Stiffness Matrices via Hamilton's Principle	65
	5.2.1 Evaluation of Finite Element Stiffness Matrix	65
	5.2.2 Derivation of the Element Mass Matrix	69
	5.2.3 Assembly of the Global Mass and Stiffness Matrix	71
	5.3 Computation of Modal Properties	74
6.	STRUCTURE AND OPERATION OF THE FORWARD FLIGHT AIRLOADS CODE	75
	6.1 Outline	75
	6.2 Blade Dynamics and Trim Procedure	76
7.	DATA CORRELATION STUDIES	81
	7.1 Objective	81
	7.2 Performance and Trim Calculations	81
	7.3 H-34 Flight Test	90
	7.4 SA-349 Flight Test	91
	7.5 H-34 Wind Tunnel Test	96
	7.6 Contributions of Full-Span Modeling to Airload Calculations	100
8.	SUMMARY	116
	REFERENCES	118
	APPENDIX A	A-1
	APPENDIX B	B-1

NOMENCLATURE

a_o	speed of sound
A	area of cross-section or matrix of blade-on-blade velocity influence coefficients
$\{B_1\}$, $\{B_2\}$, $\{B_3\}$	matrices defined in Eq. 5.14
c	rotor blade chord
c_ℓ	section lift coefficient, $\ell / 1/2\rho\,(U_T^2 + U_p^2)\,c$
C_T	thrust coefficient, $T/\rho\pi R^2(\Omega R)^2$
C_Q	torque coefficient, $Q/\rho\pi R^2(\Omega R)^2$
E	Young's Modulus
f	body force vector due to blade rotation
$\{F^{aero}\}$	nodal forces due to aerodynamic loads
$\{f_{rot}\}$	nodal force vector due to blade rotation
$\{F^{rot}\}$	nodal forces due to blade rotation
$F^{AERO}(i)$	i-th mode forcing term due to aerodynamic forces and moments (defined in Eq. A.10)
$F^{ROT}(i)$	i-th mode forcing term due to forces and moments arising from blade rotation (defined in Eq. A.11)
F	rotational force vector defined in Eq. 5.23a
G	Shear Modulus
[G]	matrix of gyroscopic terms defined in Eq. 5.33
GM(i)	generalized mass for i-th mode
H	shaft axis horizontal force
J_G^m	2nd moment of inertia per unit length about an axis parallel to the blade X-axis and intersecting the local elastic axis.
[K]	stiffness matrix
$[K_{cc}]$, $[K_{cr}]$, $[K_{rc}]$, $[K_{rr}]$	matrix partitions of the stiffness matrix defined in Eq. 5.35
$[K_E]$	material stiffness matrix
$[K_r]$	stiffness matrix terms due to blade rotation
$[K_T]$	stiffness matrix terms obtained from kinetic energy variation
ℓ	length of Finite Element or sectional lift per unit span
L	rotor rolling moment
m	moment vector due to body force defined in Eq. 5.22

$\mathbf{M}$	moment vector defined in Eq. 5.23b
M	Mach number or rotor pitching moment
N	rotor yawing moment
[M]	mass matrix
$[M_{cc}]$, $[M_{cr}]$, $[M_{rc}]$, $[M_{rr}]$	matrix partitions of the mass matrix defined in Eq. 5.35
MRC(i)	contribution to the modal forcing due to unit cyclic pitch acceleration (defined in Eq. A.12)
q	local element degrees of freedom defined in Eq. 5.4
Q	global degrees of freedom for the assembled blade or area integral defined in Eq. 5.25 or rotor torque
$\{r_{\theta_c}\}$	rigid body displacement due to root pitch defined in Eq. A.3
r	radial distance from vortex core center or radial distance along blade span
r_c	vortex core radius
$(r_v)_n$	radial position of nth vortex release point
R	rotor radius or vortex ring radius
$\mathbf{R}$	position vector of point on blade relative to the hub
R_X, R_Y, R_Z	deformation rotations about the X, Y, Z axes respectively
$\bar{r}$	radial centroid of a segment of the trailing wake sheet
SL	segment length
T	shaft axis thrust force
$T_{180°}$, T_Λ, T_γ, T_c	transformation matrices defined in Eq. 5.2
T_{rot}	transformation matrix defined in Eq. 5.3
u,v,w	translations due to deformation along the local x, y, z axes respectively
U,V,W	translations due to deformation along the blade X, Y, Z axes respectively
U_P	flow velocity perpendicular to XY plane
U_T	flow velocity perpendicular to XZ plane
U_∞	free stream velocity in wind axis system
v_θ	vortex swirl velocity
w	downwash velocity

$\mathbf{w}$	vector of downwash velocities at blade control points
W^i	internal virtual work
W_r^e	external virtual work expression due to blade rotation defined in Eq. 5.24
x,y,z	local finite element axes
$\{x_i\}$	vector of nodal displacements associated with the i-th mode eigenvector
[X]	modal matrix (matrix of eigenvectors)
$X_0Y_0Z_0$	blade coordinates of the local axes origin
X, Y, Z	blade axis coordinates
X_S, Y_S, Z_S	shaft axis coordinates
X_w, Y_w, Z_w	wind axis coordinates
Y	shaft axis side force
α_g	geometric angle of attack
α_e	blade section effective angle of attack
α_s	rotor shaft angle of attack
β	blade rigid flap angle or compressibility stretching factor or angle between the local y and η axes
γ	anhedral angle
$\boldsymbol{\gamma}$	vector of bound circulation on the blade or magnitude of vorticity vector in the wake
γ_{xi} , γ_y	vector components of vorticity trailed into the wake
$\gamma_{x\zeta}$, $\gamma_{x\eta}$	shear strains defined in Eq. 5.11
Γ	bound circulation
Γ_i	strength of trailing vortices in Zone i
δ	variational operator
δ_f	fat core size
δ_s	vortex particle spacing
ε_{xx}	longtitudinal strain defined in Eq. 5.11a
ϕ	velocity potential
$\{\Phi_2\}$, $\{\Phi_3\}$	element shape functions defined in Eq. 5.6
$[\Phi]$	shape function matrix defined in Eq. 5.7

NOMENCLATURE (Cont'd)

Φ_i	i-th mode shape
ψ	azimuth angle
Ψ	warping function defined in Eq. 5.12
Λ	sweep angle or yawed flow angle
θ	twist deformation about local x-axis
θ_0	collective pitch at blade root
θ_c	cyclic pitch displacement
θ_{nl}	nonlinear 2^{nd} order torsion term
μ	advance ratio
ρ	air density
ξ	normalized element distance along elastic axis, x/ℓ
σ	vortex particle core size or blade solidity
σ_G	blade mass per unit length (along blade X-axis)
η, ζ	principal axes of the cross-section
$\{\eta\}$	modal amplitude vector
ω_i	i-th mode natural frequency
Ω	rotor angular velocity
$c_{(\bullet)}, s_{(\bullet)}$	$\sin(\bullet), \cos(\bullet)$
$(\bullet)_{,x}$	derivative with respect to the local x axis
$\dot{(\,)}$	time derivative relative to inertial reference frame
$(\,)'$	derivative with respect to azimuthal position [thus the time derivative, $\dot{(\,)} = \Omega (\,)'$]
$\tilde{(\,)}$	Fourier transform

1. INTRODUCTION

Work on the prediction of unsteady airloads on helicopter rotors has been underway for several decades, as documented by References 1-8. One motivation for this effort has been the high level of vibration experienced by rotorcraft in a variety of flight conditions, much of which is caused by unsteady loading on helicopter main rotors. On the whole, it can be said the understanding of the dynamic response of rotor blades to aerodynamic loading is well advanced, while the prediction of the wake-induced velocities that produce this loading is more uncertain. The prediction of the velocity field induced by the rotor wake and the wake-induced aerodynamic loads are the primary topics of interest in the effort described here.

It is axiomatic that the study of helicopter rotor aerodynamics in forward flight is an exceptionally complex undertaking involving most of the major phenomena being studied by modern aerodynamicists, e.g., compressible subsonic and transonic flow, viscous drag, stalled and separated flows, and unsteady aerodynamics. Features of all of these phenomena should be included in a comprehensive model of rotor aerodynamics. However, it was not judged desirable to attempt to include the state-of-the-art treatments of all of these issues within this analysis, since such treatments often involve direct integration of the primitive equations of fluid mechanics (e.g., the Euler or Navier-Stokes equations) and so typically require exceptionally large computational capabilities. Such an approach would have defeated the primary purpose of this effort: the development of an analysis of rotors in forward flight that not only represents a substantial improvement in the refinement of rotor wake modeling but is also usable in the near term as a research tool in support of design efforts in the rotorcraft industry.

As will be made clear in the discussion to follow, the primary technical focus of the present work has been the implementation of an advanced model of the vortex wake for use in a general analysis of helicopter rotor aerodynamic loading in forward flight. This model features a novel discretization of the wake into filamentary vortices representing constant-strength contours of vorticity in the vortex sheets that trail from each blade. This approach automatically captures the wake of the full span of the rotor blade and so contains structures absent from earlier, more simplified models. The new full-span wake model is also noteworthy in that it eliminates the artificial distinction between vorticity generated by azimuthal and spanwise changes in the bound circulation on the blade (i.e., between what is conventionally termed "trailed" and "shed" vorticity) and in that it provides a visually meaningful representation of the wake.

The wake model itself has been constructed in a sufficiently general fashion to capture the full semi-infinite wake of the helicopter rotor, and includes efficient and accurate calculation of far wake effects. The computation of aerodynamic loads in the presence of the wake-induced flow field is carried out using a vortex lattice model of the blade. This model is appropriate for rotor calculations because of its potential for refined treatment of tip effects and wake/blade interaction. In addition, the study of helicopter blade loading is a classic example of a truly aeroelastic calculation, and so an appropriate treatment of the dynamics of the rotor blade is particularly important. It was not the intention of the present effort to break new ground in the analysis of rotor blade dynamics, so the model developed here includes the implementation of a finite element analysis of blade structure drawn largely from the existing literature on structural dynamics. The resulting coupled analysis of vortex wake dynamics, unsteady blade loading, and blade deformation is suitable for application to isolated rotors in steady forward flight.

Given the focus of the present work, the Computation of Rotor Aerodynamics in Forward Flight, the complete analysis has been dubbed RotorCRAFT. This report discusses the fundamental work that was carried out to support the development of the initial version of RotorCRAFT and documents the model as it currently exists. It opens with a brief review of background information and literature on the prediction of forward flight airloads, providing the motivation for the development of the full-span free wake model that forms the heart of the RotorCRAFT analysis. The following section discusses the principles of the wake model and the major features of its implementation. Along with this is a description of the implementation of a new class of vortex wake elements based on Analytical Numerical Matching (ANM), elements that offer the promise of substantially increased efficiency with no sacrifice in accuracy relative to the Basic Curved Vortex Elements (BCVEs) currently implemented in the model.

The subsequent discussion outlines the application of vortex lattice methods to aerodynamic load calculations and the implementation of the finite element model of blade deformation. The remainder of the report focuses on describing the structure and operation of RotorCRAFT and its performance in a variety of correlation studies which were aimed at evaluating the code's success as a computational tool for the analysis of aerodynamic loads. The discussion of these results will point out the advantages gained through the application of full-span wake modeling to rotor loads prediction and will note the features of the analysis requiring further development.

2. BACKGROUND ON AIRLOAD PREDICTIONS IN FORWARD FLIGHT

Miller (Ref. 1) discussed many of the sources and consequences of vibratory airloads in helicopters, noting that the higher harmonic components of downwash persist even in high speed flight, contrary to the trends predicted by models based on uniform downwash. He also pointed out the importance in capturing wake distortion so as to properly account for unsteady loading in both low and high speed flight. Scully (Ref. 2) developed a free wake analysis of the rotor using two free filaments (a rolled-up tip vortex and a diffuse inboard filament) to model the rotor wake. This distorted wake model succeeded in capturing certain features of the unsteady loading on rotors in a variety of flight conditions, though uncertainties about the proper modelling of close blade/wake interactions precluded accurate prediction of higher harmonic loads. Other broadly similar wake models have been developed over the last fifteen years (e.g., the work of Egolf and Landgrebe, Ref. 3, Sadler, Ref. 4, and Johnson, Ref. 5).

The seminal paper of Hooper (Ref. 6) pointed out the inadequacy of these types of models in predicting the nearly impulsive airloading events that occur in a broad range of rotor designs, particularly in high speed flight. Hooper considered data for flight conditions at both low and high advance ratios. He concluded that the major features of vibratory loads at low forward speed could be predicted using relatively simple models involving the oblique interaction of blades with straight line vortices. However, the high-speed cases proved to contain features requiring substantially more advanced modeling techniques. Hooper showed that several ostensibly dissimilar rotors shared a strikingly similar loading pattern and that in several cases the higher harmonic airloading was dominated by a relatively discrete event near the blade tip on the advancing side. During such interactions the blade experiences a sharp upward, and then downward, load fluctuation. This up-down pulse, which is clearly an important contributor to the overall higher harmonic airloading, appeared to be due primarily to aerodynamic interaction with the wakes produced by previous blades. Hooper also documented the inability of conventional rotor wake models to compute the behavior observed in the experimental data, a result suggesting that some aspects of the traditional approach to rotor wake aerodynamics must be inadequate, at least for the high speed case. Recent work by Miller (Ref. 7) and Johnson (Ref. 8) has been directed toward repairing some of the shortcomings in previous single-tip-vortex models.

Any wake model designed to address the issue of higher harmonic airloading must be sufficiently detailed to capture the important details of the loading experienced by rotor blades. Figure 2-1 shows that rapid, complicated load variations occur on the advancing side. Around $\psi = 90^\circ$ there is a region of negative load at the tip, and a relatively gradual spanwise load variation, with the maximum load shifted far inboard. The advancing blade experiences a rapid decrease in loading as it enters this region and a rapid load increase upon leaving it. These load variations generate a complex wake field which is encountered by the following blades. Strong trailed (streamwise) and shed (spanwise) vorticity components are present in this incident wake field. Vorticity of opposite sign is generated by the negative loading near the tip of the generating blade, resulting in a negative sign tip vortex. The usual positive sign tip vorticity is also present but is shifted inboard. Because of the more gradual radial load variation, there is insufficient time for this positive sign sheet to completely roll up before encountering the following blades.

Clearly, in view of this loading pattern and its likely source, a new treatment of the wake is necessary if rotor unsteady airloads are to be adequately predicted. The technical approach to be described below utilizes a refined analysis of the near wake that extends

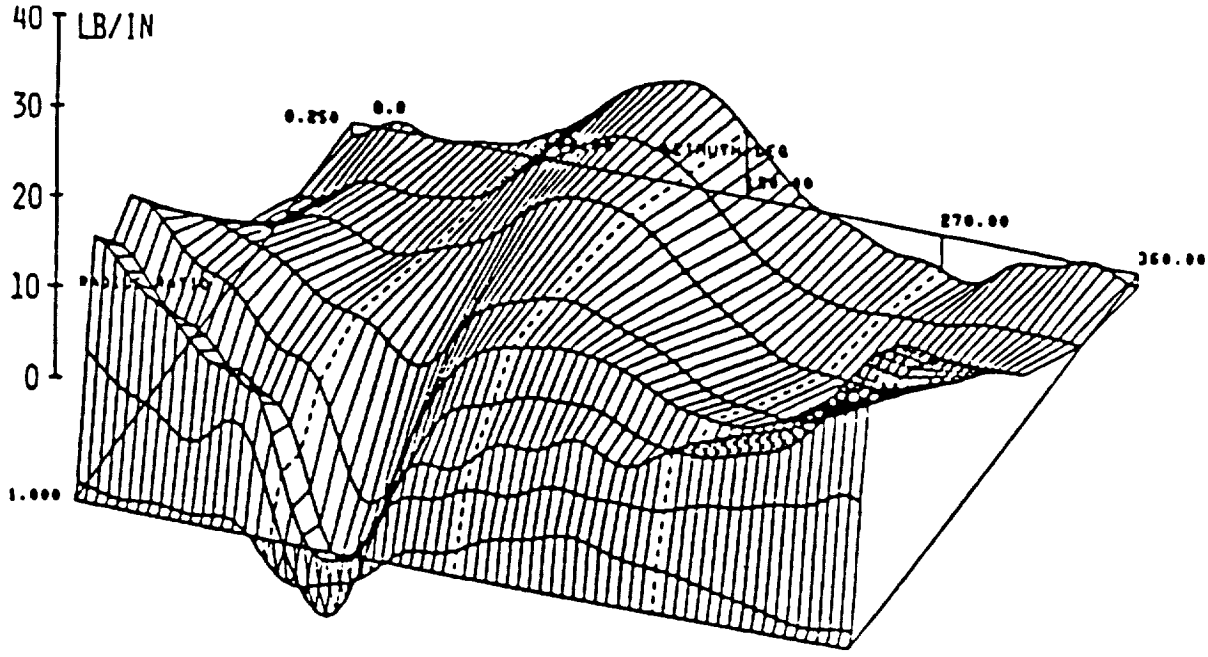

a) Harmonics 0 - 10.

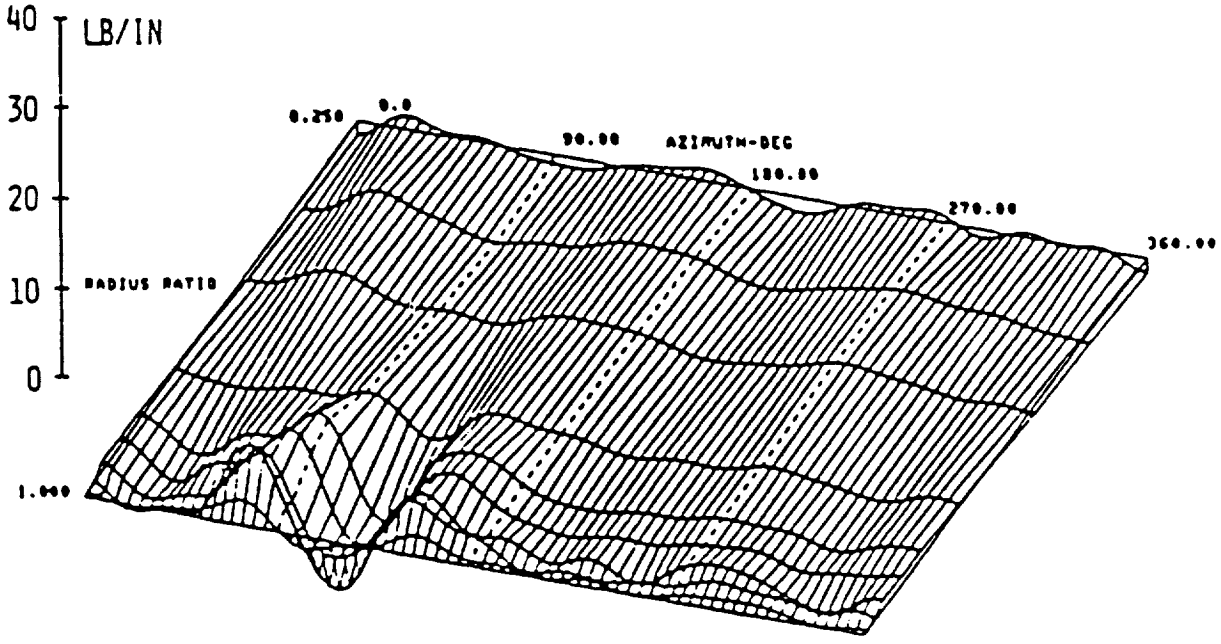

b) Harmonics 3 - 10.

Figure 2-1. Linear surface plots of aerodynamic load distribution on the H-34 main rotor at advance ratio 0.39 (from Ref. 6).

beyond the first few interactions with following blades. This analysis predicts the convective evolution of the actual wake structure, and the approach is based on calculating, rather than modeling, the actual wake flow field. For this reason, the analysis is designed to accommodate a rather general description of the wake. The wake structure accounts for the effects of spatial and temporal load variations on the generating blade. Preliminary development of these concepts is described in References 9-17, which contain very promising initial results on the predictions of the vibratory airloading of rotors, as well as discussion of fundamental tools for rotor wake analysis. The work described in References 12 and 13, which originated as part of the Boeing Helicopters research program, was of particular importance in demonstrating the applicability of the general approach used here to the prediction of rotor airloads in high speed flight.

It is important to note, though, that despite its importance to the prediction of helicopter vibration, the issue of high frequency airloading cannot be considered in isolation. The complete aerodynamic load calculation on the rotor - including the coupling to performance, trim, and blade dynamics calculations - must be considered as a whole. For this reason, this report goes considerably beyond previous exploratory work and addresses integrated and low-frequency rotor loading in substantial detail, as is appropriate for a general analysis of rotor aerodynamics. Indeed, though Hooper's discussion in Reference 6 correctly notes that the fundamental mechanisms leading to vibratory loads in transition flight at low advance ratio have been reliably identified, the predictive capability of current rotor aerodynamic models in this regime is at best fair, as was made clear by a comprehensive review paper by Harris (Ref. 18) as well as more focused studies of low-speed rotor behavior (e.g., Ref. 11). Thus, the discussion that follows will emphasize the full spectrum of rotor loads calculations and will include correlation studies with rotors in a broad range of flight conditions, in addition to the high-speed cases described above.

3. FULL-SPAN FREE WAKE MODELING

This section describes two of the principal computational tools used in the wake simulations featured in this report: curved vortex elements and the novel full-span wake model. The application of curved elements is briefly reviewed, followed by a discussion of the representation used for the complex wakes characteristic of forward flight. The model described here is based on the same fundamental ideas as the forward flight wake model outlined in Reference 12, but has been radically altered and extended by several major subsequent modifications. These modifications, documented in part by References 14 and 15, include the addition of a vortex lattice blade model, a more consistent wake evolution scheme, implementation of a far wake model, and a coupling to a flexible finite element structural model, as well as a variety of additional features developed during the current effort.

In addition, the current wake model takes advantage of recent work by Bliss and Miller (Refs. 16 and 17) in the development of exceptionally efficient techniques for the prediction of vortex-induced flow fields in free wake calculations. This work, which involves the application of a technique known as Analytical/Numerical Matching (ANM), has resulted in the development of methods for the prediction of vortex-induced velocity fields that are in many ways superior to the curved element model implemented in the earlier versions of the RotorCRAFT analysis. While not yet sufficiently mature to replace wake models based on curved elements, the ANM wake model is available as an option within RotorCRAFT. For completeness, the fundamental features of the entire free wake flow field model are now briefly reviewed, including discussion of curved vortex elements, full-span wake modeling, and ANM.

3.1 Curved Vortex Elements in Free Wake Models

The purpose of a free wake analysis is to simulate in detail the actual shape and motion of the wake of each rotor blade treated as a free vortex flow. The wake is represented by vortex filaments trailed from the blades, and each trailing filament is composed of a string of individual vortex elements connected at collocation points. The velocity field of these individual vortex elements is determined through numerical evaluation of analytical expressions for the velocity field of these elements. The Biot-Savart integration for the overall wake velocity field is evaluated numerically by summing the contributions of the individual elements. In conventional free wake analyses like that described in References 10 and 11, the convection of these points over a small time interval, corresponding to an increment of rotor rotation, is determined at each step given this velocity field. The vortex elements are then repositioned between the new collocation point locations and the calculation procedure is repeated. The process can be considered converged when the results are repeatable from one rotor revolution to the next.

Two types of vortex elements are required to implement a free wake analysis. The first type of element is used to evaluate the velocity induced at any point in the flow field, except points on the element itself. Traditionally, straight-line elements have been used for this purpose (see for example Refs. 2-5). An alternate approach was developed using a more sophisticated curved element (Refs. 9-11). This element is referred to as the Basic Curved Vortex Element, or BCVE. A second type of element is used only to evaluate the velocity induced by the element on itself. This element is called the Self-Induction Vortex Element, or SIVE. Curved elements have previously been applied to work on the wakes of hovering rotors as well as simulations in low- and moderate-speed forward flight (Ref. 11). Reference 10 also contains a discussion of the gains in efficiency and accuracy that

are realized when curved elements are used in place of straight-line elements. The documented success of curved elements in wake modeling is an important facet of the forward flight wake model described in this report.

Figure 3-1 shows a typical BCVE, depicting the local coordinate system associated with it as well as its parabolic shape. For such a parabolic shape, the functional form of the Biot-Savart law that is integrated over its length to compute the velocity field is such that it can be solved analytically; this circumstance permits a very favorable tradeoff to be made in accuracy and computation time when calculations using BCVEs are compared to ones involving straight line elements. Figure 3-2a shows several methods for joining BCVEs together to form the continuous vortex filaments that are the building blocks of most current Lagrangian free wake models. At present, the "interpolated point" method is used, and the geometry of the filaments at any instant is determined by passing overlapping arcs between the existing collocation points. Also evident in Figure 3-2b is the circular arc SIVE that computes the velocity field in the immediate vicinity of the collocation points themselves. The construction of vortex filaments using BCVEs and SIVEs is discussed in detail in Reference 10.

3.2 Representation of Full-Span Wakes

This section outlines the full-span wake model that forms the heart of the RotorCRAFT analysis. As discussed in Section 2, a complex wake model is needed in forward flight since the time-varying loading experienced by rotor blades generates both trailed and shed vorticity components in the wake. For reference, note the typical experimental result for aerodynamic load variations that are experienced by a rotor blade in high speed flight as shown in Figure 2-1. An idealized sequence of advancing side load distributions containing this behavior is sketched in Figure 3-3. A corresponding sequence of bound circulation distributions would exhibit similar behavior. Spanwise variations in the bound circulation are responsible for the "trailed" component of wake vorticity and temporal (i.e, azimuthal) variations are responsible for the "shed" component.

Assume that the bound circulation distribution along the span of the rotor at any azimuth angle ψ can be represented as $\Gamma(r,\psi)$, where r is the radial distance along the blade span. The wake that trails from the blade consists of a continuous sheet of vorticity whose strength as it leaves the blade is $\gamma(r,\psi)$. The vorticity in the wake is a vector quantity, and can be represented by

$$\vec{\gamma} = \gamma_x \hat{i} + \gamma_y \hat{j} \tag{3.1}$$

where x and y are defined parallel to the span and to the chord of the blade, respectively. The intensity of each component of vorticity is related to the bound circulation by

$$\gamma_x = \frac{-\partial\Gamma(r,\psi)}{\partial t} \tag{3.2}$$

and

$$\gamma_y = \frac{-\partial\Gamma(r,\psi)}{\partial r} \tag{3.3}$$

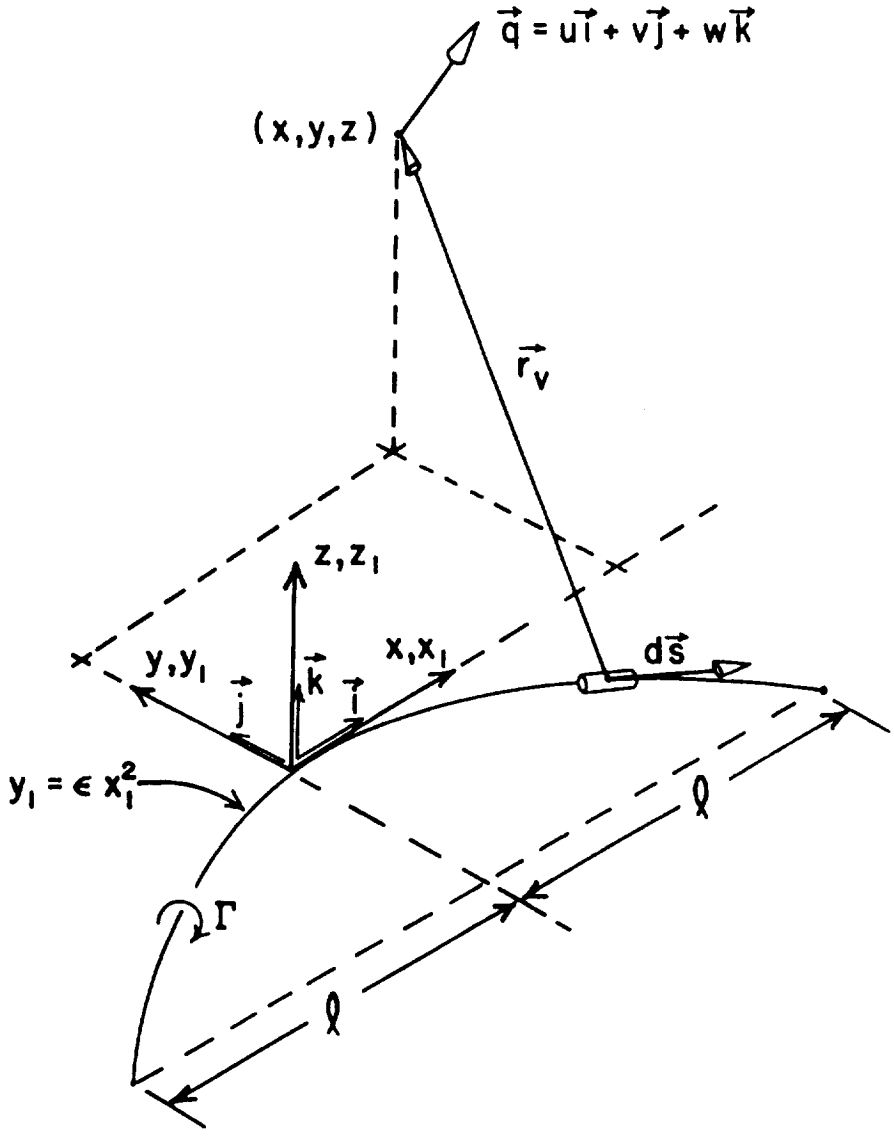

Figure 3-1. Geometry for the Biot-Savart integration over a parabolic arc.

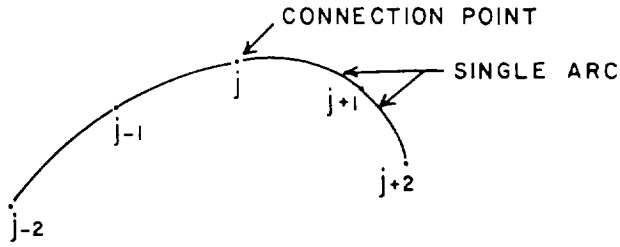

END-TO-END CONNECTION METHOD

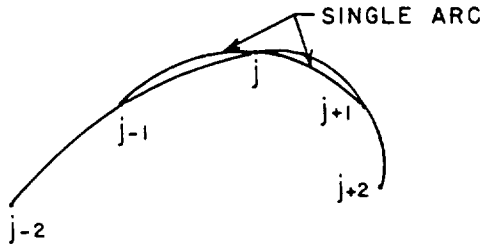

OVERLAPPING ARCS METHOD

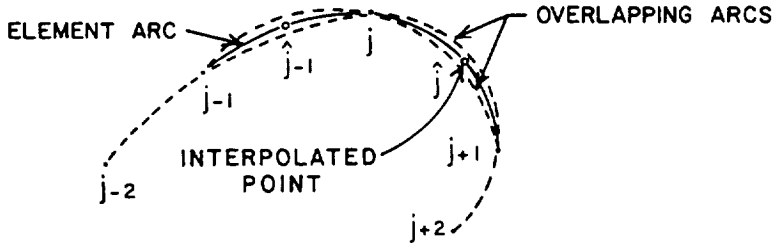

INTERPOLATED POINT METHOD

Figure 3-2a. Connection methods for curved vortex elements.

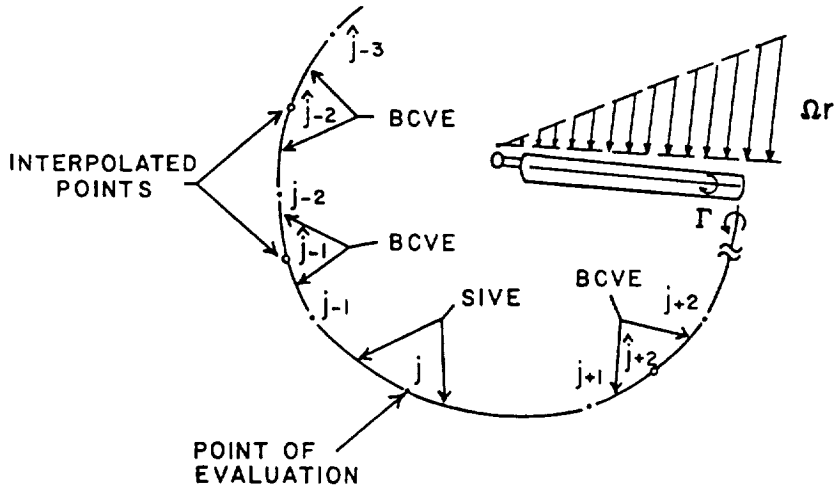

Figure 3-2b. Typical arrangement of elements to calculate the self-induced velocity at point j .

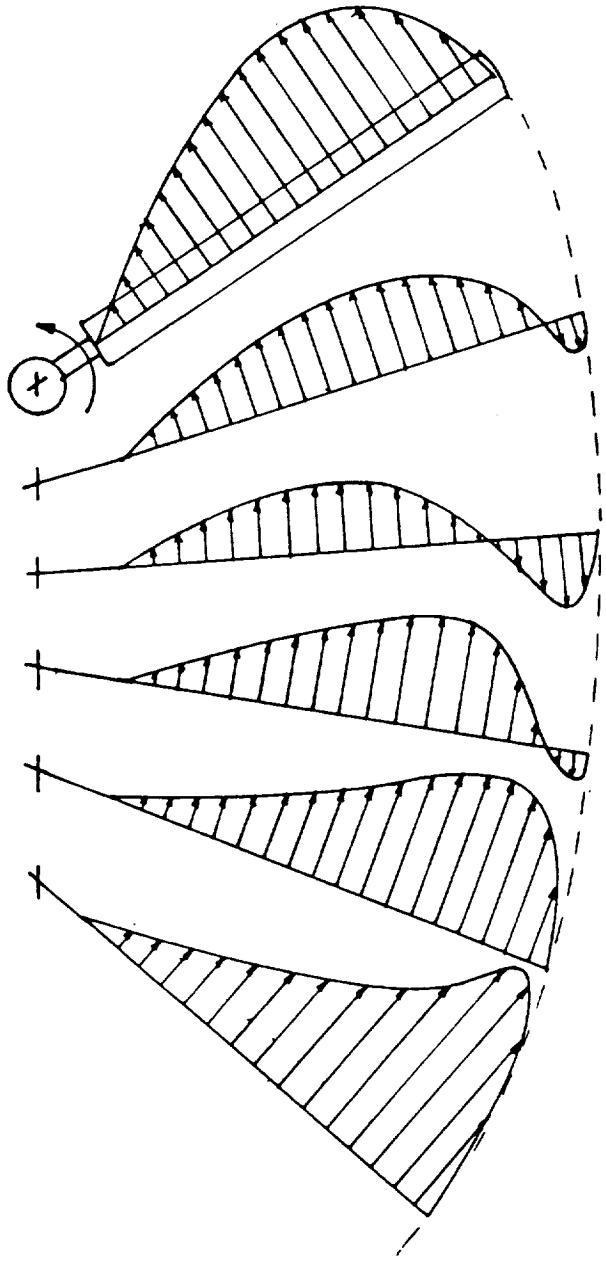

Figure 3-3. Typical load variations on the advancing side in high speed flight.

while the magnitude of the vector is determined by

$$\gamma = |\vec{\gamma}| = \sqrt{\gamma_x^2 + \gamma_y^2} \tag{3.4}$$

Note that the strength of the wake sheet may be zero and that each component may reverse sign depending on the strength and rate of change (spatial or temporal) of the bound circulation.

Figure 3-4 shows the idealized wake vorticity field corresponding to the load variations in Figure 3-3. The wake here is shown in terms of contours of constant sheet strength, i.e. lines of constant γ are depicted. (Note that for the current discussion, the distortion of sheet due to wake on wake interaction is ignored and the wake is assumed to lie in a plane; this situation is well approximated by a rotor in high speed forward flight). Clearly, only a finite number of contour lines are used in this figure, though a continuum of lines are in fact required to completely represent the wake sheet. Because increments in γ are constant between each contour line, the amount of circulation contained between any two contour lines on the sheet is constant. This circulation is related to the bound circulation on the blade as follows:

$$\Delta\Gamma = \int_r^{r+\Delta r} \gamma(r,\psi)\, dr = \Gamma(r+\Delta r,\psi) - \Gamma(r,\psi) \tag{3.5}$$

The contour lines may come together to form a closed loop, but other than this the total circulation between any two lines will remain constant throughout the wake.

One consequence of this is that if the origination points of contour lines (denoted "release points" in the discussion below) are spaced radially along the blade corresponding to fixed increments in bound circulation, then the radial distance between the contour lines will be a direct measure of the gradient in bound circulation along the blade. That is, since $\Delta\Gamma$ is a constant, the approximate relationship

$$\frac{\partial\Gamma(r,\psi)}{\partial r} \cong \frac{\Delta\Gamma}{\Delta r(r,\psi)} \tag{3.6}$$

means that filament spacing will be inversely proportional to spanwise circulation gradient. (Here, Δr is the radial spacing between contour lines as they leave the blade.) Thus, contour lines will be tightly spaced in the radial direction where gradients of bound circulation are high, as is typically true near the blade tip at most azimuth angles. As Figure 3-3 makes clear, however, realistic blade load variations do not always produce large bound circulation gradients near the blade tips. Gradients are often shallow at the advancing tip in high speed flight, and so the wake may take on a more sheetlike character, rather than rolling up into a concentrated tip vortex. Conversely, bound circulation gradients may not always be shallow in certain regions. Note in particular that the radial gradients near the blade root may be relatively large compared to the weak gradients typically seen in the inboard loading distribution of hovering rotors. Thus, unlike the diffuse inboard wakes usually present on rotors in hover, concentrated vortical structures may be present trailing from the root region on rotors in high speed flight.

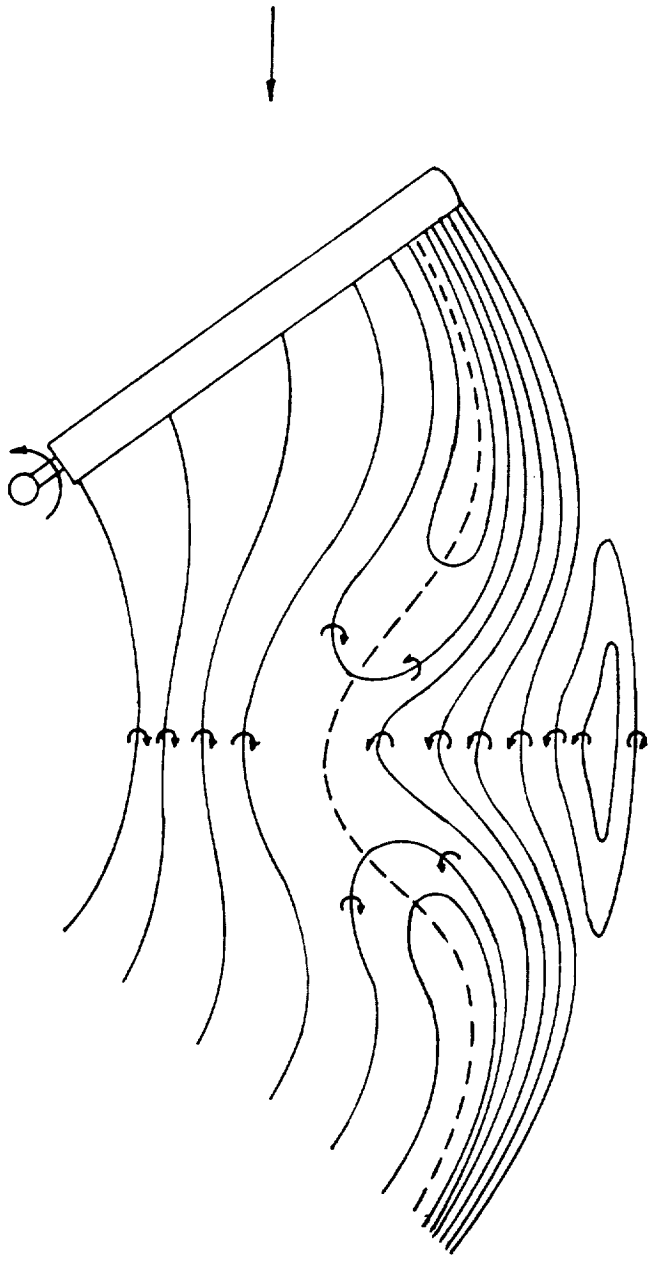

Figure 3-4. Contours of constant sheet strength in the wake on the advancing side.

Note that the tangent to the contour line at any point determines the direction of the local vorticity vector $\vec{\gamma}$. Often, the terms "trailed" and "shed" vorticity are used in describing the wake, the former to denote vorticity trailed due to spatial (radial) gradients in bound circulation and the latter to denote vorticity due to temporal (azimuthal) gradients. As should be clear from the discussion to this point, these two quantities are in fact components of the resultant vector $\vec{\gamma}$. Clearly, it is desirable to employ a wake discretization that removes the artificial distinction between these two quantities and treats the vector vorticity field in a unified manner.

In principle, one could achieve this end by discretizing the wake into continuous sheet elements, but this has proved awkward in the past (Ref. 2); curved sheet elements that could smoothly capture the distortion of the wake sheet are computationally inefficient, while simpler flat sheet elements tend to develop kinks and gaps. Another possible representation of the wake sheet is a lattice of discrete shed and trailed vortex elements (see, for example, Ref. 4) as shown in Figure 3-5. This lattice is typically constructed by trailing mutually perpendicular straight line vortex elements from the blade, elements parallel to the blade span to account for the x component of vorticity, while elements perpendicular to the span capture the y component. The trailing components have an azimuthal extent of $\Delta\psi$, while the length of the shed components is determined by the radial spacing of the vortex lattices on the blade. This approach has been used previously to calculate the near wake downwash on the generating blade (Refs. 4, 19, and 20). By extending the lattice far enough downstream, the wake interaction with subsequent blades can also be simulated. In fact, a lattice representation using curved vortex elements could be considered for use in a free wake treatment. However, in a free wake analysis this approach seems unnatural, in part because it preserves the artificial distinction between shed and trailed vorticity noted above. In addition, the effect of discretized shed components on the roll-up of the trailed components is open to question.

A wake model built on the contours of constant wake vorticity is preferable. Several interesting features of the wake vorticity field are apparent, in addition to those already cited. First, note that the radial location of the release points of the constant contour lines changes in accordance with the varying bound circulation distribution. Also, consider the path of the "zero contour" line that trails from the locations of the maximum values of bound circulation at each azimuth (the locus of these maxima are shown with a dashed line in Figure 3-4). When the magnitude of this maximum value changes by an amount larger than the increment of circulation $\Delta\Gamma$ between the contour lines, the lines on either side of this maximum line must come together to form loops. The loops across the maximum line in Figure 3-4 are a consequence of decrease and subsequent increase in the maximum load (and bound circulation) sketched in Figure 3-3.

As well as forming on either side of the line of local maxima on the rotor blade, loops may form around local minima as well. Consider the loading pattern sketched in Figure 3-3. There, the negative bound circulation that appears and then disappears near the tip leads to the formation of the set of elongated closed contours seen in the tip region in Figure 3-4. The number of loops is roughly

$$N_{loop} \cong \left| \frac{\Gamma_{min}}{\Delta\Gamma} \right| \tag{3.7}$$

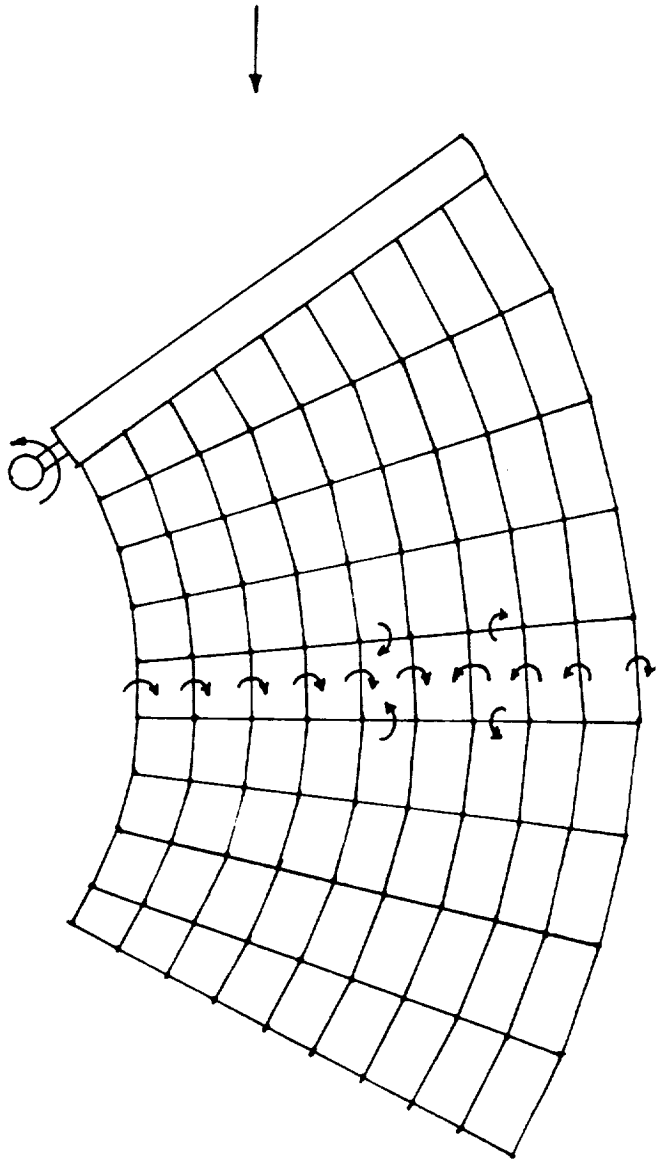

Figure 3-5. Modeling the trailed and sheet vorticity by a lattice of vortex elements.

The precise integral number of loops trailing from this tip region will of course be a function of the discreteness of the contour representation.

The discussion to this point has focused on the qualitative behavior of vortex sheet strength contours trailing from the blade, but has not explicitly defined a method for carrying out practical wake calculations. The first step in motivating this model is to recall that the contour lines can in fact be treated as vortex filaments. The natural step to take in representing the wake is thus to lay down curved vortex elements along the contours of constant wake strength, as shown in Figure 3-6. To conserve circulation in the wake, these filaments are assumed to contain all of the rolled-up vorticity trailed between adjacent release points. This means that all of the filaments will have equal strength $\Delta\Gamma$, and the filaments have constant strength along their length.

The shed and trailed vorticity is thus accounted for by the fact that the direction of the tangent vector to the resultant elements changes continuously even though the strength of each filament is constant . Using this approach, on the average only half as many elements are required as in the straight-line lattice method, where the local vorticity vector is represented by two discrete straight elements. Thus, the use of curved elements means that fewer, relatively large elements can be used to accurately represent the contour shapes. These factors give the full-span free wake model based on curved vortex elements a substantial advantage in efficiency relative to the lattice approach; since the model requires roughly half the number of elements, the number of operations required to compute the wake-on-wake velocity field will be reduced by approximately a factor of four. Previous work described in Reference 10 has indicated that the ratio of execution time for wake models using curved or straight vortex elements is

$$\frac{T_c}{T_s} = 3.3 \left(\frac{N_c}{N_s}\right)^2 \tag{3.8}$$

The factor of 3.3 used here was determined by numerical experiments to be the ratio of execution time of BCVEs to straight elements (Ref. 10). Clearly, since a single curved element can replace two straight elements, a constant-contour, full-span wake using curved elements will be more efficient than the straight-line lattice approach since the reduction in the number of elements outweighs the increased computation time required by BCVEs.

As noted above, by choosing each contour filament to be of equal strength the filaments are closely spaced in regions of high circulation, and are widely spaced in regions where the circulation is low. This relationship between filament spacing and sheet strength, and the fact that the filaments follow the actual vortex lines, means that the structure and relative strength of the wake can be seen visually. Since the computational filaments are aligned along the true vortex lines in the wake, this seems to be the most natural and accurate representation of the wake. Also, because the "shed" cross-filaments present in the lattice model are eliminated, an additional discretization along the wake length is not needed and the potential problems of handling these cross-filaments in a free wake representation are avoided.

Once the wake is laid out, the analysis proceeds much as the tip vortex analysis described in Reference 10, except that multiple filaments are trailed from each blade. This inclusion of the wake trailing from the full span of the rotor blade gives this method its most concise and descriptive names, and moreover is one of the most important features of the new model developed here. Subsequent calculations will show the important role played by the wake of the inboard portion of the blade. In addition, this full-span approach naturally allows for the appearance, evolution, and disappearance of the wake of opposite-

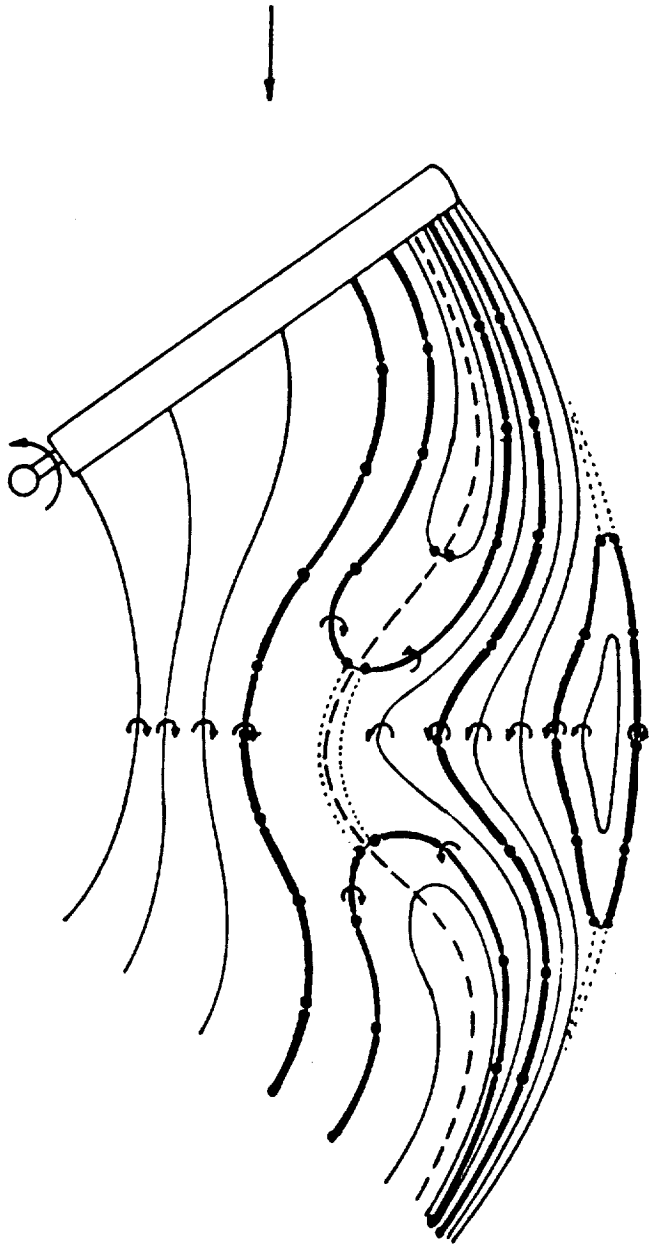

Figure 3-6. Modeling the wake structure with curved vortex elements.

sign circulation zones; such zones are very often present near the advancing tip of conventional rotors (as well as on highly twisted blades - such as tiltrotor blades - in transition flight) and are often critical to the correct handling of wake-induced velocities.

While offering superior efficiency and resolution of the wake structure, this new full-span wake approach does introduce certain differences and difficulties. Two new features of the wake representation that must be addressed are the formation of loops in the wake and the spanwise variation in filament release points as the blade rotates. Handling both of these features requires careful treatment of the numerical logic involved in filament generation and amalgamation.

In its current form, the analysis starts with an estimate of the spanwise bound circulation distribution at a set of azimuthal locations. This distribution can be calculated from a loads analysis, using a simple inflow model, such as the skewed, prescribed downwash of the Drees model described in Reference 21 (see Section 6 for a more detailed discussion of the initialization and operation of the analysis). Typically, the bound circulation is calculated at fixed spanwise stations. The spanwise release points for the individual discrete filaments are found by linear interpolation between these fixed spanwise calculation points. This must be done at each azimuthal station since the circulation distribution changes. Not only do the release points shift along the blade span but some of them also disappear and reappear as the maximum circulation decreases and increases. This disappearance and reappearance corresponds to the formation of loops in the wake.

In the initial versions of this forward flight analysis (i.e., prior to the work of Ref. 14) the bound circulation distribution was assumed to be fixed and did not evolve along with the wake geometry. As of the the publication of Reference 15, the restriction on blade circulation had been removed, though at that time a simple blade dynamics model was in place that precluded fully realistic load calculations. In the current procedure, the free wake evolution provides an updated inflow distribution which is used as input to the vortex lattice model to generate a new bound circulation distribution. This allows a new set of release points to be calculated for further free wake calculations that update the blade loading. An interior iteration is required to find a blade dynamics and trim solution that is consistent with this blade loading. This will be discussed later, along with details of the finite element structural deformation analysis that has been implemented to allow a more complete description of the blade motion.

3.2.1 Wake Structure

The wake is divided into four distinct zones, as sketched in Figure 3-7 (note that the vertical dimension is expanded by a factor of 3:1 in this figure). In Zone 1, filaments trail from the inboard ('positive') circulation distribution; no filaments are trailed from any inboard reverse flow region. Zone 2 filaments trail from the outboard, negative circulation distribution, if one exists at the azimuth in question. Zone 3 is a varying strength vortex pair that represents the circulation downstream of Zone 1, beginning at the end of Zone 1 filaments and extending a specified azimuthal distance downstream. Zone 4 is the same as Zone 3 except that it captures Zone 2 circulation; this zone is rarely important, but is included for completeness.

The filaments in Zone 1 are constant in strength along their length and, moreover, the strength of each filament is equal. Varying circulation strength in the Zone 1 wake is accounted for by increasing and decreasing the number of filaments present, not by increasing and decreasing their strength. For example, if Zone 1 filaments have a

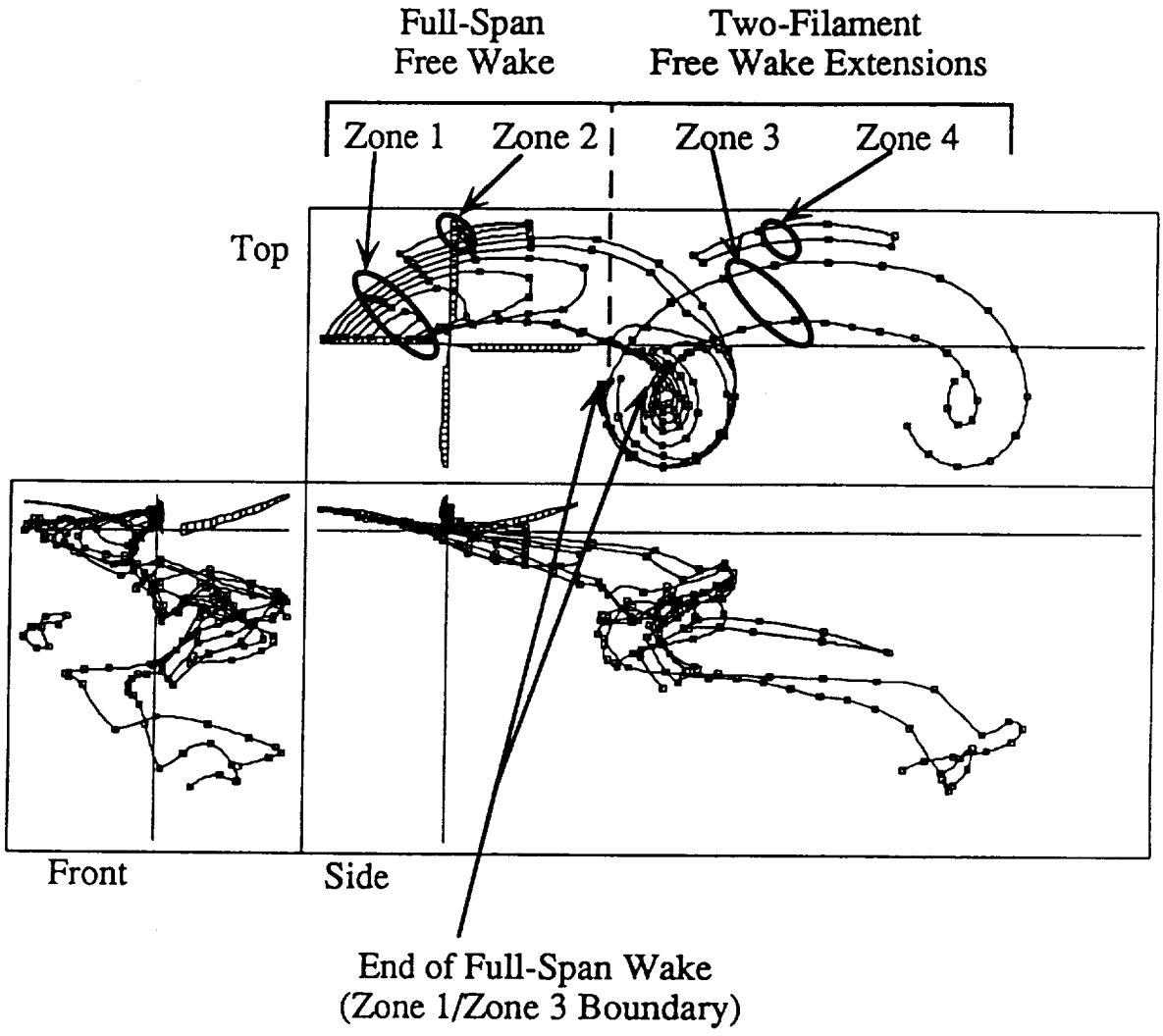

Figure 3-7. Three-view of wake structure trailing from one blade of a four-bladed rotor at advance ratio 0.35 .

circulation strength of 20 ft^2/sec and there is a maximum of 100 ft^2/sec of circulation in the bound circulation within Zone 1 at a particular azimuth, then there will be ten Zone 1 filaments present at this azimuth, five with a strength of -20 ft^2/sec and five with +20 ft^2/sec. Even if the user selected 12 filaments for Zone 1 as input, there will still only be 10 at this azimuth. The other two will appear at azimuths that have greater circulation.

At present, a fixed assumption of the wake layout logic is that the radial distribution of bound circulation consists of a positively loaded region inboard, with the possibility of a negatively loaded zone near the tip at some azimuthal stations. Zone 2 filaments will be created and deleted in the same manner as Zone 1 for those azimuths at which negative tip loading is present. Using this approach for both zones, the filaments represent contours of constant vorticity strength in the wake. This procedure could be extended to accommodate more than two zones, but it was judged that the present arrangement covered a sufficiently broad range of realistic rotor operating conditions for current purposes.

Unlike Zone 1 and Zone 2 filaments, the strength of Zone 3 and Zone 4 filaments vary around the azimuth. Zone 3 contains one varying-strength vortex pair. The strength of the Zone 3 filaments at each location is equal to the maximum circulation at that location. For the example above, the two Zone 3 filaments would have strengths of $\pm$100 ft^2/sec at an azimuthal location with a peak circulation of 100 ft^2/sec. Zone 4 operates in the same manner for the negative tip distribution if it is present.

The filament strengths themselves are determined in the following manner. After an initial estimate of the blade motion has been made (see below), the circulation on the blade as a function of radial position is known at each azimuth. The strength of Zone 1 filaments is then set so that they can account for the maximum circulation that will occur at any azimuth. For example, if the maximum circulation at any azimuth is 100 ft^2/sec and the user has selected 12 Zone 1 filaments (six will be positive and six negative), then the strength of each filament will be $\pm(1.2)(100)/(6) = \pm 20$ ft^2/sec. The factor of 1.2 is introduced to allow for the possibility that the peak circulation will grow as the calculation progresses; lower peak circulations will be automatically accommodated by vanishing filaments and by the formation of vortex loops. This 20% "safety margin" has proved adequate for nearly all calculations to date. Thus, as the solution evolves, this will be enough circulation to account for a peak circulation of up to 120 ft^2/sec. However, if after subsequent evolution of the wake-induced velocity and the blade motion the circulation increases above 120 ft^2/sec then the filament strengths are increased to compensate. Convergence of the wake solution is usually retarded (but not precluded) if such a change in filament strengths occurs. The same procedure is used to determine the filament strengths of Zone 2 filaments based on the (algebraic) minimum negative circulation peak outboard of the inboard circulation peak. The 'outboard' stipulation effectively eliminates the reverse flow region from the analysis.

In general, then, the strength of the filaments trailing from Zone 1 will be

$$\Gamma_1 = \frac{1.2 \max(\Gamma(r,\psi))}{0.5\, N_{1f}} \tag{3.9}$$

where N_{1f} is the maximum number of filaments to be trailed from Zone 1, and $\Gamma(r,\psi)$ is the bound circulation distribution within this zone. (Note that the factor of 0.5 is added since

the total number of filaments that may be trailed from Zone 1 will include an equal number of vortices of opposite sign.) The strength of Zone 2 filaments is determined in exactly the same way. Unlike the filaments in Zones 1 and 2, the Zone 3 and 4 filaments vary in strength along their length. The strength of the Zone 3 filaments at an azimuthal location ψ_0 is

$$\Gamma_3(\psi_0) = \pm \max(\Gamma(r,\psi_0)) \tag{3.10}$$

That is, the Zone 3 filament circulation is set at the maximum value for the bound circulation at the azimuth at which the element was trailed. The circulation strength of the Zone 3 trailers will thus vary around the azimuth; the curved elements within this zone are assumed to vary in strength linearly over their length. The Zone 4 filament strength is defined in an analogous manner. The determination of the vortex strength is, of course, only one part of the wake layout procedure; the specification of vortex release points is addressed in the next section.

3.2.2 Filament Release Points

Filament release points are the points on the blade from which the vortex filaments are released into the wake to account for the vorticity trailed from the blade. Currently filaments are released from the trailing edge of the blade at radial locations that are based on the circulation on the blade and the strength of the filaments. (As will be described later, special provision is made for a so-called 'overlap near wake' that smooths the flow field generated by the vortices in the near wake). Release points vary from azimuth to azimuth because of the temporal variation in bound circulation.

The general formulation for the positioning of release points illustrated can be expressed as follows. Denote the circulation distribution along a blade at a particular azimuth angle ψ as $\Gamma(r)$, the vortex sheet trailed into the wake has strength $-d\Gamma(r)/dr$. Assume for the purposes of discussion that $\Gamma(r)$ is positive across the domain of interest, so that it corresponds to Zone 1 of the rotor blade; the discussion to follow applies equally well to Zone 2, except that the sign of the bound circulation and the circulation in the wake are reversed. Assume also that we examine an interval $r_a < r < r_b$ such that

$$\Gamma(r_b) - \Gamma(r_a) = \Gamma_1 \tag{3.11}$$

where Γ_1 is a specified value of circulation. Γ_1 will be the net circulation around the wake trailed from this region. If the interval bounded by r_a and r_b is sufficiently small, then $\Gamma(r)$ can be assumed to vary linearly within it. In this case, the centroid of the trailing vorticity will be

$$\bar{r} = \frac{1}{\Gamma(r_b) - \Gamma(r_a)} \int_{r_a}^{r_b} r \frac{d\Gamma}{dr} dr = \frac{(r_b + r_a)}{2} \tag{3.12}$$

Moreover, assuming a linear distribution of Γ over this interval implies that

$$\Gamma(\bar{r}) = \frac{\Gamma(r_a) + \Gamma(r_b)}{2} \tag{3.13}$$

Thus, if the vortex sheet trailing from the interval $r_a < r < r_b$ is replaced by a single vortex filament of strength Γ_1, it should be released from the radial location $\bar{r}$ to ensure that both circulation and the first moment of vorticity are conserved; the release point should coincide with the radial location of the mean circulation over the interval.

Figure 3-8 shows a schematic of the release point selection for a representative case that illustrates this procedure at work. This case features eight filaments of strength Γ_1 trailing from Zone 1, while four of strength Γ_2 trail from Zone 2. (Note that Γ_2 is not in general equal to Γ_1). The maximum bound circulation here is $3.5\Gamma_1$. Release points are located at the radial locations along the blade where the circulation strength is $0.5\Gamma_1$, $1.5\Gamma_1$, $2.5\Gamma_1$, and $3.5\Gamma_1$. There are eight release points in all, four on the side of increasing circulation for the negative strength filament trailers and four on the side of decreasing circulation (at positions corresponding to $3.5\Gamma_1$, $2.5\Gamma_1$, $1.5\Gamma_1$, and $0.5\Gamma_1$) for the positive strength filament trailers. The net circulation trailed into the wake is always zero. On the scale shown in Figure 3-8, Γ_2 is half the value of Γ_1, so only two trailers will be released on either side of the negative peak circulation in Zone 2.

In practice, the release point is computed by finding the radial locations at which the bound circulation reaches levels that bound the half-integral multiples of Γ_1 (i.e., $0.5\Gamma_1$, $1.5\Gamma_1$, etc.) and then linear interpolation is used to defined the point inside the interval where the release is to take place. Consider for example the release of the nth filament from the inboard side of the Zone 1 circulation distribution. The bound circulation is in general known at a discrete number of radial positions; assume that two stations r_a and r_b have been identified such that $\Gamma(r_a) < (n + 0.5)\Gamma_1 < \Gamma(r_b)$. Then, the nth release point $(r_v)_n$ is

$$(r_v)_n = r_a + \left[(n+0.5)\Gamma_1 - \Gamma(r_a) \right] \frac{(r_b - r_a)}{\left(\Gamma(r_b) - \Gamma(r_a)\right)} \tag{3.14}$$

For those special cases at the edges of the Zone, the lower bound is taken to be the point at which the bound circulation passes through zero.

As is noted above, this procedure was developed assuming that the bound circulation distribution was piecewise linear, and for good accuracy it is advisable to use a sufficient number of filaments along the span so that this condition is approximated reasonably well. The consequences of using too few filaments are clear from the simple case illustrated in Figure 3-8, since, for example, four trailers with a total of $4.0\Gamma_1$ of circulation strength are trailed from Zone 1, which actually contains a peak circulation of $3.5\Gamma_1$. This discrepancy is clearly related to the use of a relatively small number of trailers, and will vanish as the number of trailers is increased.

Although only a single azimuth station (denoted time step n) is shown in Figure 3-8, the figure nonetheless suggests the mechanism by which filament loops are formed. The loop in the wake of Zone 1 indicates that at time step n-1 ten vortex filaments were trailing

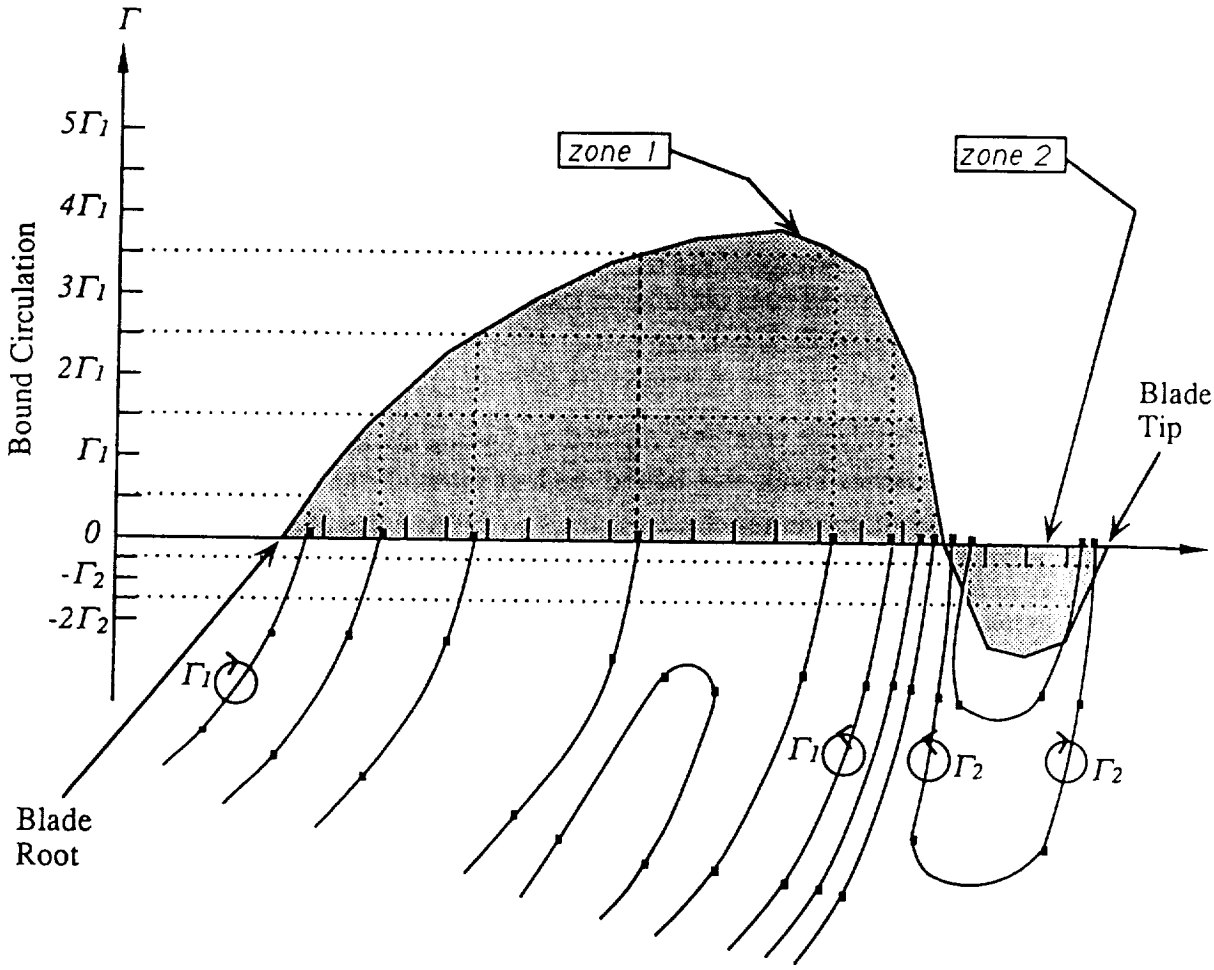

Figure 3-8. Radial bound circulation distribution for a rotor with positive and negative circulation zones, showing the release points of trailing wake filaments.

Γ_1 = filament strength in zone 1

Γ_2 = filament strength in zone 2

from this portion of the blade, and thus the peak bound circulation was in excess of $4.5\Gamma_1$. The decrease of the peak value to level shown in the figure at time step n has caused two release points to disappear and has thus prompted the formation of a filament loop in the wake. Conversely, the structure of the wake of Zone 2 in this figure shows that two release points appeared at time step n-1, indicating that the negative peak circulation passed through $-1.5\Gamma_2$ during this interval, leading to the opening rather than the closing of a loop.

It is possible that a release point location will appear more than twice along the span if the circulation distribution does not increase and then decrease monotonically (i.e., if there are local maxima or minima within the zone). The current analysis was tailored for the case of a bound circulation distribution with a single positive peak and a possible negative peak outboard, and so ignores these variations. Release points are determined by moving outboard from the root of Zone 1 for the side of increasing circulation and moving inboard from the tip of Zone 1 for the side of decreasing circulation. In this way, no release points will be assigned to small 'dips' in the middle of the distribution if they exist. The current programming logic could be extended to take account of such features, but this was not judged to be necessary in the present effort (though this may ultimately be necessary to model fully general load distributions on rotors). Zone 2 release points are done in a manner exactly analogous to Zone 1.

Zone 3 release points do not occur at the blade, but rather at the downstream end of Zone 1 filaments. As discussed above, Zone 3 has two filaments of opposite sign whose magnitude at any azimuth is set by the maximum circulation strength at that azimuth. All the circulation in the wake is rolled up into these two trailing filaments, which are assumed to be filaments with linearly varying vortex strength. In rolling up the full-span free wake in Zones 1 and 2 to form the varying-strength trailers in Zones 3 and 4, the leading points in the rolled-up filaments (sometimes denoted "free wake extensions" in the discussion that follows) are placed at the mean of the distribution of vorticity formed by the downstream ends of the full-span wake filaments. Since all of the endpoints of the Zone 1 trailers should be nearly coplanar, the point representing the mean will lie within this same plane. The root filament of Zone 1 is formed from the amalgamation of the filaments trailing from the inboard half of this Zone. This Zone 3 root filament will start at a point defined by

$$\bar{x} = \frac{2}{N_{1f}} \sum_{k=1}^{\frac{N_{1f}}{2}} [x_v(\psi_0)]_k \qquad \bar{y} = \frac{2}{N_{1f}} \sum_{k=1}^{\frac{N_{1f}}{2}} [y_v(\psi_0)]_k \qquad \bar{z} = \frac{2}{N_{1f}} \sum_{k=1}^{\frac{N_{1f}}{2}} [z_v(\psi_0)]_k \tag{3.15}$$

Here, x_v, y_v, and z_v denote the position of the endpoint of the kth trailing vortex from Zone 1; ψ_0 is the azimuth angle at which the Zone 1 wake terminates. This procedure is repeated for filaments indexed $(N_{1f}/2 +1)$to N_{1f} to form the rolled-up tip filament in Zone 3. Exactly analogous procedures are used to define the starting point of the filaments in Zone 4.

Though this transition to a rolled-up wake can be abrupt in some cases, the flow field experienced by the rotor blades will not be adversely affected if the region of the wake using the full-span trailing filaments is long enough to move the transition point one to two rotor radii from the disk. This is easily accomplished in high speed flight, since the wake is in general convected rapidly downstream of the rotor. Low speed cases will feature closer interaction of Zone 3 with the rotor, but here the wake filaments from Zone 1 - the tip filaments in particular - should already be tightly concentrated by the point where the

transition to Zone 3 takes place. The role and formulation of the wake model in Zones 3 and 4 is discussed further in Section 3.3.

3.2.3 Wake-Induced Velocity Calculations

As the blade rotates, the filament points move from their release points due to contributions from the convection of the free stream, the velocity induced by the vorticity in the wake, and induced velocity from the circulation on the blade. At present, two options are available for treating wake-on-wake interactions in the analysis: allowing such interactions to include the velocity induced by wakes trailed from other blades or to include only the velocity induced by the wake of a given blade on itself. The former is more consistent with the spirit of true free wake analysis, and is the preferred approach at low and moderate forward speeds where wake distortion is very pronounced. The latter, more simplified case is computationally more efficient and is often an adequate approximation for high speed cases.

In either case, the rotor blades experience the velocity field induced by the full rotor wake. As will be described in the next section, a vortex lattice analysis is used to compute the loads on the rotor blade. The velocity induced by the vortex wake BCVE's at the control points within the lattice of vortex quadrilaterals are stored for use in the blade loads calculations (see Section 4). The computation of the wake influence at each of the edges of the vortex lattice is a computationally demanding task if high lattice density is used, and so certain simplifications are invoked, taking advantage of the results of substantial numerical experimentation. If the distance from the BCVE midpoint to the quad control point is greater than five times distance from the edge midpoint to the control point, then the wake-on-blade velocity calculation at that particular edge is bypassed and the velocity at the edge midpoint in question is set equal to the velocity at the control point of the quadrilateral.

A topic of special interest is the computation of the velocity induced by the near wake immediately downstream of the generating blade. The basic model used here involves the replacement of the curved vortex elements that are trailed from the blade with an 'overlap region' that produces a smooth flow field at the blade surface. The wake in the overlap region consists of extensions of the bound trailers that leave the blade and are trailed downstream . The two principal options that exist within the current analysis allow the overlap to consist either of straight trailers that are rigidly fixed parallel to the chord line of the blade or of trailers that move in accordance with the local free stream velocity. Figure 3-9 illustrates a typical configuration of near-wake trailers at four azimuth locations for a rotor at advance ratio 0.4. The change in orientation of the trailers around the azimuth reflects the varying orientation of the effective local free stream. In addition to the alterations in the near wake, a special treatment of the vortex trailers in the overlap region is made in the case of highly yawed flow to correct for tip loads, as will be discussed in Section 4. The technical substance of the overlap model and the model problems carried out to validate it will also be discussed at that point.

In the current overlap model the azimuthal extent of the overlap region may be specified. The overlap is only applied to the wake trailing from the generating blade, i.e. only points of evaluation on the generating blade 'see' the straight trailers in the overlap region. All points of evaluation in the wake or on other blades experience the flow field induced by the full free wake. To an observer on the generating blade itself, the free wake of filamentary trailers begins at the downstream end of the straight trailers; this has the desired effect of smoothing out the discreteness that would otherwise be present if the curved filaments began directly at the trailing edge of the blade.

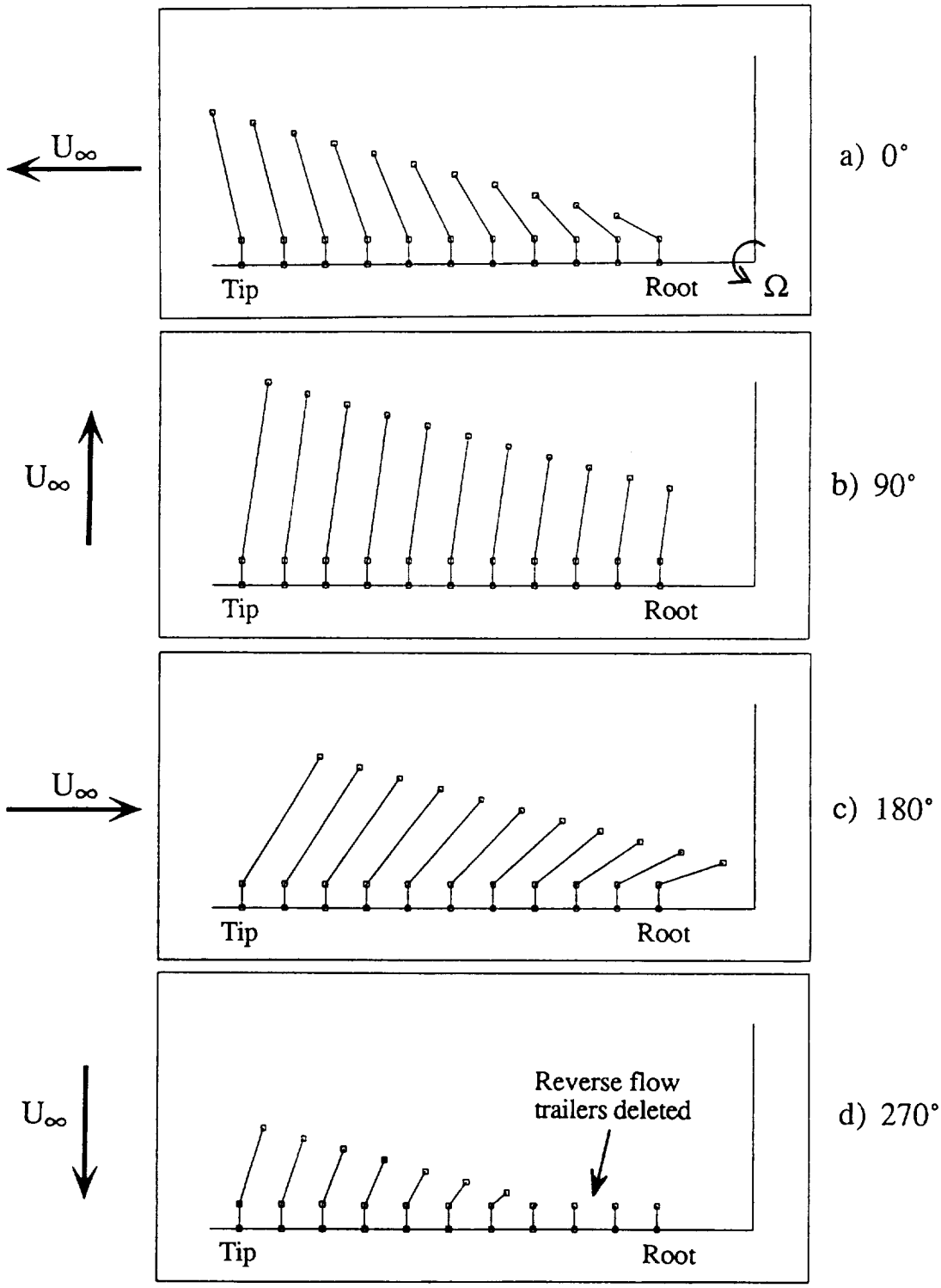

Figure 3-9. Schematic of bound vortex lattice and movable near-wake trailing vortices in the overlap region: four azimuth angles for a rotor at advance ratio 0.4 .

3.2.4 Vortex Core Modeling and Self-Induction Cutoff Distance Selection

As with all Lagrangian wake models incorporating vortex filaments, a vortex core is required to remove singularities from the flow field. Previous investigations (e.g., Refs. 2, 3, and 8) found that load calculations are sensitive to the particular core size chosen. One of the objectives in formulating the current model was to remove as much of this sensitivity as possible. As long as core radius parameters exist within wake calculations, it will be possible to 'dial' or adjust the predicted loads. The discussion that follows is directed at outlining the approach that was taken here to implement a treatment of the vortex core that constitutes a reasonable step towards reducing the modeling role of vortex filament cores.

It is important to appreciate that the full-span free wake model itself contributes substantially to the aim of weakening the modeling role of the core. Alternative models, such as using single free tip filaments, must of necessity use adjustments in the core size to capture flow field effects which are in fact attributable to spanwise and azimuthal loading changes. Since such changes are automatically captured with the current full-span wake analysis, one possible ambiguity has been removed. However, since filamentary vortices are in fact still used, some effective core structure must be imposed to remove the flow field singularities associated with line vortices. The core model used here is the one originally proposed by Scully (Ref. 2); the swirl velocity profile is

$$v_\theta = \frac{\Gamma}{2\pi} \frac{r}{r^2 + r_c^2} \tag{3.16}$$

This constitutes an 'algebraic' core model, which retains half of the vorticity associated with the vortex inside the core radius r_c and leaves half outside. Scully notes that this swirl velocity profile has considerable experimental substantiation. Also, this particular core structure is a convenient choice for the implementation of vortex elements based on ANM, as discussed below.

The issue of the selection of the core radius itself remains. Currently the core radii vary from filament to filament and along filaments from azimuth to azimuth. In keeping with the spirit of the discretization of the wake, which places curved filaments on contour lines of constant strength of the wake sheet trailing from each blade, the local core radius is based on the distance between vortex release points at each azimuth. The core radius becomes the average distance to the neighboring release points on either side (at a given azimuth) with special cases at the root, tip and center of each zone. That is, for filaments numbered n-1, n, and n+1 trailed within Zone 1 or Zone 2, the core size of filament n is computed as

$$(r_c)_n = \frac{((r_v)_n - (r_v)_{n-1}) + ((r_v)_{n+1} - (r_v)_n)}{2} \tag{3.17}$$

At the center, averages are taken between the nearest filament and the maximum circulation line. At the root and the tip, averages are taken using the distance to the blade cutout, blade tip, or the boundary between Zones 1 and 2.

In the current analysis, bounds can be placed on the core size and, if desired, particular core radii can be chosen for each filament. Numerical experimentation has shown that the rotor loading still shows substantial sensitivity if core sizes are adjusted

arbitrarily. However, the primary mode of operation for the correlation runs discussed below was to allow the core radius assigned to each filament to adjust itself to local conditions as outlined above. It is judged that this approach is consistent with the overall aim of removing as much arbitrariness as possible from the analysis of rotor airloads.

In addition to selecting the core properties of the wake filaments, the analysis must also compute an appropriate choice for the cutoff distance associated with the self-induction velocity generated by each filament. The vortex filament dynamics are currently analyzed by integrating the Biot-Savart law over the vortex filaments. This integration is done numerically in the present analysis by breaking the filaments up into simpler vortex elements (BCVE's in this case) whose integrations can be done in closed form, and summing all the element contributions. If a finite-strength vortex filament of infinitesimal cross-section is used, then the Biot-Savart integration is logarithmically singular when the point of evaluation is placed on the curved filament itself. This logarithmic singularity of self-induced velocity is associated with the local curvature of the filament at the point of evaluation. This problem is avoided by stopping the integral at a cut-off distance on either side of the point of evaluation. This approach is handled by a special self-induction vortex element called the SIVE.

Typically, the choice of cut-off distance for a vortex trailing from a wing or rotor blade is obtained from an asymptotic analysis that give results in term of local core size (length scale) and the net swirl and kinetic energy content of the vortex core that must actually exist at the center of the filament. The energy content and core size can be obtained from a detailed knowledge of core structure or, in the case of a tip vortex, by a knowledge of the blade load distribution using a recently developed method (Ref. 22). The latter approach was used in recent work on the prediction of hovering rotor wake geometry and performance (Ref. 23).

The self-induced velocity for the filaments in the current analysis is also handled by a cut-off distance approach, but in this case the cut-off distance is based on the fact that the filaments represent a vortex sheet. It can be shown that a curved segment of the vortex sheet experiences a self-induced velocity, similar in principle to that experienced by a vortex core. A planar, constant strength curved vortex sheet can be shown to have a cut-off distance equal to half the sheet width. The velocity computed using the SIVE element and this cut-off distance applies at the center of the sheet. If the sheet cross-section is rotated 90°, as if the sheet now lies on a cylindrical surface, then there is a change in the cut-off distance. However, the logarithmic dependence in the SIVE formula makes this change insignificant. Therefore, in the analysis, the half-width cut-off distance formula is used as the default choice for all filaments, though other choices can be imposed if desired.

3.3 Far Wake Modeling

The full-span wake described above could in principle be used to discretize the entire rotor wake, but this would be computationally inefficient. Typically three or more full revolutions of free wake are required to obtain an adequate model of wake distortion, while a full semi-infinite wake is rigorously necessary to capture the complete wake-induced velocity field. The high-resolution full-span wake model is required only for the regions where wake-on-blade interactions or careful treatment of wake roll-up is necessary. (For present purposes, the flow field induced on the rotor itself is the primary concern, while in other applications - e.g., the computation of wake-induced flow fields at the tail rotor or empennage - a larger region of full-span wake may be required). Beyond such regions, a simplified model is appropriate, and the discussion above has given some indication of its form. The approach taken is to amalgamate like-sign vorticity trailing from

each of the wake filament zones into single, freely distorting tip and root filaments. As long as this amalgamation (see Figure 3-7) takes place reasonably far downstream of the rotor itself, its effect on the rotor loading will be small.

Presently, the maximum number of filaments that may be trailed from a given azimuth in each of the four wake zones is specified before starting the calculation. This number is ordinarily at least ten, but the useful range can be from six to twenty, depending on the advance ratio and rotor loading. Smaller numbers of filaments can often be used at low speeds, while the complex vorticity field characteristic of high speed flight may require a large number of filaments. The analysis also requires the specification of the number of turns of full-span wake that are to be used and the azimuthal location at which the two-filament wake is to commence. The strength of the rolled-up filaments is adjusted at each azimuthal station to conserve circulation in the wake. This accounts for the effect of the 'shed' component of the vortex wake in the far field. The root and tip filaments in this zone (Zone 3, as discussed in Section 3.2.2) originate at radial positions corresponding to the centroids of the truncated filaments that are trailed inboard and outboard, respectively, of the peak circulation on the rotor blade. These filaments, which will be referred to as 'free wake extensions', distort freely as the calculation progresses.

To complete the analysis of the wake, the free wake extensions must themselves be effectively extended in a semi-infinite fashion; simple truncation of the wake can lead to errors in induced velocity in some flight conditions, particularly at low speed. The far wake model consists of two regions, as shown schematically in Figure 3-10 and is similar to the far wake treatment originated in Reference 10. (It should be noted that a precondition for invoking this far wake model is the presence of at least two full turns of the two-filament free wake extension). The first portion of the far wake consists of a specified number of turns of prescribed wake, turns which duplicate the geometry of the last turn of the free wake extensions. The spacing and orientation of these prescribed turns is set by the average convection over the last two free wake extension turns. The prescribed turns consist of BCVEs, and since their geometry depends on the configuration of the last turns of free wake, this prescribed wake evolves constantly during the free wake evolution.

Given this model for the far wake, the problems to be resolved are the determination of the direction in which the wake is convected, and the development of an efficient method to sum the infinite number of repeated turns of far wake. The mean convection direction is determined by comparing the positions of the last and next to the last turns of free wake. The change in position of each set of corresponding points on these two turns is computed. These position differences between pairs of points, originally generated at the same blade azimuthal location, defines a displacement vector. A running average of all these displacement vectors, generated while stepping the blade through the previous full turn, is computed to determine an average displacement vector. This average displacement vector, $\vec{r}_s$, is taken to represent the average displacement per blade revolution of a wake turn due to overall convection. It is used to orient the successive far wake turns in space. The purpose of the running average over a cycle is to filter out the distortion effects that are superimposed on this mean convection.

Note again the far wake configuration illustrated in Figure 3-10. The far wake can be thought of as being composed of a set of semi-infinite rows of elements running in the direction of $\vec{r}_s$, one of which is shown in the figure. It is possible to sum the contributions of each row in an efficient manner by using a discrete approximation for the Biot-Savart law.)This development is discussed in detail in Reference 10 and will not be repeated here.)

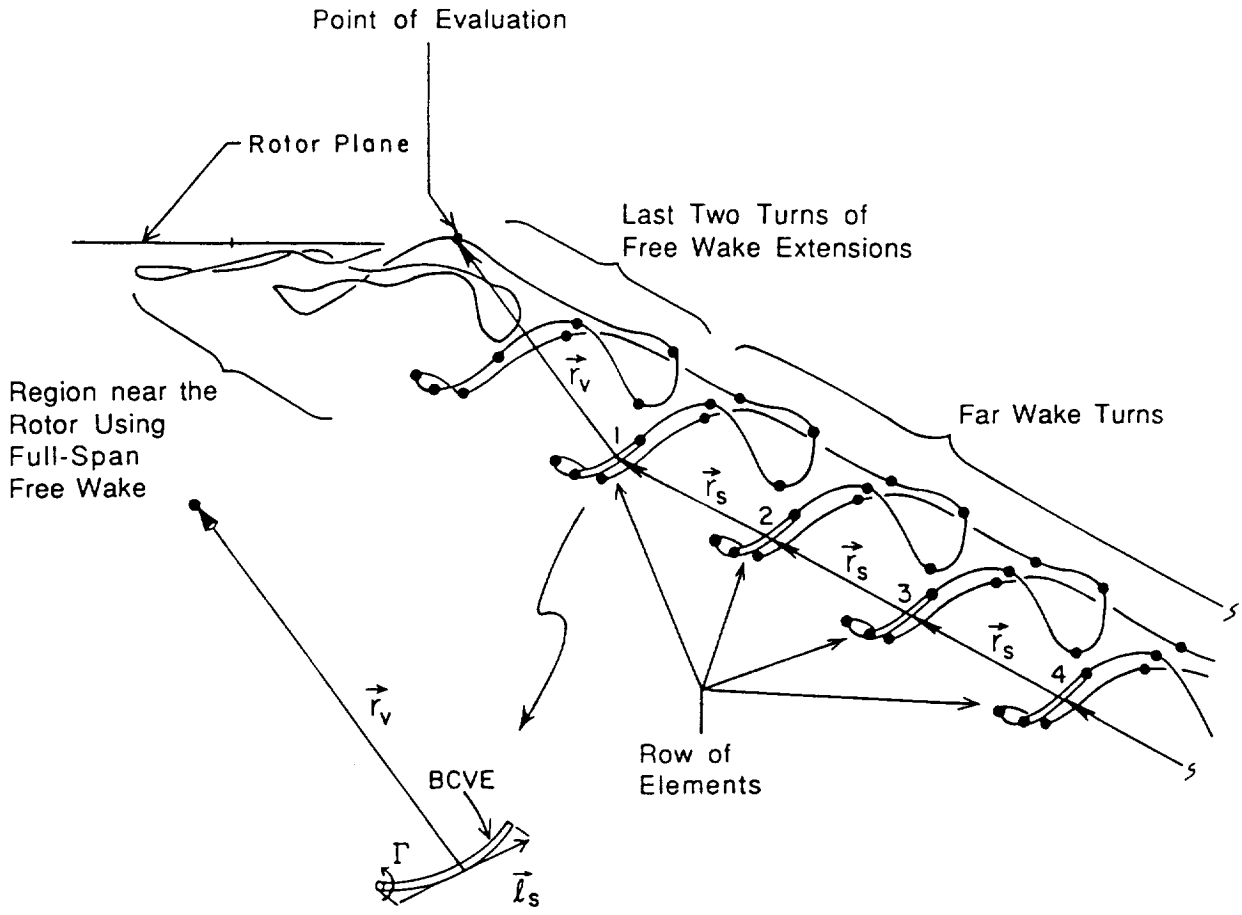

Figure 3-10. Schematic of the far wake model and its coupling to the two-filament free wake extensions.

This intermediate prescribed wake model is based on the idea that the best estimate of the shape of a far wake turn is the shape of the turn of the free wake extensions. Ideally, after each blade revolution, the vortex wake represented by the last turn of the extensions would occupy the position of the first far wake turn. This assumption corresponds to freezing the shape after the last turn of the extensions. The effect of subsequent downstream distortion is, therefore, not included, and only convection in an average sense is taken into account. This approximate shape is best for the first few far wake turns, since there has been relatively little time for subsequent distortion. Neglecting this distortion in the far wake turns that are farther downstream makes little difference since the influence of their detailed shape is less crucial because they are farther away.

The far wake model has been implemented into the RotorCRAFT analysis and has performed in a fashion similar to previous forward flight wake studies (e.g., Ref. 10 and 11). A smooth, stable transition between the end of the free wake and the beginning of the far wake has been achieved. Since the far wake structure is based on free wake information, the far wake shape evolves along with the free wake solution. Note that there is a different far wake shape at each time step in the solution. The far wake configuration also adjusts automatically to the rotor flight condition.

3.4 Implementation of Wake Models Based on ANM

In the free wake analysis of rotors in forward flight or hover, the use of BCVEs has led to considerable success, as is well documented in the literature (Refs. 9-15). The proven robustness and accuracy of the method are direct consequences of its high resolution representation of the filamentary wake vorticity field. However, in some applications, the use of such high resolution, computationally intensive vortex elements everywhere in the flow domain may significantly reduce the efficiency of the method; while a high resolution representation of the vorticity field is required to capture the steep velocity gradient when an evaluation point is in the immediate vicinity of a vortex element, the bulk of the calculations usually involve evaluation points which are in the far field where coarse resolution is sufficient. In this regard, the use of the particle-based "vorton" method can result in considerable savings in computational costs. Because vortons are "clumps" of vorticity concentrated at a single point in space, the algebraic functions associated with the calculation of their velocity field are particularly simple and inexpensive to evaluate.

In the literature, applications of this method to unsteady vortical flow problems have shown promising results (Refs. 24-26). However, convergence studies of the method (Refs. 27-29) indicate that sufficient overlap of the particles must be maintained, i.e. $\delta s = \sigma$, where δs is the spacing and σ is the core size. This requires that a large number of vorton particles be used. For a typical rotorcraft free wake calculation where convective washout of an assumed wake shape is used to obtain converged solution, the order of the calculation is $O(N^3)$, where N is the number of vortex elements, and for a large number of vorton particles, this represents a formidable computational load even with the simple functional form of the individual velocity calculation.

Recently, a new method which incorporates both the accuracy of BCVEs and the efficiency of a vorton method has been developed (Refs. 16 and 17). In this method, referred to as the method of Analytical/Numerical Matching (ANM) , a low resolution far field solution is constructed with a small number of fat vorton particles. The small number of elements limits the computational load to within the capabilities of conventional computing machines while the fat core size assures the mathematical consistency of the scheme. For cases of close approach, where an observation point is in the near field of a

vortex filament, a local analytical correction is applied to capture the high gradient near field solution (Fig. 3-11). Inspired by the method of matched asymptotic expansions, the local analytical correction serves to match the coarse resolution far field solution to the fine resolution near field solution and is composed of two opposite-signed curved arc elements which are fitted locally to the vortex filament. The positive sign arc has the actual physical core size while the negative arc has the fat core and is used to match the fat core particle solution with the thin core arc solution. In principle, any curved arc element can be used for the local correction; for present purposes, however, a closed circular ring is chosen because of its closed-form Biot-Savart integral which ensures the efficiency of the velocity evaluation. Furthermore, the correction is applied only as needed for near field interactions, which usually represent a small fraction of the calculation. The resultant scheme is highly efficient, providing the accuracy of the BCVE method but with the CPU savings of a vorton method.

3.4.1 Results of Test Runs

In their work, Bliss and Miller (Ref. 17) have applied the ANM method to several test problems involving simple geometry such as circular and elliptical vortex rings. They were able to obtain good agreement between the calculations and theory with an impressive speed-up factor of three to four compared to corresponding BCVE calculations. In an effort to independently establish the robustness and accuracy, as well as the parameter sensitivity of the ANM method, extensive test runs using the ANM method have been carried out as part of the development of the RotorCRAFT analysis. The parameters associated with the method are δs , σ_f and σ_n. , where δs is the spacing between vorton particles, σ_f is the fat core radius and σ_n is the near field cutoff distance, within which the analytical correction is applied. The following is a brief description of some of the different test cases.

The first sample calculation involved a circular vortex ring with circulation $\Gamma=1$, radius $R=1$ and core size $\sigma=0.2$ discretized into 50 equally spaced vortex elements. The induced velocity normal to the plane of the vortex ring was computed at evaluation points along a radial line in the plane of the ring. Both ANM and BCVE (with the self-induced SIVE component included) formulations were used and the results have been compared. The ANM parameters used are $\sigma_n=5\sigma_f$, $\sigma_f=\delta s$ and $\delta s=2\pi R/50$. Figure 3-12a shows a comparison of the normal velocity computed along a radial line that intersects a vortex particle. Very good agreement between the two calculations can be observed. A plot of the percentage velocity error, given in Figure 3-12b, shows that the error of ANM relative to BCVE is essentially zero in the region $0.4 \leq R \leq 1.6$, where the analytical correction is applied. A slight discrepancy is observed at $R=1.0$, the center of a vortex particle, and this is due to the difference in the self-induction model. In the region $R \leq 0.4$ or $R \geq 1.6$, slight discrepancies which are within an acceptable level, are observed. In these calculations, a speed-up factor of four for the ANM calculation was realized.

Additional calculations were run for a 4:1 elliptical vortex ring with $\Gamma=1$ and $\sigma=0.2$ discretized into 50 elements. Cosine spacing is used to give a high density of elements in the region with steep curvature. The velocity normal to the plane of the ring is computed on the major axis, where the error of the ANM method, if any, is expected to be a maximum. Figure 3-13a shows a comparison between the ANM calculation, with $\sigma_f=\delta s$ and $\sigma_n=5\sigma_f$, and the BCVE calculation. Significant over-prediction of the velocity near the interior of the ellipse, as reported in Reference 17, is observed. Calculation of the local

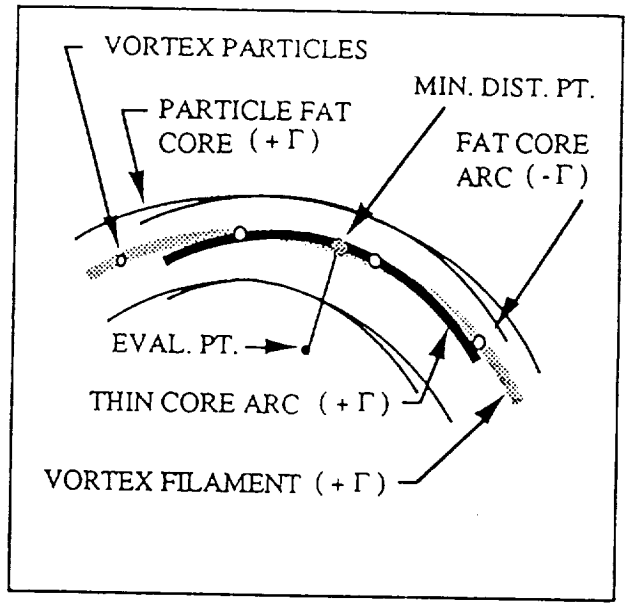

Figure 3-11a. Three-part ANM composite solution: (1) fat core vortex particle outer solution, (2) thin core analytical inner solution, and (3) opposite sign fat core analytical matching solution.

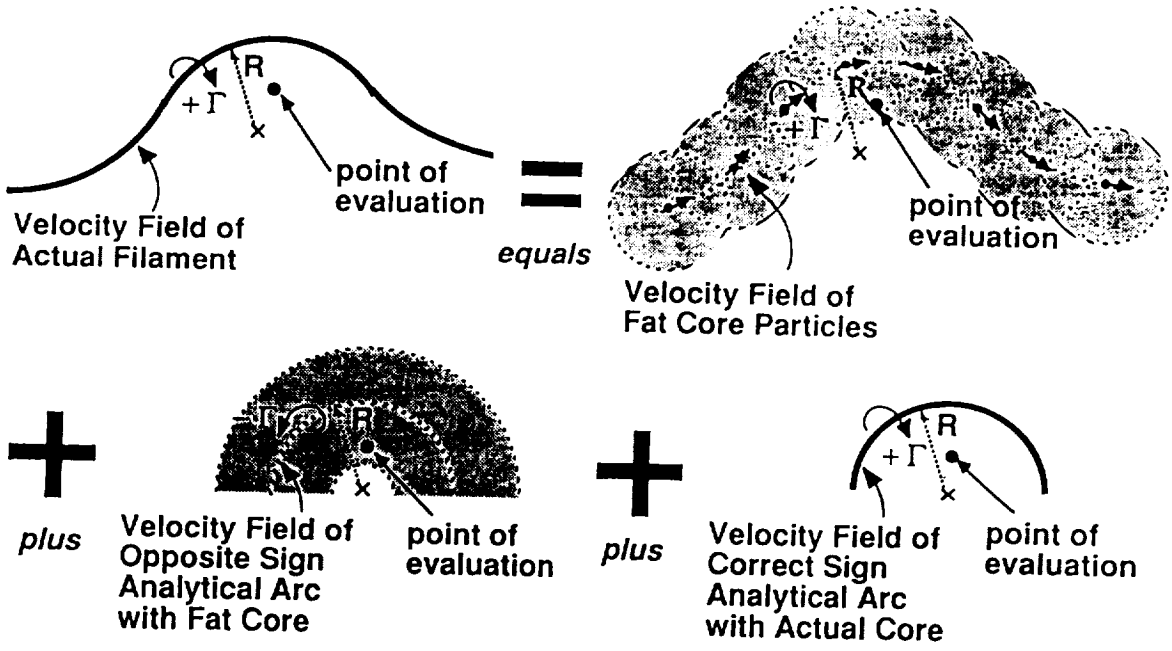

Figure 3-11b. Schematic of ANM composite solution.

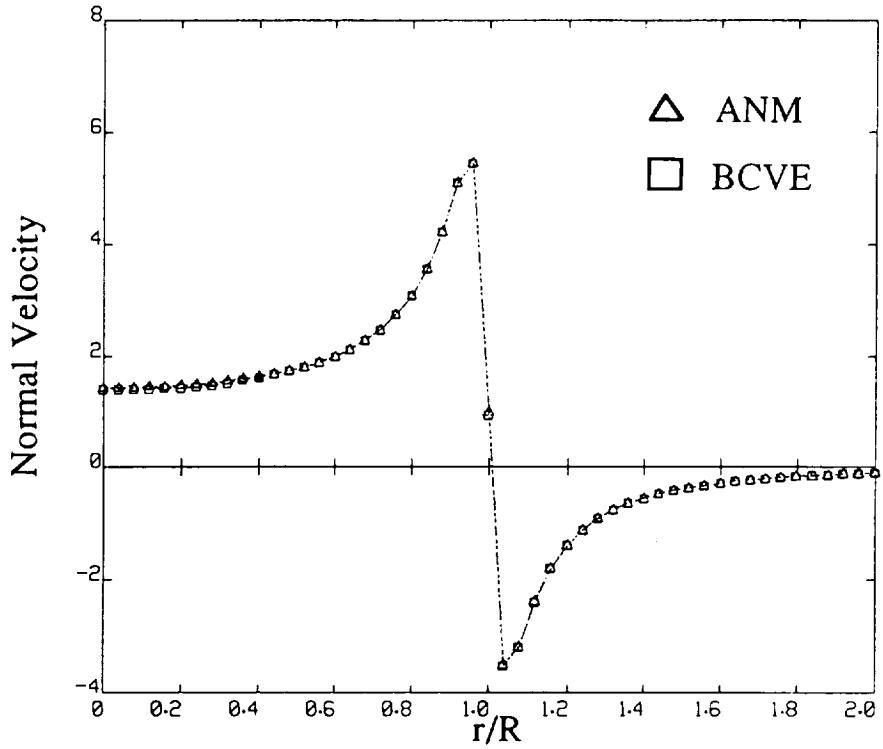

Figure 3-12a. Comparison of normal velocity at points near a circular vortex ring: BCVE and ANM calculations.

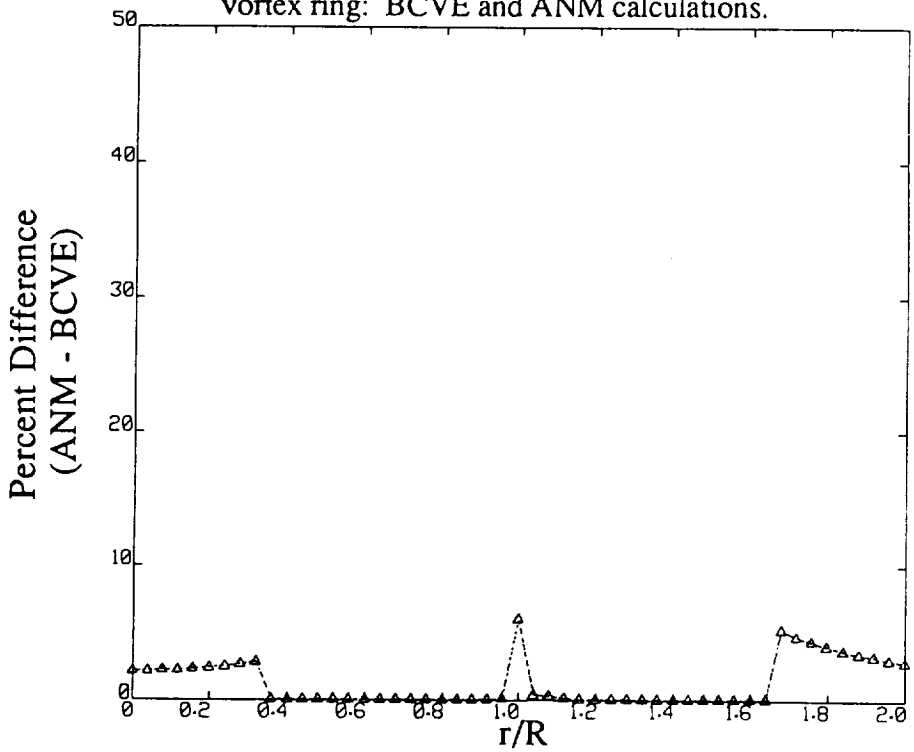

Figure 3-12b. Percentage velocity difference for ANM relative to BCVE.

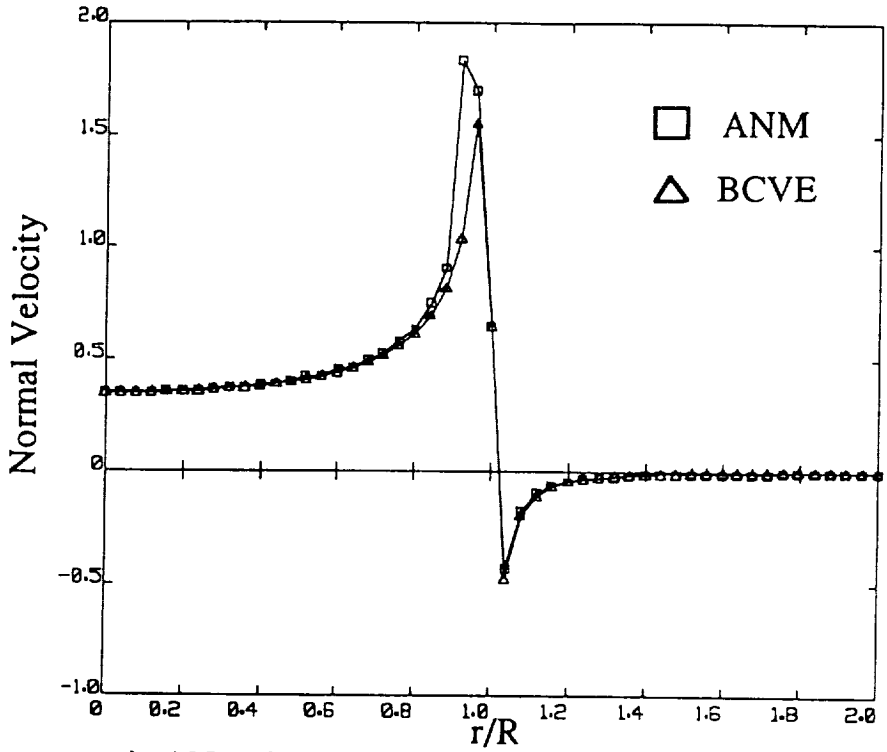

a) ANM fat core equals particle spacing.

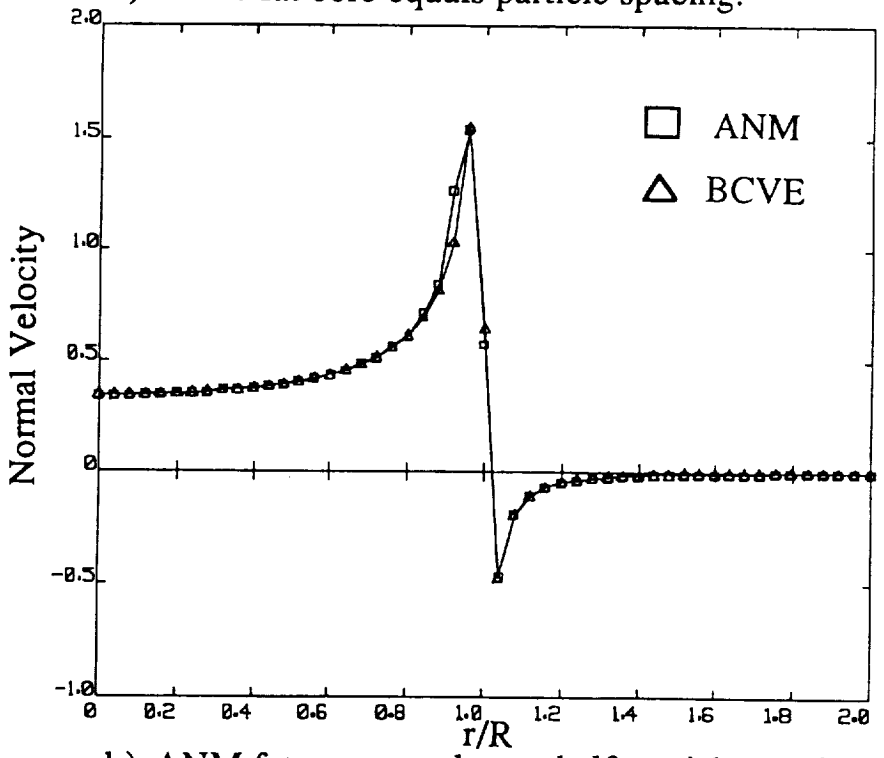

b) ANM fat core equals one-half particle spacing.

Figure 3-13. Comparison of velocity normal to a 4:1 elliptical vortex ring.

radius of curvature shows that it is less than the fat core used, implying that the fat core analytical matching is given by a small disc of vorticity, i.e. a vortex ring with core size greater than its radius. Clearly, this is not a suitable model for matching the fat core particle solution to the local thin ring solution. Repeating the ANM calculation with a reduced fat core of $\sigma_f=0.5\delta s$ while keeping the near field cutoff parameter unchanged yields improved results, as shown in Figure 3-13b. This suggests that in using the ANM method, care must be exercised to ensure that the fat core size used does not exceed the local radius of curvature and this can be achieved either by using sufficient density of vortex elements in the region of high curvature, or by limiting the fat core size used. Test runs involving variation of σ_n have shown little effect, verifying the insensitivity of the results to σ_n, which is an advantage for the method.

As these sample problems indicate, the application of vortex wake models using ANM holds considerable promise, in that flow fields with accuracy comparable to BCVE calculations can be achieved with considerably reduced computation time. A variety of calculations were undertaken to explore the suitability of ANM elements for routine use within the RotorCRAFT analysis. The test cases discussed here involve computations on a representative four-bladed rotor at both low and high advance ratio. The particular configuration used is an H-34 main rotor, operating at a thrust coefficient of 0.0037.

In the case of low advance ratio, the wake vortex filaments tend to remain close to the rotor for a substantial period of time because of the low convective flow speed. This results in significant close interactions between filaments and represents a severe test for the robustness of the ANM-based wake model in terms of its capability to handle close encounters. In this case, one revolution of the H-34 rotor at an advance ratio of 0.15 is computed with 16 steps per revolution. The ANM parameters used are $\sigma_f=0.5\delta s$, $\sigma_n=3\sigma_f$. Figure 3-14a shows a comparison of the time history of the computed airload at the 90% radial station using the ANM and BCVE-based calculations. Comparing these cases, it is observed that the ANM calculation tracks its BCVE counterpart closely. However, a 50% saving in CPU is realized when comparing the ANM to the BCVE calculation.

In the next case, calculations are carried out at an advance ratio of 0.39 and comparison of the airload time history shows excellent agreement (Fig. 3-14b). For the higher harmonics, however, the comparison, as shown in Figure 3-15a, shows some differences in amplitude and phasing. In terms of amplitude, there are significant underpredictions by the ANM calculation at the first, second and last minima, and the first and last maxima. There are also phase errors at the second maxima and minima. This can be attributed in part to errors that can be introduced at high forward speed due to the increase in the length of some of the wake elements; since the size of the fat core on the vorton elements is set at one half of the element spacing, stretching of the elements may lead to unanticipated increases in the fat core size. However, repeating the ANM calculation using a reduced fat core of $\sigma_f=0.25\delta s$ improves the amplitude comparison significantly, as shown in Figure 3-15b. Some phase difference remains, but this may be due to the coarse time discretization, i.e. number of steps per revolution. Running the calculation at a finer resolution of 24 steps per revolution improves this slightly.

3.4.2 Discussion of Parameter Selection for ANM

In these sample airload calculations of a rotor in forward flight, convective washout of an initially assumed wake geometry is used to step the solution towards convergence.

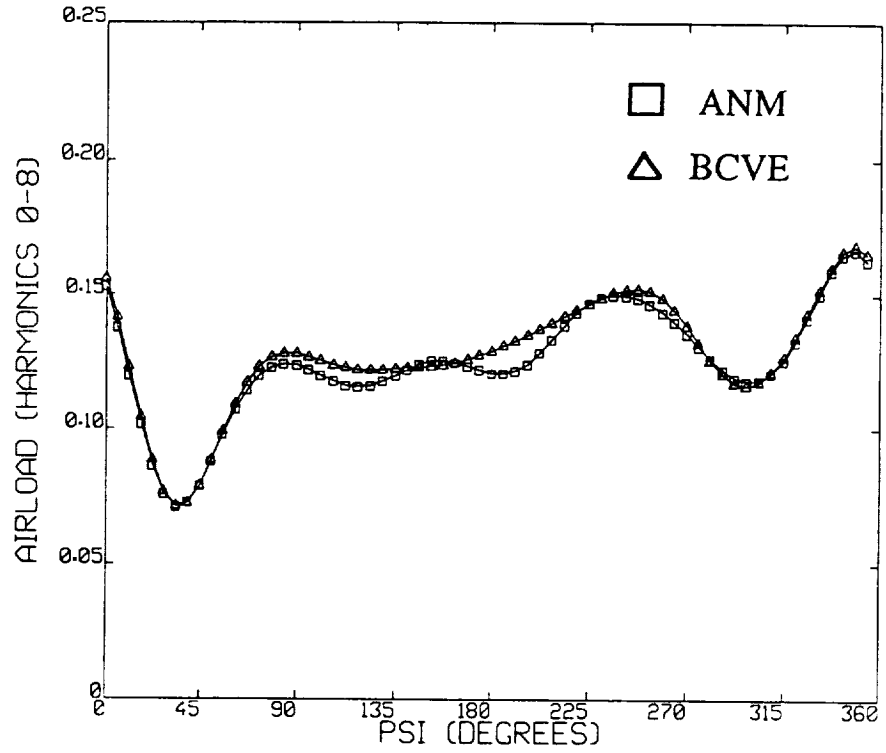

a) advance ratio 0.15

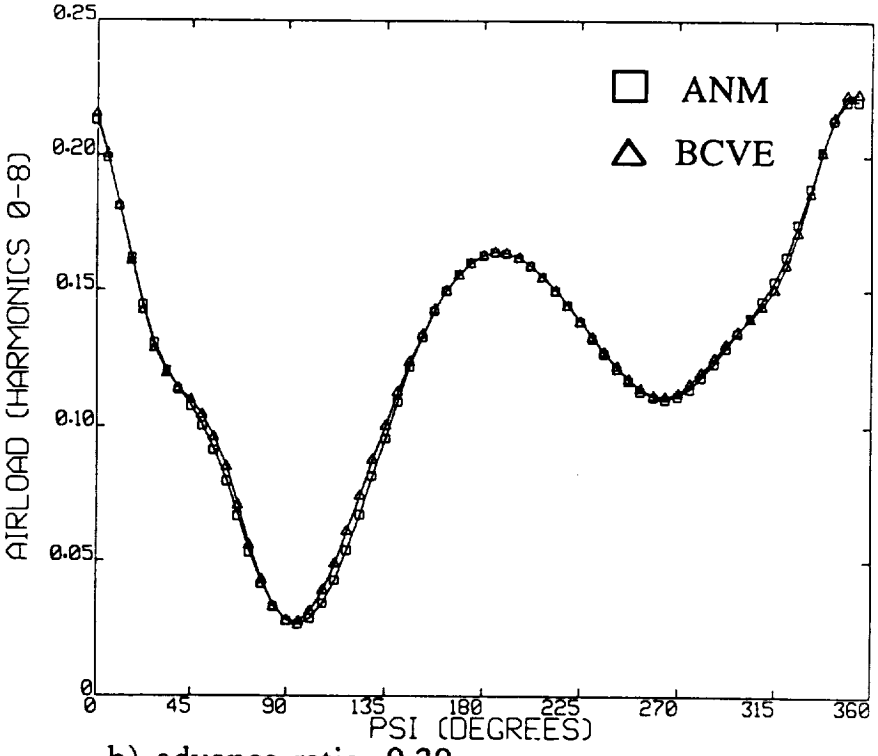

b) advance ratio 0.39

Figure 3-14. Comparison of time history of airloads at r/R = 0.9 for an H-34 rotor using ANM and BCVE wake models.

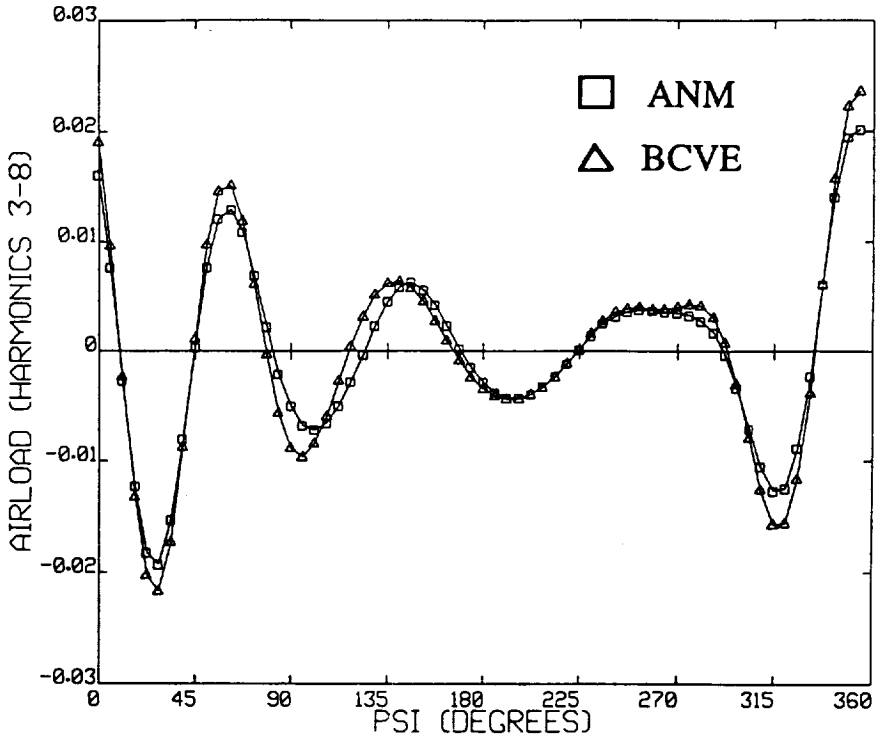

a) ANM fat core equals one-half particle spacing.

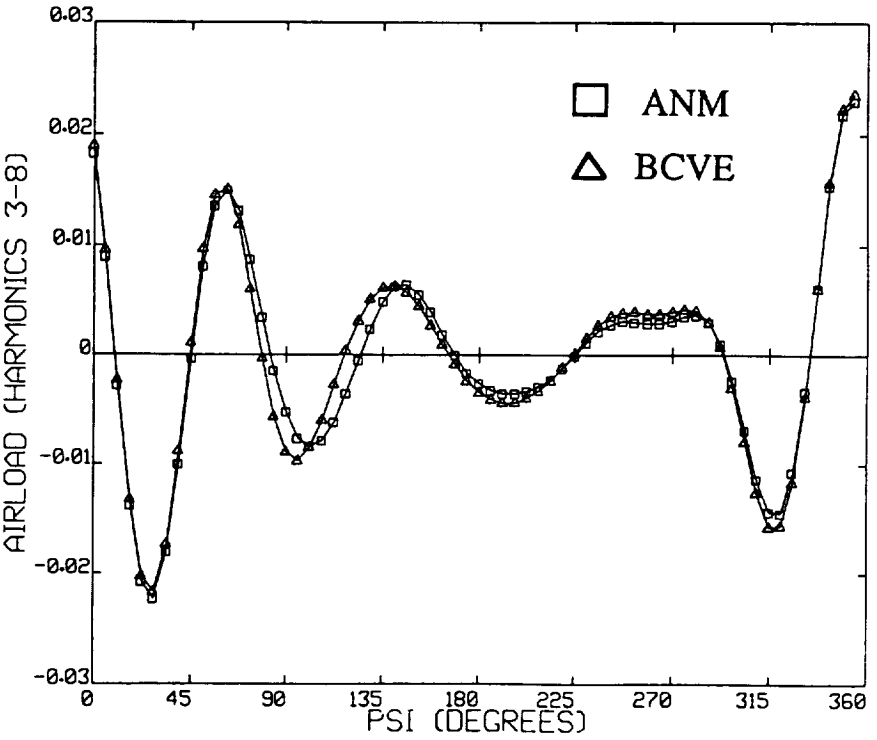

b) ANM fat core equals one-quarter particle spacing.

Figure 3-15. Comparison of time history of higher harmonic airloads at r/R = 0.9 for an H-34 rotor at advance ratio 0.39 using ANM and BCVE wake models.

For N vortex elements, this usually involves N steps to converge, resulting in an $O(N^3)$ calculation. Furthermore, for the blade dynamics calculation to converge, several rotor revolutions are required and this represents a significant computational load. To reduce the computational time, the ANM method seems a favorable candidate, in that its accuracy is comparable to BCVEs while it has a distinct advantage in efficiency. In this effort, the ANM method has been added to the forward flight code as an option to reduce computational load. Representative test runs, presented in the last section, have shown that a speed-up factor of two can be realized.

Despite the attractive savings in CPU, the ANM scheme should not at present be thought of as a replacement for the BCVE scheme, but rather as an alternative in cases where a significant time constraint is encountered. This is because as demonstrated in the last section, care must be exercised in using the ANM scheme. This is especially true for cases of high advance ratio, where wake vortex element spacings are large due to the high convective flow speed. In these cases, the fat core size of the particle should only be a small fraction of the spacing and test runs have indicate that a fat core not exceeding $0.25\delta s$ would be appropriate. This represents a sacrifice in the smoothness of the far field solution but is essential in assuring the correctness of the near field matching. For cases involving low to moderate advance ratio, the significance of such differences are diminished, and a fat core of $\sigma_f=0.5\delta s$ should be used to ensure the smoothness of the wake vorticity field. In terms of the near field cutoff parameter σ_n , test runs have showed little dependency of the results on the parameter and in general, a cutoff of $\sigma_n=3\sigma_f$ will ensure a proper matching of the far field and near field solutions.

In conclusion, it is anticipated that as greater familiarity with ANM wake elements is achieved, they will become the computational tool of choice, replacing the existing BCVE formulation. For this reason, they have been included as a computational option in the current RotorCRAFT analysis, though for the present the selection of BCVEs remains the preferred approach.

4. VORTEX LATTICE MODELING OF ROTOR BLADE AERODYNAMICS

As noted above, one of the primary tasks of the Phase I effort described in Reference 14 was to introduce a lifting surface/vortex lattice model of the rotor blade into the computation of rotor airloads. The principal motivation for this effort was to allow improved resolution of loads in the vicinity of the tip as well as during close blade vortex interactions (though the current formulation is still inadequate for prediction of loads due to direct vortex impingement on the blade surface). This model has been revised and extended during Phase II to include a refined treatment of tip effects as well as of both steady and time-varying near wake effects. After the initial effort described in Reference 14, though, a variety of areas for improvements in the baseline model were identified. Among these were the need to incorporate profile drag into performance predictions, compressibility modeling, the inclusion of lift stall , the influence of yawed flow and wake skew on load predictions, and a model of the inflow contributed by the extreme near wake. The following sections will discuss the steps that were taken to include all of these features; the discussion will overlap at many points since several of the topics are closely related. These topics will be preceded by discussion of the background on vortex lattice treatments.

4.1. Background on Vortex Lattice Models

Many modern rotors feature complex planforms, and it is advantageous to use lifting surface routines (which are a subset of the general class of aerodynamic panel methods) to analyze such designs. Subsonic panel methods have been widely used in the computation of flow around both lifting and nonlifting configurations (e.g., Refs. 30 and 31). These methods use a distribution of sources, doublets or vortices, or different combinations of these singularities arranged in a variety of geometrical forms. A wide variety of panel methods are in routine use in the fixed-wing aerodynamics community, and they have been applied to the full range of complex configurations including surfaces with thickness, complex configurations involving separated flows, surfaces interacting with nonlinear vortical wakes, and the like.

The particular model employed here focuses primarily on thin lifting surfaces with no side- or leading-edge separation (with the exception of tip effects in yawed flow discussed in Section 4.7), and so is in the tradition of models first developed by Falkner (Ref. 32) and later popularized by such researchers as Rubbert (Ref. 33) and Margason and Lamar (Ref. 34). The rotor blade is represented in the present work by a surface consisting of vortex quadrilaterals. Four constant strength straight-line vortices form the sides of each quadrilateral, except at the trailing edge of the blade where a modified vortex quadrilateral without the downstream line vortex is used. Also, as noted above, special modifications can be made to the side edge of the tip in cases where yawed flow causes part of the wake to be trailed from this edge.

Lifting surface theory has received relatively little use in rotorcraft applications, with the exception of such work as References 35 and 36. Lifting line theory has been preferred for routine use because of its simplicity and because its form simplifies the direct use of two-dimensional airfoil data to account for transonic and viscous effects. On the other hand, lifting surface theory has the advantage of a more correct treatment of three-dimensional effects. Three-dimensionality is important in the localized effects of blade vortex interaction and for the prediction of tip loading, particularly for treating novel tip shapes with considerable sweep and taper. One objective of the present effort was to explore the development of a hybrid scheme in which the advantages of both methods are incorporated.

4.2. Outline of the Vortex Lattice Layout Procedure

The lifting surface/vortex lattice analysis used here was adapted for use from the hover simulation described in Reference 23. This formulation allows substantial flexibility in the specification of the blade's planform so that complex designs may be accommodated. Currently, the lattice can be divided into as many as ten different regions, with separate linear distributions of twist, taper, and sweep within each. The spacing of the quadrilaterals in a vortex lattice analysis is an important consideration, as is discussed in Reference 37. The judicious selection of the density, spacing, and orientation of the quadrilaterals can considerably enhance the efficiency and rate of convergence of the blade loading. The current analysis has been provided with sufficient flexibility to arrange essentially arbitrary chordwise and spanwise distributions of lattice elements though the control points are always assumed to lie at the geometric center of the quadrilateral. For simplicity and convenience, however, all of the calculations discussed in this report feature uniform spacing of vortex quadrilaterals both in the chordwise and spanwise directions, unless otherwise noted.

The vortex quadrilateral lattice is drawn in blade coordinates, as defined in Figure 4-1. First the blade segments are laid out separately in the XY-plane applying taper and sweep. The lattice is displaced toward the trailing edge by a distance of one quarter of the chordwise length of the leading edge quadrilaterals. For one row of quads and an unswept rectangular planform, this puts the quad leading edge (load vortex) along the quarter chord line of the blade and the vortex lattice control points (center points of each quad) along the 3/4 chord line of the blade. The lattice is inset from the blade root and tip by a distance equal to a quarter of the width of the last quad at either edge. This technique was suggested in Reference 38, and was found both there and in sample calculations carried out for this effort to accelerate convergence of the loading solution.

For reference purposes, the quarter-chord line of the blade is taken as the line that connects the quarter chord points of each blade section, while the X axis of the blade coordinate frame is the line connecting the hub with the quarter-chord of the root section. The sweep angle for any segment is defined as the angle the local quarter-chord line makes with the X axis. Pitching moment calculations use the local quarter-chord line as a reference axis, however both collective and cyclic pitch are applied about the X axis.

In cases more complex than untwisted rectangular planforms, additional steps must be carried out. Figure 4-2 depicts the individual steps carried out in laying out the blade geometry. In actual calculations, the order of operations is different than is shown here; first, taper is applied linearly from root to tip along each segment. Then sweep is applied by displacing each segment toward its trailing edge (+Y-direction); the sweep angle is the angle between the X-axis and the quarter chord line. The twist gradient is applied by rotating each chord of the lattice about its quarter chord point. Finally, anhedral is applied by displacing each segment downward in the +Z-direction. The resulting vortex lattice structure is stored and written to a file to be used in a graphical verification of the planform.

In addition to the geometric inputs just described, a camber distribution for the blade may also be specified. Numerical input is used to describe the geometry of the camber line. When camber is present, the lattice itself is not deformed to fit the specified distribution, rather the boundary conditions at the vortex quadrilateral control points are altered to introduce the surface slope into the calculation. However, a certain minimum chordwise density of quadrilaterals is required to resolve the camber distribution; an absolute minimum of three quadrilaterals chordwise should be used, with five or more being desirable. This level of quadrilateral density can create a substantial computational

Shaft Coordinates (X_S,Y_S,Z_S)

Blade Coordinates (X,Y,Z)

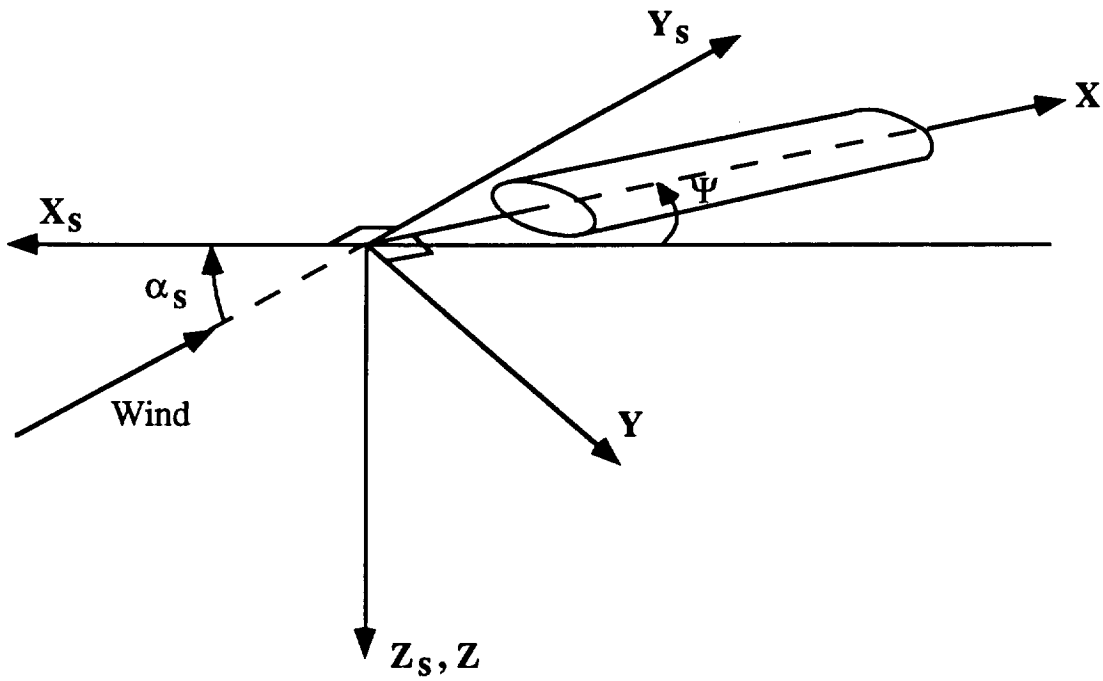

Figure 4-1. Definition of shaft coordinates and blade coordinates.

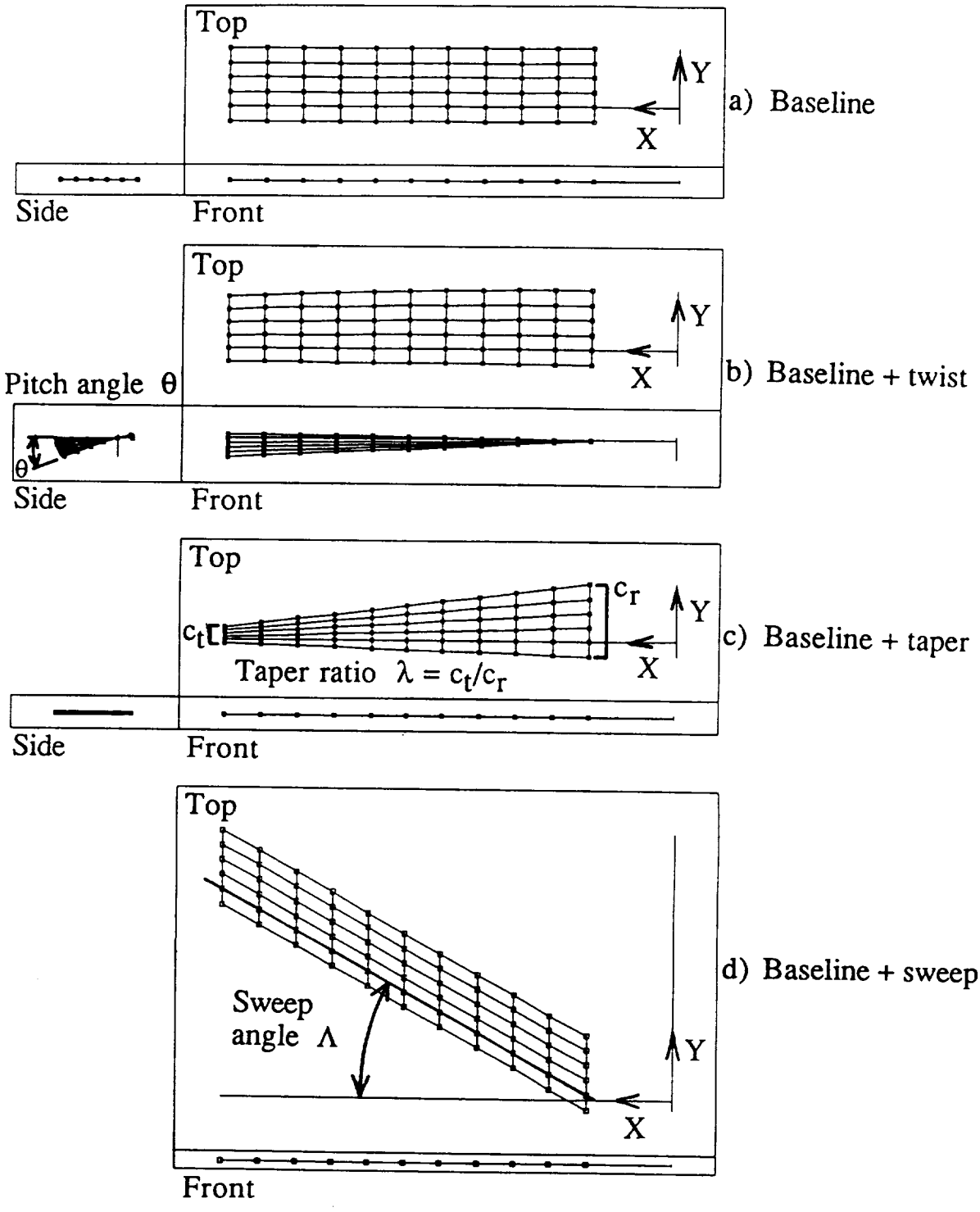

Figure 4-2. Sample blade layout: illustration of definition of taper, twist and sweep on a 5 x 20 lattice.

burden. An alternative approach for including zero lift angles is also available for cases where improved computational efficiency is desired. An appropriate rotation of the vector normal to the blade at the control points of each quadrilateral will alter the effective angle of attack of the section and can be used to introduce the shift of the zero lift angle of attack. In this manner, realistic zero lift angles of attack can be introduced into the calculations with only one quadrilateral chordwise. The zero lift angle is computed from two-dimensional airfoil data read in to support the computation of profile power, a task described in Section 4.4 below. That section will also describe the methods used for incorporating pitching moment information into calculations where camber distributions on the blade are not read in.

4.3 Computation of Aerodynamic Loads

The discussion above outlines the procedure used to lay out the vortex lattice to represent a general rotor blade planform. The solution method used to find the bound circulation given this lattice is essentially a straightforward implementation of the classical approach described in the literature on lattice methods for fixed wing applications (e.g., Ref. 34). Each of the quadrilaterals is examined individually and a mean vector normal to the quadrilateral surface is established as shown in Figure 4-3, which also shows the location of the 'control point' associated with the quadrilateral. Given this and the location and orientation of each of the quadrilaterals on the blade, the velocity induced by the blade lattice on each of the control points is determined, assuming unit strength for each quadrilateral. Then the resulting velocity is resolved in the normal direction at each control point, yielding an array of influence coefficients relating the vector of bound circulations, γ , to the downwash, $\mathbf{w}$, at each control point:

$$\mathbf{w} = A\gamma \tag{4.1}$$

where

$$A = \frac{\partial w_i}{\partial \gamma_j} \qquad i, j = 1,....n \tag{4.2}$$

Here, n is the number of vortex quadrilaterals on the blade. Note that the location of each of the quadrilaterals as well as the velocities above are defined in the blade reference system depicted in Figure 4-1.

This array of coefficients is stored and the velocity induced at each control point by the free stream, the blade rotation and deflection (discussed below), and the rotor wake are summed and resolved into 'normal-wash' velocities that are then used to find the vector γ of bound circulation values on the disk as follows:

$$\mathbf{q}_j = (\mathbf{q}_{\text{free stream}})_j + (\mathbf{q}_{\text{wake}})_j + (\mathbf{q}_{\text{blade}})_j \tag{4.3}$$

$$w_j = \mathbf{q}_j \cdot \mathbf{n}_j \tag{4.4}$$

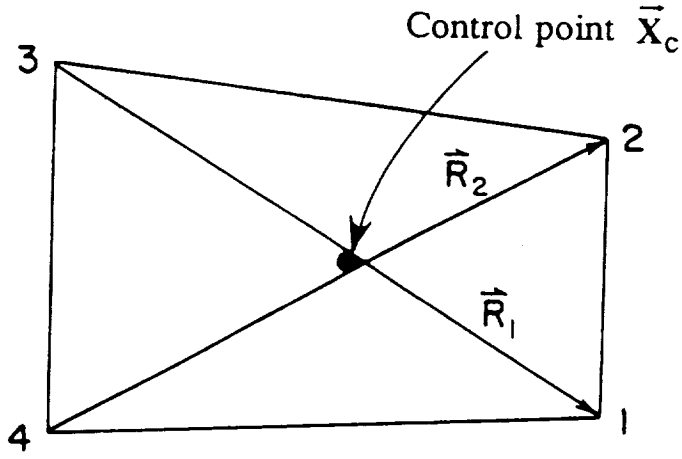

Normal vector at $\vec{X}_c$ is $\vec{n} = \vec{R}_1 \times \vec{R}_2$

$$\vec{X}_c = 0.25\left(\vec{X}_1 + \vec{X}_2 + \vec{X}_3 + \vec{X}_4\right)$$

Figure 4-3. Typical vortex quadrilateral, showing the corner indices and diagonal vectors. Control point found using the mean of the corners. Normal vector defined as indicated.

$$\gamma = A^{-1} w \tag{4.5}$$

The vector γ can then be used to solve for the forces and moments on each segment of the blade by applying the Joukowsky Law to each of the four edges of the vortex quadrilaterals, i.e.,

$$F_{jk} = \rho \gamma_j (q_{jk} \times s_{jk}) \ell_{jk} , \quad j = 1,...n \quad k = 1, 2, 3, 4 \tag{4.6}$$

Here, s_{jk} is the unit vector directed along edge k of quadrilateral j ; ℓ_{jk} is the length of this side, while γ_j is the strength of the quad. The reference velocity q for the evaluation of forces is computed at the mid point of the edge k . This velocity contains all the components deriving from the free stream, the wake, the motion of the blade, and the velocity induced by the entire vortex quadrilateral grid, though the influence of the segment on which a particular point lies is deleted. These individual forces are then summed to yield the integrated forces on each blade:

$$F = (HI_S + YJ_S + TK_S) = \sum_j \sum_k F_{jk} \tag{4.7}$$

Moments exerted by the blade about the sectional quarter-chord reference axis can also be computed:

$$M = (LI_S + MJ_S + NK_S) = \sum_j \sum_k F_{jk} \times r_{jk} \tag{4.8}$$

Moments about the flapping and lagging axes of the blade are taken to compute the gross blade motion, while pitching moments can be computed for each section to use for the calculation of torsional deformation. Here, r is the vector from the reference axis to the point of action of F. (Tabulated information on pitching moment coefficients can also be used to determine the moments, as will be described in the next section).

The resulting forces and moments are computed in the blade reference frame and are then transformed into the shaft frame to yield the thrust and induced torque. Additional computations are undertaken to resolve those components that contribute to the horizontal and side forces (H and Y, respectively). Of course, these calculations omit the effect of viscous forces on the blades, and steps must be taken to include them. However, the basic vortex lattice analysis can be modified to include the effect of compressibility on the sectional lift and moment, and the approach taken to these issues is described separately below. Other modifications are necessary to account for stall, yawed flow, and unsteady effects in the near wake; these topics are also taken up in the following sections.

4.4 Prediction of Sectional Profile Drag and Profile Torque

To introduce forces generated by profile (viscous and pressure) drag into the calculation, the only practical approach at present is the use of two-dimensional airfoil data.

The form of data required for this coupling is tabulated values for sectional drag coefficients as a function of both Mach number and sectional angle of attack. The definition of the local Mach number at a particular radial station is relatively straightforward, being

$$M(r,\psi) = \Omega R \frac{\left(\left(\frac{r}{R}\right) + \mu \sin\psi \cos\alpha_s\right)}{a_o} \tag{4.9}$$

though adjustments for tip relief are required in general. A more uncertain issue is the definition of an effective angle of attack for use in the look up tables.

The definition of effective sectional angle of attack is intrinsic to lifting line theory, being defined as

$$\alpha_e = \alpha_g - \alpha_i \tag{4.10}$$

where α_i is the inclination of the effective free stream to the local zero lift line. The definition of the α_i in the context of rotary wing lifting line theory is relatively straightforward, being

$$\alpha_i = \tan^{-1}\left(\frac{U_P}{U_T}\right) \tag{4.11}$$

where U_P is the flow field component normal to the section in blade coordinates, while U_T is the tangential flow component. U_P itself consists of contributions from the free stream, the blade motion, and the wake-induced velocity field. In the context of lifting line theory, the wake-induced velocity is evaluated at the quarter-chord point of the section. However, in vortex lattice models, there is no clearly defined reference point at which the wake-induced velocity can be computed to yield its contribution to the effective angle of attack for the section.

To define such a reference velocity in the context of lattice methods, first recall that in the limiting case of a high aspect ratio wing or rotor blade, a good approximation to the two-dimensional flat plate solution for a lifting airfoil can be recovered by using a large number of chordwise vortex quadrilaterals. In this sense, the portions of the lattice running parallel to the blade span constitute the "two dimensional part" of the lattice solution. Conversely, the trailing legs of the vortex quadrilaterals represent the "three dimensional part" of the solution, since they would all have zero strength on a wing or blade of infinite aspect ratio. The flow components associated with these trailers are directly related to finite span effects. On this basis it is appropriate to define an effective angle of attack for a section by deleting the flow field contributions from the spanwise quadrilateral edges and computing simply the contributions from the chordwise or trailing legs of the lattice.

This reference velocity, suitably averaged over the chord for cases involving more than one quadrilateral chordwise, provides the component of induced velocity that is

contributed by the blade and near wake trailers in the overlap region to the complete induced angle of attack. (Note that this approach reduces to the lifting line definition of induced velocity for the case of one chordwise quadrilateral). The resulting velocity is then added to the velocity field generated by the rest of the wake in the manner indicated in Equation 4.10 to yield the effective angle of attack. The local Mach number and angle of attack can then be used to enter two-dimensional look-up tables to compute drag and moment coefficients; lift coefficients are also routinely looked up, though they are used only to define post-stall characteristics, as described below.

The two-dimensional coefficients are, of course, defined only for a specific airfoil section. Many rotor blades feature more than one section along the span. In the current analysis, as many as ten sections along the span may be specified. For any given spanwise station, the section coefficients are computed for each of the two airfoils that bound the segment containing the station of interest and then interpolated linearly to the desired point. Similarly, for each Mach number/angle of attack pair, bilinear interpolation is used to find the appropriate coefficients within each look-up table of lift, drag, and moment coefficients.

4.5 Compressibility

Compressibility has an important effect on rotor performance at typical tip Mach numbers for modern rotors. Some of this effect is captured by the inclusion of Mach number dependence in the look-up tables used for profile drag coefficients. However, compressibility also has a significant impact on the lift generated by airfoils at specified angles of attack, and so its influence on thrust and induced power must be considered as well. This section discusses how the augmentation of lift associated with compressible flow can be achieved. Preliminary work has also indicated that some of the nonlinear aspects of airfoil section behavior associated with transonic flow (i.e., alterations in moment coefficients and zero lift angle) can be incorporated in the context of nominally linear vortex lattice methods; implementation of methods to accomplish this has been reserved for follow-on work.

For two-dimensional thin airfoils, treatments like the Prandtl-Glauert correction to lift curve slope are acceptable methods for including compressibility effects. In vortex lattice calculations, transformations that are similar in spirit but more elaborate in detail must be invoked. When analyzing hovering rotors, Kocurek, in Reference 35, used a transformation of the entire space surrounding the rotor in generating a correction for compressibility. Currently, a more restricted transformation of the blade geometry is used, one based on the local Mach number at the radial stations along the span.

It is assumed that the flow around a given blade section can be found using the compressible potential equation

$$\beta^2 \phi_{xx} + \phi_{yy} + \phi_{zz} = 0 \qquad \beta^2 = 1 - M^2(r,\psi) \qquad (4.12)$$

where M represents the local Mach number as defined in Eq. 4.8. (For this discussion, x denotes the streamwise flow direction (positive downstream); y lies along the radius (positive out); and z is positive up.) Using a transformation whereby x is replaced by βx_i , y by y_i , and z by z_i changes the above equation to:

$$\phi_{x_i x_i} + \phi_{y_i y_i} + \phi_{z_i z_i} = 0 \qquad (4.13)$$

This equation governs the incompressible flow around a transformed blade in which the blade chord is stretched by a factor of β^{-1} (note that β varies along the radius). The transformed blade is used in the time stepping analysis to find the wake geometry and the associated loads on the blade. Then, the loads must be corrected in accordance with the geometrical transformation to obtain the thrust and torque on the rotor in compressible flow.

The transformation outlined above leaves the bound circulation, the downwash on the blade, and the dimensional lift per unit span the same for both the compressible and incompressible problems. Thus, the thrust and induced power computed for the transformed, incompressible problems are the same for the original, compressible problem. However, because of the stretching of the airfoil chord, the lift coefficient for any section for the compressible problem is greater by a factor of β^{-1} than the lift coefficient in the transformed, incompressible problem.

4.6 Stall

To this point, the discussion has focused implicitly on the prediction of the loading at low to moderate angles of attack. In many forward flight conditions, sections of the blade span can reach or exceed the static stall angle. A vortex lattice calculation will compute unrealistically high sectional lift for such cases, since no allowance is made for lift limitation or indeed for other than linear lift characteristics. It is inappropriate to expect that models currently available will be able to offer detailed insight into the loading on those portions of the rotor blade undergoing stall. However, reasonable steps can be taken to ensure that the major features of the lift behavior of rotor blades can be captured.

First, it should be noted that the presence of yawed flow will substantially increase the nominal maximum lift coefficient that a section of the blade may carry. Experimental evidence of this phenomenon has been observed in experimental work on fixed wings, and the qualitative model used to allow for this effect is discussed immediately below. Also, many rotor configurations have a substantial sensitivity to rate effects in delaying the onset of stall. Reference 5 among many other sources discusses the potential importance of dynamic stall. No dynamic stall model is used in the present version of RotorCRAFT, though it is a prominent candidate for addition in follow-on development.

As discussed in Section 4.4, the local effective angle of attack is computed at each radial station on the blade, as is the section lift coefficient and the maximum lift coefficient permitted by the look-up tables. Once the computed c_ℓ (appropriately adjusted for yawed flow) exceeds the stipulated maximum lift coefficient, the stall model is invoked and the effective angle of attack is used to look up an appropriate lift coefficient given the Mach number of the onset flow. The vortex lattice lift calculation for the section is overridden by a new value for sectional lift with the form

$$\ell = \frac{1}{2} \rho \left(U_P^2 + U_T^2 \right) c c_\ell \qquad (4.14)$$

This new lift calculation is then resolved to provide thrust and torque contributions in the shaft axis system for subsequent use in performance and dynamics calculations. The local bound circulation is also reduced to properly reflect the reduced lift at the section. The computation of profile drag is not affected, since 2-D look-up tables using the effective angle of attack are used for both stalled and unstalled sections. Sample calculations using this procedure in the context of wing calculations are discussed in Section 4.9.

4.7 Overlap Near Wake

As described in Section 3, the rotor aerodynamics analysis utilizes a free wake having constant strength vorticity contours coupled to a vortex quadrilateral model for the blade aerodynamics. To achieve consistent results, an overlap wake model is used behind each blade to capture the effects of the extreme near wake. The overlap wake is a finite length prescribed wake consistent with the vortex quadrilateral model, namely it consists of a set of vortex filaments trailing behind the quadrilateral structure. When calculating downwash at points on the blade, the overlap wake provides a near field contribution, while contributions from the remainder of the wake are provided by the constant strength contour free wake. On the other hand, when calculating velocities in the wake, the free wake is extended right up to the blade, hence the overlap. The overlap wake is needed because the free wake model is not consistent with the blade vortex quadrilateral model in terms of either the number of filaments or their location with respect to the blade control points.

The following technical issues were examined with respect to the overlap wake model and its role in the calculation of the blade aerodynamic loads:

- Accuracy of the truncation of the overlap wake and its replacement with the constant vorticity contour wake beyond a certain distance.

- Treatment of the overlap wake with respect to skewed inflow, i.e. effective sweep, as the blade rotates.

- Treatment of the blade tip as downstream edge in the presence of skewed inflow (effective sweep).

These issues were studied by examination of the simpler problem of a straight rectangular wing in a skewed (swept) inflow. This problem contains all the physics essential to the above issues, without the complexity of a rotor calculation. The important physical effects are thereby more easily separated and examined. A simplified version of the same vortex quadrilateral code used for the rotor analysis was used for this study of corresponding effects on a vortex quadrilateral wing. The study of wake truncation is presented here, while the results of the skewed inflow analysis are presented in the next section.

The effect of wake truncation was examined by considering a rectangular vortex quadrilateral wing in uniform, unswept flow. At a certain distance behind the wing the trailing vortices were truncated and replaced by a vortex pair. Each vortex in the pair has the same net circulation as the wing bound circulation, and each is located at the spanwise centroid of the corresponding trailed vorticity from the near wake. This case is an extreme one, in that it corresponds to a rotor blade with a constant vorticity contour free wake having only two filaments. Note that the positioning of the free wake filaments in the rotor code is essentially equivalent to centroidal positioning. The geometric layout is shown in Figure 4-4 ("centroid model").

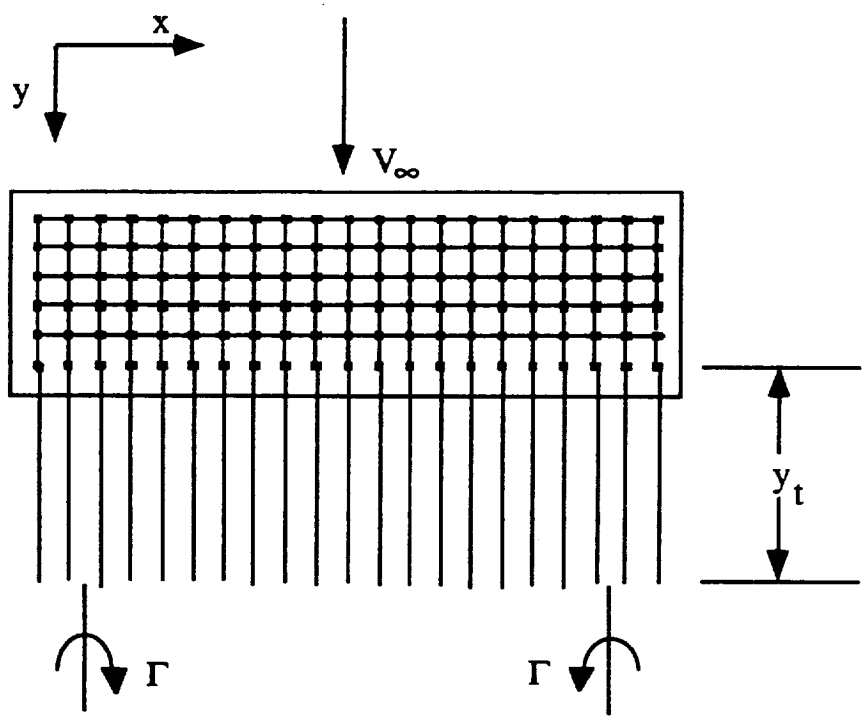

Figure 4-4. Schematic of the model problem for the study of wake truncation.

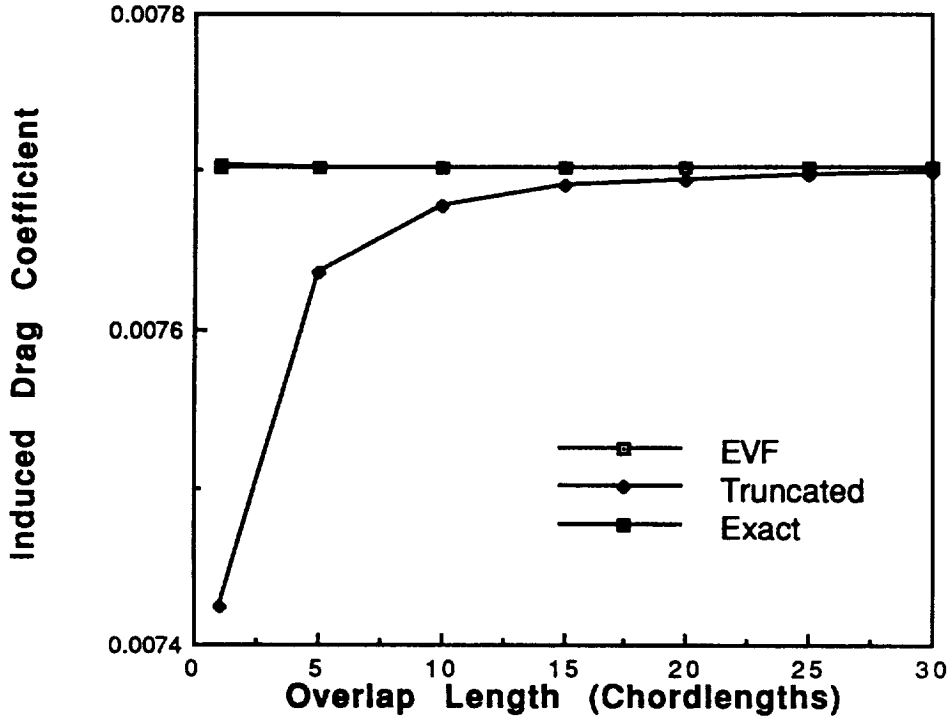

Figure 4-5. Predictions of induced drag on a wing with aspect ratio 4.0 as a function of y_t .

The planar vortex wake in Figure 4-4 is composed of N discrete parallel vortex filaments, truncated a distance y_t behind the trailing edge. Such vortex systems are commonly used in the vortex lattice method, or VLM, to model the trailing wake of a finite wing, except they normally extend to infinity. The vortex system can be described entirely by the space coordinates of the vortices and their strengths. Certain invariants of motion apply in a two dimensional sense to vortices in free motion, and this leads naturally to the concept of a center of vorticity and an effective net vortex strength.

At some distance from the vortex system the effects of the vortex system become indistinguishable from the effects of an equivalent vortex filament of net strength Γ located at the centroid, or center of vorticity, of the system. For the group of discrete vortex filaments of strength Γ_i located behind one half (semi-span) of the wing, the spanwise coordinate of the center of vorticity is defined as:

$$X = \frac{\sum_{i=1}^{N/2} \Gamma_i x_i}{\sum_{i=1}^{N/2} x_i} \qquad (4.15)$$

The strength of the equivalent vortex is:

$$\Gamma = \sum_{i=1}^{N/2} \Gamma_i \qquad (4.16)$$

The equivalent vortex filament (EVF) concept was implemented into the VLM wing code. The wake is divided in two by a line parallel to the free stream passing through the mid-span. Each filament of the equivalent vortex filament pair has a strength equal to the net strength of the portion of the truncated wake which it replaces. Thus the net circulation is conserved. The filaments of the equivalent vortex pair are placed at the centers of vorticity of the divided wake. The wake is divided in two by a line parallel to the free stream. Each filament of the equivalent vortex filament pair has a strength equal to the net strength of the portion of the truncated wake which it replaces. Thus the net circulation is conserved. The filaments of the equivalent vortex pair are placed at the centers of vorticity of the divided wake.

In the standard VLM calculation flow tangency conditions are enforced. Aerodynamic performance characteristics are then obtained from an inversion of an influence coefficient matrix. This matrix is based entirely on the geometry of the problem. The EVF concept was implemented by making this process iterative. The locations and strengths of the centroidally placed far-field vortices were iterated upon until flow tangency conditions were met.

Three wake models were considered for the present study. The first model was that of the full wake without truncation (namely y_t -> infinity), which is the standard way of modelling the wake in VLM. The second model truncated the wake at a finite distance without replacing the truncated section of the wake. The EVF model also truncates the wake at a finite distance, however the lost wake is replaced by an equivalent vortex filament pair.

Parametric studies were performed to study the validity of the EVF concept. The studies were performed on a rectangular wing having aspect ratio of either four or ten, with a flat plate airfoil. The planform was at five degrees angle of attack. The study compared overall and sectional load properties. Sectional lift and drag coefficients were plotted for various wake truncation lengths. Overall planform lift and drag coefficients are plotted as a function of the wake truncation point. Figure 4-5 shows the induced drag coefficient of the wing (a quantity that is especially sensitive to the downwash distribution) as a function of the truncation distance (expressed in multiples of the chord) for a wing of aspect ratio 4. Very small errors occur between the full wake and the EVF model, even for truncation at one chord length behind the wing. The most significant errors occur for the case with the wake truncated and not replaced with an equivalent far field vortex pair. For higher aspect ratio the same trend is observed, but with smaller percentage errors since the importance of the wake decreases with increasing aspect ratio. While it might be expected that the integrated drag might be relatively insensitive to the wake model, it was surprising to find that the detailed load distribution were also relatively insensitive. Only the case with the far wake completely removed showed large deviations in distribution as the truncation point was moved closer to the trailing edge. The EVF model showed errors of no more than a few percent, and typically less, as the truncation point was brought to within a chord of the trailing edge.

The results reveal a single very important conclusion. The model using an equivalent centroidal vortex pair works extremely well, even when truncation of the near wake and transition to the pair occurs relatively near the blade. It follows that the rotor code should have excellent accuracy in this regard, since it normally uses more than two filaments in the free wake, and typically makes the transition from the overlap wake several chords behind the blade.

4.8 Yawed Flow

In forward flight, many sections of the blade are operating with local effective free streams that are yawed substantially from the direction normal to the leading edge. Though the local flow vector can be substantially affected by wake-induced velocities, the yaw angle at any section can be reasonably approximated by

$$\Lambda \cong = \tan^{-1}\left(\frac{\mu\cos\alpha_s\cos\psi}{\frac{r}{R} + \mu\cos\alpha_s\sin\psi}\right) \tag{4.15}$$

It is clear that for rotors at high advance ratio substantial yaw angles will be present when blades are located at azimuth angles 0° or 180°, particularly for inboard sections. These yaw angles have several important effects on rotor performance.

First, as noted above, the presence of yaw can substantially increase the allowable maximum lift coefficient on a blade section. The lift on a blade section is conventionally defined using only the flow component normal to the leading edge as a reference velocity.

With c_ℓ defined on this basis, then the maximum lift coefficient that can be carried is increased to

$$\frac{(c_{\ell max})_{\Lambda = 0}}{\cos\Lambda} \tag{4.16}$$

This delays the onset of stall in that larger sectional lift coefficients can be attained before the stall model is invoked. In addition, the presence of yawed flow changes the direction and magnitude of the profile drag on the section, in that the drag is assumed to act parallel to the local free stream and not parallel to the local chord line.

The presence of yawed flow also has a significant effect on the lift in the vicinity of the blade tip. For wings in rectilinear flight or for rotor blades operating at azimuth angle 90° or 270°, the flow near the tips is ordinarily essentially parallel to the chord line, and the wake leaves the trailing edge smoothly. However, in the highly yawed flow that can occur in the fourth and first quadrants, the side edge of the blade becomes an effective "trailing edge" where a Kutta condition should be applied. Such an effect is not captured in the basic vortex lattice model since the trailing legs of the vortex quadrilaterals in the last row at the tip overlap one another, so that they effectively constitute a single vortex line at the tip (see Fig. 3-9). Once the wing or blade experiences substantial yawed flow, leaving this treatment unmodified can lead to errors in the load distribution near the tip. As suggested in Figure 4-6 , the quadrilateral edges at the tip of the lattice will ordinarily generate suction forces in the presence of yawed flow. In point of fact, in this flow configuration, the side edge of the blade should be treated like an extension of the trailing edge, with a condition imposed to null the forces carried at this edge.

This can be accomplished by allowing the lattice trailers to depart the blade parallel to the yawed flow instead of parallel to the chordline, as depicted in Figure 4-7. The tip edge trailers are allowed to move with the local flow as the blade moves from azimuth angle 270 to azimuth angle 90, though they are fixed parallel to the chord over the rest of the azimuth. This treatment can be invoked or bypassed as desired, but it typically has the effect of increasing the blade loading near the tip relative to the unmodified lattice layout; invoking the yawed tip trailers and imposing the Kutta condition on the tip edge eliminates the suction force associated with yawed flow and typically causes the entire load distribution at the tip to shift slightly and become more positive.

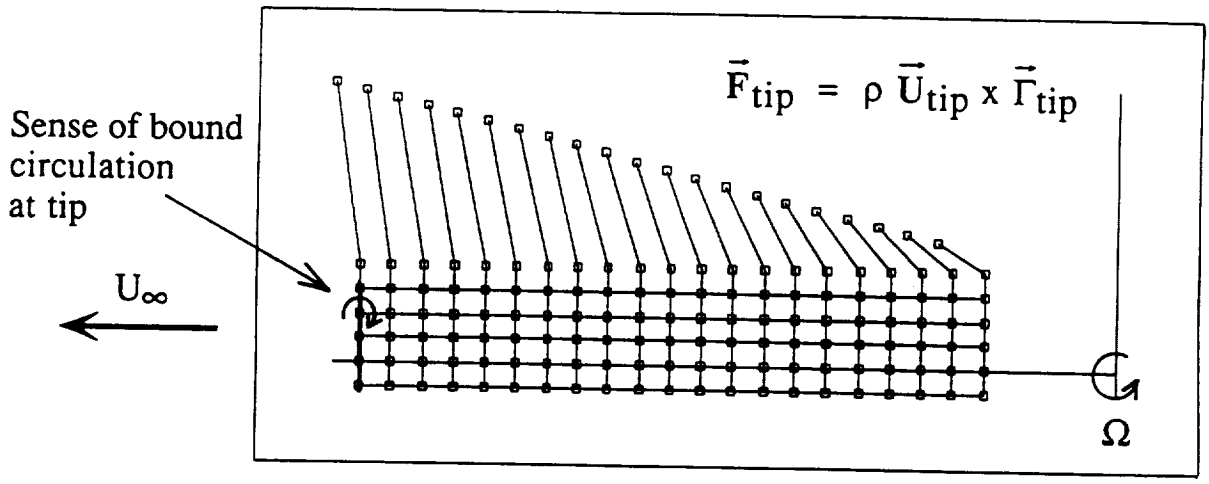

Figure 4-6. Top view of typical rotor blade 5 x 20 vortex lattice at advance ratio 0.4 , azimuth angle 0° . Yawed flow due to U_∞ produces suction (downward force) on side edge in the fourth and first quadrants.

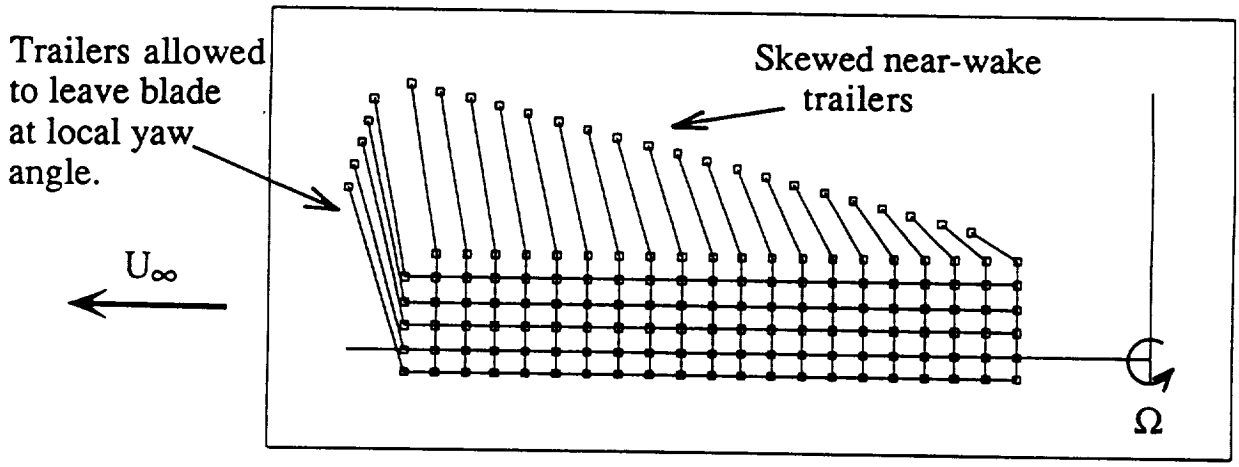

Figure 4-7. Same blade as Figure 4-6 with tip trailers released at local flow yaw angle. Kutta condition enforced on blade tip.

5. FORMULATION OF THE ROTOR BLADE DYNAMIC MODEL

The structural properties of the helicopter blade are clearly critical to the evaluation of the response and performance of a helicopter in forward flight. Thus, one of the major efforts within the development of the RotorCRAFT code has been to incorporate a realistic finite element (F.E.) representation of the blade. This section discusses the formulation of the dynamic model itself and outlines its capabilities and limitations. The description of its coupling with the aerodynamic model discussed above is reserved for Section 6; further description of the inputs required for this portion of the analysis are given in Reference 39.

A preliminary word on the reference frames used in this discussion is in order. Figure 5-1 shows the axis systems used in this calculation. The basic reference frame in the calculation is the wind axis frame, with X_w pointing into the relative wind, Z_w pointing down in the plane containing the rotor shaft and Y_w at right angles to these axes. The shaft axis is reached by a rotation of an angle α_s around the Y_w axis. The blade axis system is then reached by a rotation of an angle $(180-\psi)$ around the Z_s axis, so that the Z_s and Z_w are coincident. In the discussion that follows, the blade axis system is also referred to as the 'global' axis system to distinguish it from local axis systems attached to each of the elements used in the dynamic model.

5.1 Finite Element Structural Model of the Helicopter Blade

The particular finite element (F.E.) model used here to represent the helicopter blade accounts for extension, twist and transverse bending displacements. To accurately simulate these deformations, the blade is discretized into a number of beam finite elements each having a total of 14 degrees of freedom (d.o.f.). Stiffness properties for each element are computed from the cross-section geometry and material properties supplied by the user. Similarly, the blade mass distribution is used to both define elemental mass matrices and also to compute the contributions of blade rotation inertia forces to the stiffness matrices (geometric stiffening) and nodal forces. The resulting elemental mass and stiffness matrices are then assembled and any constrained d.o.f. eliminated to finally yield the corresponding global matrices for the complete blade structure. The approach taken is similar to previous implementations of F.E. methods for rotorcraft applications, such as Reference 40.

The resulting mass and stiffness matrices serve as inputs to the standard eigenvalue problem which must be solved to obtain the modal frequencies and shapes for the F.E. model. It is pointed out that the modal properties are dependent upon the frequency of blade rotation since the geometric stiffening is proportional to the square of this frequency. The generalized eigenvalue problem is solved by a standard Jacobi iteration technique.

The transfer of information between the structural and the aerodynamic models in RotorCRAFT occurs chiefly via the modal properties of the blade. In essence, the mode shapes are used to compute generalized modal forces from the distributed aerodynamic forces. These modal forces drive the corresponding modal responses. These responses in turn are used in conjunction with the mode shapes to determine the instantaneous displacements and velocities at any point along the blade. Finally, the blade deformations and deformation rates provide the necessary information to update the flow field and aerodynamic forces, as described in the previous section. Hence, one iterates toward a steady state solution where the blade displacements and their rates are constant at each

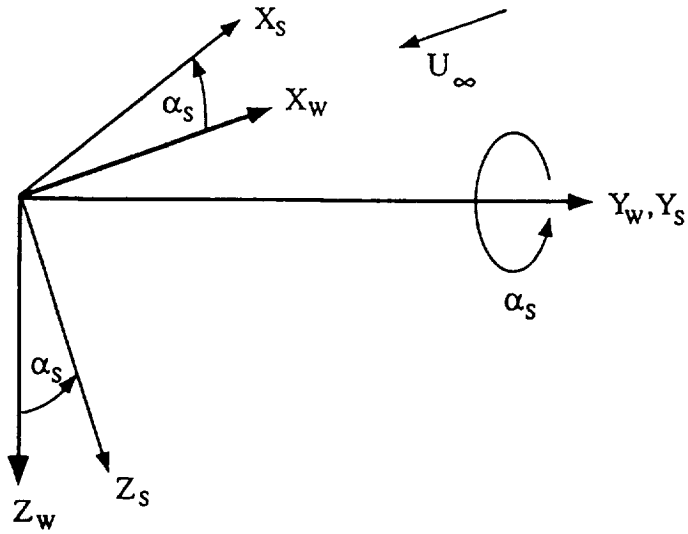

a) Rotation of wind axis system about Y_W to reach shaft axis system (Z_S parallel to rotor shaft)

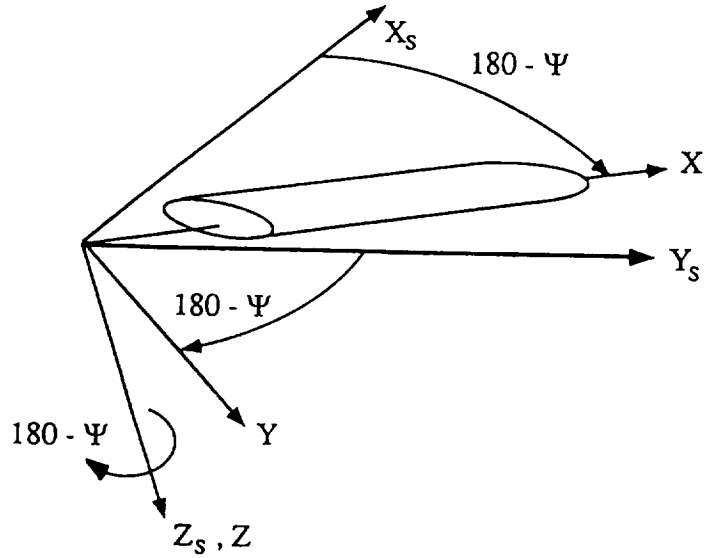

b) Rotation of shaft axes about Z_S to reach blade axis system (X,Y,Z)

Figure 5-1. Axis system definitions.

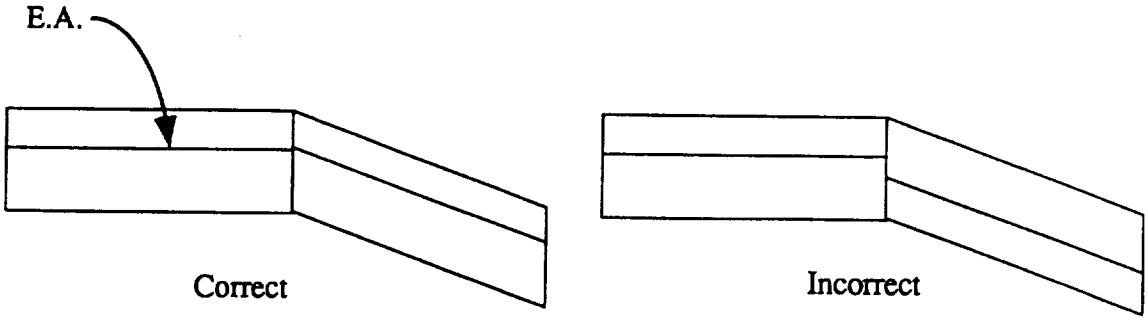

Figure 5-2. Correct and incorrect alignment of the elastic axis (E.A.) between adjacent elements.

azimuthal location. The remainder of this section explains in greater detail the derivation of the structural model and of the mode shapes and generalized forces that enter into the dynamic computation.

5.1.1 Assumptions

The assumptions inherent in the blade model and geometry are stated below:

- The blade displacements are of sufficiently small magnitude that:
  - linear constitutive relations between stress and strain are applicable,
  - the transformation matrix relating the local axes of each element may be regarded as constant and equal to the corresponding matrix in the undeformed state,
  - negligible approximation is made in assuming that rotations due to deformation commute, and,
  - the twist, bending and extension deformations may be linearly superimposed.

- The blade material is assumed isotropic and the stress-strain relation obeys Hooke's law.

- The elastic axis for each element is defined. The elastic axes of any two adjacent elements coincide at their mutual joining section (see Fig. 5-2). In other words, the elastic axis is continuous along the blade. This is necessary to correctly define the assembly of the individual blade F.E. s.

- The principal axes of the cross-section for each element are assumed to be perpendicular to the elastic axis of that element. This implies that if there are sweep and anhedral changes between consecutive elements then their principal axes will not coincide at their mutual section. The degree of approximation introduced into the bending calculation will increase with the amount of sweep and anhedral change between adjacent elements. It will also decrease with slenderness of the element since the discrepancies resulting from non-alignment of the principal axes occur locally in the neighborhood of the joining section.

It is pointed out that the last two assumptions are mainly due to the fact that warping effects are modelled in the analysis. One of the chief advantages of the finite element method is its versatility in the assembly of the constituent elements. For simple elements, e.g., pure beam elements and bar elements, one is free to assemble the components in whatever orientations one chooses. Furthermore, discontinuities in the mass and stiffness properties from element to element are permitted. However, when modeling warping deformations the line of shear centers, or elastic axis, plays a significant role. The current formulation approximates the elastic axis by a sequence of straight line segments and it is the desire to accurately represent the elastic axis that results in the preceding last two assumptions. Thus to the extent that warping effects are significant, failure to satisfy the last two assumptions and suitably approximate the elastic axis leads to error in the solution. In most cases however, and for the closed tubes representative of helicopter rotor blades, warping effects will be dominated by deformations arising from pure bending and torsion,

and thus violation of these assumptions will not lead to significant error. This has been verified by numerical testing of the FE model for loaded structures containing 90° elbow joints and discontinuities in the beam stiffness properties.

5.1.2 Blade Geometry

Each of the blade segments defined in the RotorCRAFT blade geometry input is subdivided into structural finite elements in the manner specified by the user. The global axes for the assembled blade are denoted by XYZ corresponding to the blade axes defined in Figure 5-1. Local axes, xyz , are defined for each element such that the x-axis coincides with the elastic axis, or the line of shear centers, of the element. Axes y and z are derived from the transformation applied to the global Y and Z axes as described below. The transformation matrix relating the local element axes to the global axes is derived from the local segment layout specifications. The segment geometry is specified as follows (see Fig. 5-3):

(1) The planform is first defined. Each blade segment has length, SL , along the global X-direction and chord length, c , in the global Y-direction. The sweep, Λ , defines orientation of the quarter chord line for the segment. Note that for non-zero sweep, the length of the finite element along the quarter chord length differs from the length measured along the blade X-axis. If one finite element is associated with each blade segment then the element length shall in fact be:

$$\ell = \frac{SL}{\cos \gamma} \tag{5-1}$$

where γ is the anhedral (see step 3 below).

(2) A camber and then a pre-deformation twist gradient are defined over each segment. This information is not included in the transformation matrix since it is judged that effects due to camber and pre-twist upon structural properties can be more accurately specified in the information on blade cross-section properties (see Ref. 39). Addition of camber would be reflected in the cross-sectional moments of area and pre-twisting would affect primarily the orientation of the principal axes. These parameters are directly specified in the blade cross-section input file discussed in Reference 39.

(3) Anhedral is then applied to each segment about an axis parallel to the global Y axis and passing through the left hand end (nearest to the rotor hub) of the segment. The direction of this rotation is in the negative Y-direction., i.e., positive anhedral, γ , results in the blade drooping down.

(4) Finally, collective pitch in the form of a rotation about the global X-axis is applied to the assembled structure.

This sequence of rotations is used to define the transformation matrix relating the local axes to the global ones of the RotorCRAFT code. An additional 180° rotation about the global X-axis precedes the above rotations since the local finite element z-axis is

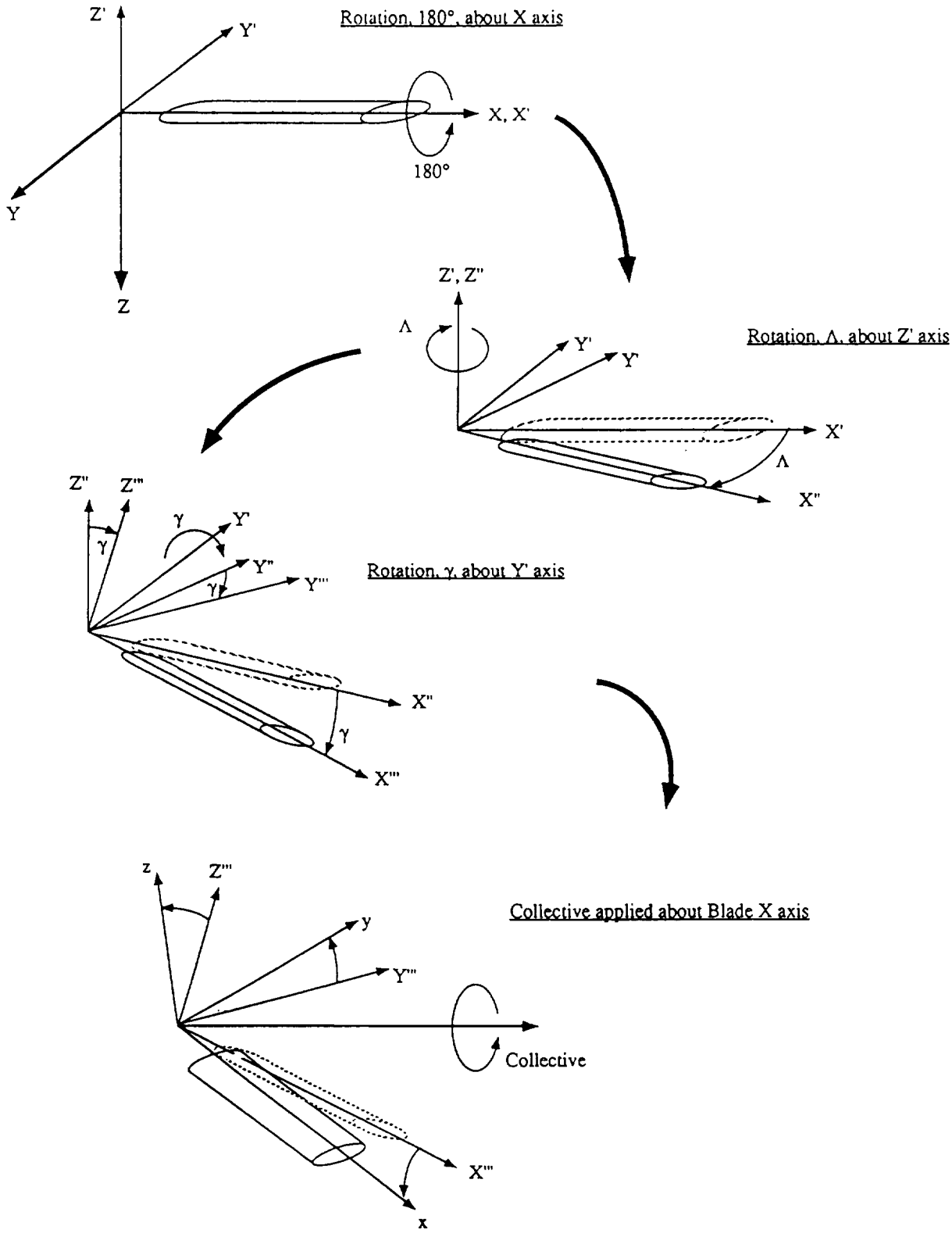

Figure 5-3. Sequence of rotations to go from blade axis system (X,Y,Z) to local element coordinate system (x,y,z).

positive upward whereas the global Z-axis is positive in the downward direction. The preceding parameters are supplied in the blade geometry input file.

From the above sequence of rotations the local and global axes are related by:

$$\begin{Bmatrix} X \\ Y \\ Z \end{Bmatrix} = \begin{Bmatrix} X_0 \\ Y_0 \\ Z_0 \end{Bmatrix} + T_C\, T_\gamma\, T_\Lambda\, T_{180^\circ} \begin{Bmatrix} x \\ y \\ z \end{Bmatrix} \tag{5.2}$$

where T_{180° , T_Λ , T_γ and T_C are the transformation matrices corresponding to the 180° rotation, sweep, anhedral and collective operations respectively, and the coordinates, $X_0Y_0Z_0$, are the global coordinates of the origin of the local axes. Here the origin lies on the elastic axis at the end of the element nearest the rotor hub. The combined matrix,

$$[\,T_{rot}\,] = T_C\, T_\gamma\, T_\Lambda\, T_{180^\circ} = \begin{bmatrix} c_\gamma c_\Lambda & c_\gamma s_\Lambda & s_\gamma \\ c_C s_\Lambda - s_C s_\gamma c_\Lambda & -c_C c_\Lambda - s_C s_\gamma s_\Lambda & s_C c_\gamma \\ s_C s_\Lambda + c_C s_\gamma c_\Lambda & -s_C c_\Lambda + c_C s_\gamma s_\Lambda & -c_C c_\gamma \end{bmatrix} \tag{5.3}$$

Note that the rotations due to deformation can also be referred to the global axes using this transformation since the deformations are assumed small and the rotations thus commute.

5.1.3 Element Degrees of Freedom

The specification of the shape functions and the fourteen degrees of freedom of each element is summarized here. Each element has two end nodes and one node at its midpoint, as shown in Figure 5-4. The degrees of freedom correspond to translational and rotational deformations at these nodes. The deformation of the element at any point is estimated by interpolation of the nodal displacements using the shape functions. Let u , v and w denote the displacements along the local x , y , and z axes respectively and let θ denote the twist deformation about the x axis. Then the generalized displacement vector is defined as:

$$\text{Lag: } \begin{Bmatrix} q_1 \\ q_2 \\ q_3 \\ q_4 \end{Bmatrix} = \begin{Bmatrix} v(0) \\ v_{,x}(0) \\ v(\ell) \\ v_{,x}(\ell) \end{Bmatrix} \qquad \text{Flap: } \begin{Bmatrix} q_5 \\ q_6 \\ q_7 \\ q_8 \end{Bmatrix} = \begin{Bmatrix} w(0) \\ w_{,x}(0) \\ w(\ell) \\ w_{,x}(\ell) \end{Bmatrix}$$

$$\text{Twist: } \begin{Bmatrix} q_9 \\ q_{10} \\ q_{11} \end{Bmatrix} = \begin{Bmatrix} \theta(0) \\ \theta(\ell/2) \\ \theta(\ell) \end{Bmatrix} \qquad \text{Axial: } \begin{Bmatrix} q_{12} \\ q_{13} \\ q_{14} \end{Bmatrix} = \begin{Bmatrix} u(0) \\ u(\ell/2) \\ u(\ell) \end{Bmatrix} \tag{5.4}$$

where the subscript $(\bullet)_{,x}$ denotes the derivative with respect to the local x axis coordinate and ℓ is the element length. Thus q_1 and q_2 refer to the displacement and corresponding slope due to bending in the y-direction at the left hand node. The corresponding right hand node deformations are q_3 and q_4 , and so forth for the other

Local Degrees of Freedom for Blade Element

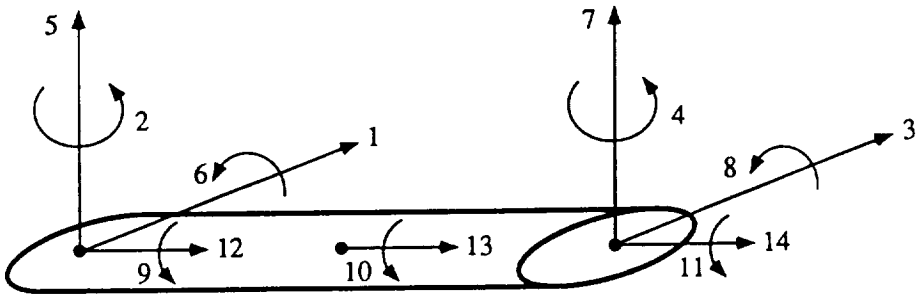

Assembly and Ordering of Global Degrees of Freedom

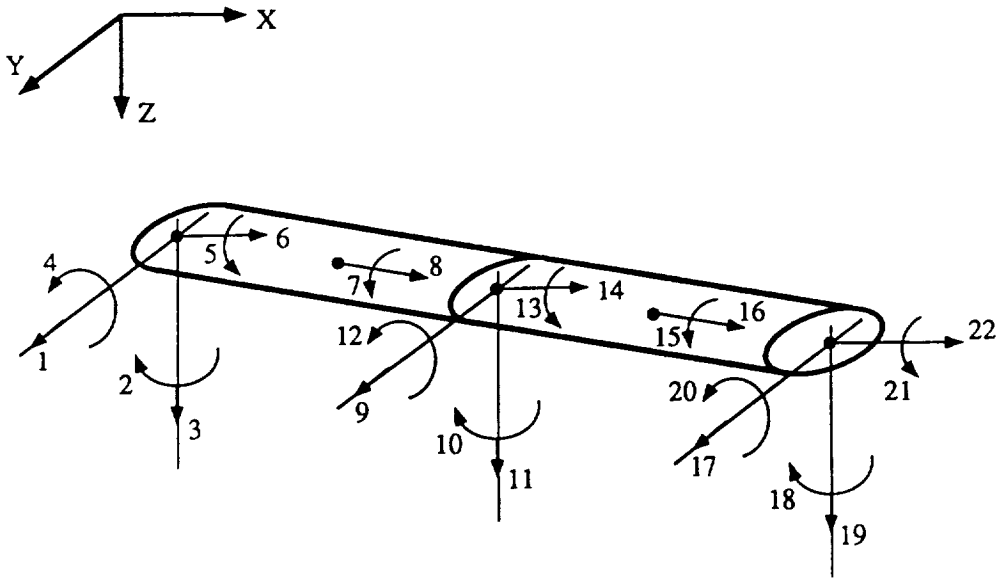

Figure 5-4. Definition of finite element degrees of freedom and schematic of the element ordering scheme.

displacements. Note that the slopes, $v_{,x}$ and $w_{,x}$, can be regarded as a small positive rotation about the local z-axis and a small negative rotation about the local y-axis respectively.

The transverse displacements, v and w, are interpolated using cubic Hermitian polynomials as is the common practice in beam finite element formulation. Quadratic polynomials are used to interpolate the torsional and axial deformations. This is the simplest element interpolation scheme yielding a consistent formulation for coupled torsion-bending (Ref. 40). Specifically:

$$v(x) = \{\Phi_3\}^T \begin{Bmatrix} q_1 \\ q_2 \\ q_3 \\ q_4 \end{Bmatrix} \qquad w(x) = \{\Phi_3\}^T \begin{Bmatrix} q_5 \\ q_6 \\ q_7 \\ q_8 \end{Bmatrix}$$

$$\theta(x) = \{\Phi_2\}^T \begin{Bmatrix} q_9 \\ q_{10} \\ q_{11} \end{Bmatrix} \qquad u(x) = \{\Phi_2\}^T \begin{Bmatrix} q_{12} \\ q_{13} \\ q_{14} \end{Bmatrix} \tag{5.5}$$

where, $$\{\Phi_3\} = \begin{Bmatrix} 1 - 3\xi^2 + 2\xi^3 \\ (\xi - 2\xi^2 + \xi^3)\ell \\ 3\xi^2 - 2\xi^3 \\ (-\xi^2 + \xi^3)\ell \end{Bmatrix} ; \quad \{\Phi_2\} = \begin{Bmatrix} 1 - 3\xi + 2\xi^2 \\ 4\xi - 4\xi^2 \\ -\xi + 2\xi^2 \end{Bmatrix} \tag{5.6}$$

and $\xi = x/\ell$. The preceding relations may be expressed in compact form as:

$$\begin{Bmatrix} v(x) \\ w(x) \\ \theta(x) \\ u(x) \end{Bmatrix} = [\Phi]\{q\} \tag{5.7}$$

where $\{q\}$ is the vector of generalized displacements and $[\Phi]$ is a (4 x 14) matrix appropriately constructed from Equations 5.5 and 5.6.

Finally in the formulation of the elemental stiffness and mass matrices it is valuable to define principal axes of the cross-section, η and ζ, which are oriented such that:

$$\int_A \eta\zeta \, dA = 0 \tag{5.8}$$

The angle β is then the angle between the local y and η axes.

The global degrees of freedom are obtained by resolving the deformations along the global axes using the transformation matrix derived previously. At an end node, all of the three translational and three rotational d.o.f. are available (since the slopes of the transverse

bending displacements correspond to rotations). Thus, the translation between the local element d.o.f.s and the global ones is straightforwardly achieved using the transformation matrix, T_{rot} :

$$\begin{Bmatrix} U \\ V \\ W \end{Bmatrix} = [T_{rot}] \begin{Bmatrix} u \\ v \\ w \end{Bmatrix} \quad ; \quad \begin{Bmatrix} R_X \\ R_Y \\ R_Z \end{Bmatrix} = [T_{rot}] \begin{Bmatrix} \theta \\ -w_{,x} \\ v_{,x} \end{Bmatrix} \tag{5.9}$$

where R_X , R_Y , and R_Z , are rotations due to deformation about the global XYZ axes respectively. At the mid-node the preceding translation is more involved since only two d.o.f., the twist and axial deformations, are available in the local axes and additional constraints are necessary to uniquely define the twist and stretch in the global directions. One approach would be to specify the four remaining local d.o.f at the mid-point by interpolating from the end-nodes using the element shape functions, i.e. evaluating $v(\ell/2)$, $w(\ell/2)$ and their slopes using Equations 5.5-5.7. These together with the local twist and extension deformations completely define the six local displacements from which the global deformations readily follow. However, it was found that this led to numerical problems in the resulting transformation matrix, since the complete element is singular for certain blade geometries. This might be expected from the observation that 18 global displacements (6 at each node) have been defined in terms of only 14 element d.o.f. Hence, the inverse transformation from global to local deformations is in fact non-unique. The approach taken here is to simply define the global deformations to coincide with the respective local ones at the mid-node, i.e.,

$$\begin{Bmatrix} q10 \\ q13 \end{Bmatrix}_G = \begin{Bmatrix} q10 \\ q13 \end{Bmatrix}_L \tag{5.10}$$

This both simplifies the transformation and results in an orthogonal element transformation matrix, i.e., if the elemental transformation which will be composed of elements of $[T_{rot}]$ is denoted by $[T_{GL}]$ so that $\{q\}_G = [T_{GL}]\{q\}_L$ then $[T_{GL}]^{-1} = [T_{GL}]^T$. An alternative procedure would be to eliminate the mid-node d.o.f. using static condensation. However, this is unnecessary in light of the small number of d.o.f.s of the fully assembled model, the additional programming complexity and the further approximation that would thus be introduced.

5.1.4 Derivation of the Element Strains and Stresses

In order to compute the elemental stiffness matrix the strains arising from the preceding displacements must be evaluated. The nonlinear expressions for the strains are stated:

$$\begin{aligned} \varepsilon_{xx} &= u_{,x} + (\Psi\theta_{,x})_{,x} + \frac{1}{2}(\eta^2 + \zeta^2)\,\theta_{,x}^2 \\ &+ \frac{1}{2} v_{,x}^2 - v_{,xx}\{\eta\cos(\beta+\theta) - \zeta\sin(\beta+\theta)\} \\ &+ \frac{1}{2} w_{,x}^2 - w_{,xx}\{\zeta\cos(\beta+\theta) + \eta\sin(\beta+\theta)\} \end{aligned} \tag{5.11a}$$

$$\gamma_{x\eta} = 2\,\varepsilon_{x\eta} = (\Psi_{,\eta} - \zeta)(\theta_{,x} + \theta_{nl}) \tag{5.11b}$$

$$\gamma_{x\zeta} = 2\,\varepsilon_{x\zeta} = (\Psi_{,\zeta} + \eta)(\theta_{,x} + \theta_{nl}) \tag{5.11c}$$

and all other strains are assumed zero. Here, θ_{nl} is a nonlinear 2^{nd} order torsion term, and $\Psi(x,\eta,\zeta)$ is the Saint Venant warping function expressing the out-of-plane displacement, u_{warp}, due to torsion:

$$u_{warp}(x,\eta,\zeta) = \Psi(x,\eta,\zeta)\,\theta_{,x} \tag{5.12}$$

The linear expressions are easily obtained from above:

$$\varepsilon_{xx} = u_{,x} + (\Psi\theta_{,x})_{,x} - v_{,xx}\{\eta\cos\beta - \zeta\sin\beta\} - w_{,xx}\{\zeta\cos\beta + \eta\sin\beta\} \tag{5.13a}$$

$$\gamma_{x\eta} = (\Psi_{,\eta} - \zeta)\theta_{,x} \quad ; \quad \gamma_{x\zeta} = (\Psi_{,\zeta} + \eta)\theta_{,x} \tag{5.13b,c}$$

These strains are expressed in terms of the vector of generalized d.o.f., $\{q\}$, and the shape functions and their derivatives w.r.t. x, by substituting for the occurrences of u, v, w, and θ using the expressions, Equations 5.11-5.13. This results in:

$$\varepsilon_{xx} = \begin{Bmatrix} -[\eta\cos\beta - \zeta\sin\beta]\{\Phi_3''\} \\ -[\zeta\cos\beta + \eta\sin\beta]\{\Phi_3''\} \\ \Psi_{,x}\{\Phi_2'\} + \Psi\{\Phi_2''\} \\ \{\Phi_2'\} \end{Bmatrix}^T \{q\} = \{B_1\}^T\{q\} \tag{5.14a}$$

$$\begin{Bmatrix} \gamma_{x\eta} \\ \gamma_{x\zeta} \end{Bmatrix} = \begin{Bmatrix} \Psi_{,\eta} - \zeta \\ \Psi_{,\zeta} + \eta \end{Bmatrix} \begin{Bmatrix} 0 \\ 0 \\ \{\Phi_2'\} \\ 0 \end{Bmatrix}^T \{q\} = \begin{Bmatrix} \{B_2\}^T \\ \{B_3\}^T \end{Bmatrix} \{q\} \tag{5.14b,c}$$

The corresponding stresses are derived from the Hooke's Law:

$$\sigma_{xx} = E\,\varepsilon_{xx} \tag{5.15a}$$

$$\sigma_{x\eta} = G\,\gamma_{x\eta} \quad ; \quad \sigma_{x\zeta} = G\,\gamma_{x\zeta} \tag{5.15b,c}$$

5.2 Derivation of the Stiffness and Mass Matrices Via Hamilton's Principle

The discussion above defines the relationships for stresses and strains for the current F.E. formulation. This section deals with the generation of the mass and stiffness matrices that permit these elements to be coupled into the equations of motion of the rotor blade. There are several ways of obtaining the stiffness and mass matrices. Here the Extended Hamilton's Principle has been applied. One begins by deriving expressions for the kinetic energy and the strain energy of each element. Any remaining forces not contained in the kinetic and strain energies are accounted for by an external virtual work term. Application of the variational calculus to the Lagrangian, $\mathcal{L}$ = (Kinetic Energy) - (Strain Energy), yields the equations of motion that govern the blade dynamics. The variation of the strain energy in this case is identical to the expression for the internal virtual work. Since the internal virtual work can be written down directly, it is unnecessary to execute the intermediate step of obtaining an expression for the strain energy. Hence, the actual computation of the strain energy is circumvented in the analysis to follow.

5.2.1 Evaluation of the Finite Element Stiffness Matrix

The structural stiffness matrix K is composed of a sum of three terms K_E , K_r, and K_T , where K_E is the usual material stiffness matrix obtained from the internal virtual work, K_r accounts for additional geometric stiffening due to blade rotation, and K_T is derived from the variation of the kinetic energy. K_r is derived by expressing the forces and moments due to rotation explicitly and regarding these as externally applied loads that are accounted for by an external virtual work term. This approach is frequently used in buckling analysis and bending and torsion problems where axial forces are present. The geometrically nonlinear terms in the strain expressions are of importance since axial forces are present and result in significant additional stiffening of the blade. If moderate deformations are permitted (i.e. moderate rotations but small strains) then the rotational forces and moments are sufficiently well specified using only linear geometrical considerations.

The internal virtual work due is given by:

$$W^i = \int_V \sigma_{xx} \cdot \delta\varepsilon_{xx} + \sigma_{x\eta} \cdot \delta\gamma_{x\eta} + \sigma_{x\xi} \cdot \delta\gamma_{x\xi} \; dV \qquad (5.16)$$

Substituting for the stresses and breaking up the volume integral:

$$W^i = \int_0^{\ell} \{ \int_A E\varepsilon_{xx} \cdot \delta\varepsilon_{xx} + G\gamma_{x\eta} \cdot \delta\gamma_{x\eta} + G\gamma_{x\xi} \cdot \delta\gamma_{x\xi} \; dA \} \; dx \qquad (5.17)$$

Substituting for the strains using Equation 5.14 and performing the integrations results in:

$$W^i = \{\delta q\}^T [K_E] \{q\} \qquad (5.18a)$$

where the desired stiffness matrix is

$$[K_E] = \int_0^{\ell} \{ \int_A E\{B_1\}\{B_1\}^T + G(\{B_2\}\{B_2\}^T + \{B_3\}\{B_3\}^T)\, dA \}dx \tag{5.18b}$$

The construction of $[K_E]$ requires a sequence of integrations, the first being an area integration over the area of cross-section at a given station, x, along the element, and the second being the integral along the length of the element. Evaluation of the area integral results in expressions containing various properties of cross-section multiplied by the shape functions and their derivatives w.r.t. x. These properties include the cross-sectional area, moments of area, area centroids relative to the η and ζ axes, and a total of nine integrals involving the warping function, Ψ. The finite element implementation employed in RotorCRAFT does not compute these properties, but instead requires that the various cross-sectional area integrals be input directly via the blade cross-section input file. The finite element code requires that these properties be specified at the end nodes of each element and assumes that they vary linearly between the end nodes. The final integration along the element length involves products of the shape functions and their derivatives and is effected numerically using Gaussian integration. A list of the cross-section area integrals required in the analysis is given in Reference 39.

In order to determine the contributions to the stiffness matrix and the nodal forces due to blade rotation one first defines the position vector of a point on the blade in blade coordinates,

$$\mathbf{R}(X,Y,Z) = X\mathbf{I}+Y\mathbf{J}+Z\mathbf{K}$$

$$\text{or,} \quad \begin{Bmatrix} X \\ Y \\ Z \end{Bmatrix} = \begin{Bmatrix} X_0 \\ Y_0 \\ Z_0 \end{Bmatrix} + [T_{rot}] \begin{Bmatrix} x_{ie} + u \\ v+\eta\cos(\beta+\theta)-\zeta\sin(\beta+\theta) \\ w+\eta\sin(\beta+\theta)+\zeta\cos(\beta+\theta) \end{Bmatrix} \tag{5.19a}$$

which in local coordinates is,

$$\begin{Bmatrix} x \\ y \\ z \end{Bmatrix} = [T_{rot}]^T \begin{Bmatrix} X_0 \\ Y_0 \\ Z_0 \end{Bmatrix} + \begin{Bmatrix} x_{ie} + u \\ v+\eta\cos(\beta+\theta)-\zeta\sin(\beta+\theta) \\ w+\eta\sin(\beta+\theta)+\zeta\cos(\beta+\theta) \end{Bmatrix} \tag{5.19b}$$

where x_{ie} is the distance along the elastic axis of the element containing the point. Then the body force at any point on the blade due to rotation is:

$$\mathbf{f} = -\rho\,(\Omega\mathbf{K}) \times \{(\Omega\mathbf{K}) \times \mathbf{R}\} \tag{5.20}$$

where ρ is the density of the blade material, and the unit vectors are aligned with the global axes. When expressed in the local co-ordinate system of a particular element, this becomes,

$$\begin{Bmatrix} f_x \\ f_y \\ f_z \end{Bmatrix} = \Omega^2 [T_{rot}]^T \left(\begin{Bmatrix} X_0 \\ Y_0 \\ 0 \end{Bmatrix} \right.$$

$$\left. + \begin{bmatrix} 1 & 0 & 0 \\ 0 & 1 & 0 \\ 0 & 0 & 0 \end{bmatrix} [T_{rot}] \begin{Bmatrix} x_{ie} + u \\ v+\eta\cos(\beta+\theta)-\zeta\sin(\beta+\theta) \\ w+\eta\sin(\beta+\theta)+\zeta\cos(\beta+\theta) \end{Bmatrix} \right) \tag{5.21}$$

The moment about a point on the element elastic axis, $\mathbf{R}_{ea} = X_{ea}\mathbf{I}+Y_{ea}\mathbf{J}+Z_{ea}\mathbf{K}$, due to the rotational force acting on a volume element located at $\mathbf{R}$ somewhere on the blade is,

$$\mathbf{m} = (\mathbf{R} - \mathbf{R}_{ea}) \times \mathbf{f}\, dA\, dx \tag{5.22}$$

The net forces and moments at a point on the elastic axis defined by x_{ea} are:

$$\mathbf{F} = \int_{X_{ea}}^{R} \{ \int_A \mathbf{f}(x,y,z)\, dA \}\, dX \tag{5.23a}$$

$$\mathbf{M} = \int_{X_{ea}}^{R} \{ \int_A [\mathbf{R}(X,Y,Z) - \mathbf{R}_{ea}(X_{ea},Y_{ea},Z_{ea})] \times \mathbf{f}(X,Y,Z)\, dA \}\, dX \tag{5.23b}$$

where R is the value of X_{ea} at the blade tip. The domain of integration extends from X_{ea} to the blade tip since the net force and moment vectors vanish at the blade tip.

The virtual work expression for the net blade rotation forces undergoing virtual deformations that accounts for the geometric stiffening effects is stated (see Ref. 40):

$$W_r^e = \int_0^{\ell} \{F_x\,(v'\delta v'+w'\delta w') + M_{yy}\,\delta(v''\theta) + M_{zz}\,\delta(w''\theta)$$

$$+ Q\theta'\delta(\theta') + \frac{1}{2} M_{xx}\,\delta(v''w'-w''v') \}\, dx_{ie} \tag{5.24}$$

Here,

$$Q = \frac{1}{A} \int_A F_x\,(y^2 + z^2)\, dA \tag{5.25}$$

and the terms, F_x, M_x, M_y, and M_z are simply the local components of the net forces and moments due to rotation summed over the portion of blade lying outboard of the point x_{ie} on the elastic axis. Note that the first term in Equation 5.24 represents the usual

additional stiffening due to an axial force. The virtual work contribution for this first term may be viewed as a differential moment arising from structural deformation, $dM_z = F_x(v'dx)$ and $dM_y = F_x(-w'dx)$, moving through virtual rotations, $\delta v'$ and $\delta(-w')$. Note also that neglecting the virtual work term, Equation 5.24, will lead to totally erroneous results since geometric stiffening plays a major role in the range of angular velocities typical for helicopters. In fact, failure to retain of Equation 5.24 results in a softening of the blade, which is clearly incorrect.

Equations 5.19 to 5.24 contain all of the information necessary for the computation of $[K_T]$. The remaining procedure is laborious, but straightforward and is briefly summarized below:

• Resolve all forces, moments, and position vectors appearing in the above equations, Equations 5.19 to 5.24, in the local element coordinate system.

• Substitute for all occurrences of u, v, w, and θ, and their derivatives using Equations 5.5 and 5.4.

• Replace $\sin(\beta+\theta)$ and $\cos(\beta+\theta)$ by the small θ approximations.

• Substitute for f, m_x, F_x, M, and Q in Equation 5.24 and discard all terms of order higher than 2.

• Carry out the cross-section area integrations. As in the computation for $[K_E]$, this area integral can be directly expressed in terms of certain cross-section properties. Since the blade material density, ρ, is now present in the analysis these cross-section properties will be quantities such as the mass per unit length, cross-sectional center of mass, torsional moment of inertia per unit length, etc. The complete list of parameters needed is given in Reference 39.

• Finally, evaluate Equation 5.24. Judicious use of integration by parts where possible simplifies the evaluation of Equation 5.25. For example, the first term,

$$\int_0^{\ell} \{F_x\,(v'\delta v'+w'\delta w')\,dx_{ie} = \left[F_x(x_{ie}) \int_0^{x_{ie}} v'\delta v'+w'\delta w'\,d\mu\right]_{x_{ie}=0}^{x_{ie}=\ell}$$

$$+ \int_0^{\ell} f_x \left\{ \int_0^{x_{ie}} (\,v'\delta v'+w'\delta w'\,)\,d\mu \right\} dx_{ie} \qquad (5.26)$$

The quantity $(v'\delta v'+w'\delta w')$ is easily evaluated from Equation 5.7 in terms of the element shape functions and the generalized vector of nodal displacements, $\{q\}$. Thus the integral contained in the brackets $\{\bullet\}$ can be written down analytically. The final integration along the element from $x_{ie}=0$ to $x_{ie}=\ell$ is done by Gaussian integration.

• The final expression for the virtual work due to blade rotation is of the form:

$$W_r^e = \{q\}^T [K_r] \{q\} \tag{5.27}$$

where $[K_r]$ is the additional geometric stiffening matrix and is proportional to Ω^2 .

5.2.2 Derivation of Element Mass Matrix

The mass matrix is derived from the Kinetic Energy expression for the element. The velocity of any point on the blade is a combination of deformation velocities and velocities due to the steady blade rotation:

$$\dot{\mathbf{R}} = \frac{\partial \mathbf{R}}{\partial t} + \Omega \mathbf{K} \times \mathbf{R} \tag{5.28a}$$

where $\partial(\bullet)/\partial t$ refers to rates of change occurring relative to axes rotating with the blade.

The components of $\dot{\mathbf{R}}$ in the local element coordinates are:

$$\begin{Bmatrix} \dot{R}_x \\ \dot{R}_y \\ \dot{R}_z \end{Bmatrix} = \begin{Bmatrix} \dot{u} \\ \dot{v} - [\eta \sin(\beta+\theta) + \zeta \cos(\beta+\theta)]\dot{\theta} \\ \dot{w} + [\eta \cos(\beta+\theta) - \zeta \sin(\beta+\theta)]\dot{\theta} \end{Bmatrix}$$

$$+ [T_{rot}]^T \begin{bmatrix} 0 & -\Omega & 0 \\ \Omega & 0 & 0 \\ 0 & 0 & 0 \end{bmatrix} \left(\begin{Bmatrix} X_0 \\ Y_0 \\ Z_0 \end{Bmatrix} + [T_{rot}] \begin{Bmatrix} x+u \\ v+\eta\cos(\beta+\theta) - \zeta\sin(\beta+\theta) \\ w+\eta\sin(\beta+\theta) + \zeta\cos(\beta+\theta) \end{Bmatrix} \right) \tag{5.28b}$$

The kinetic energy for the element is,

$$KE = \frac{1}{2} \int_0^{\ell} \int_A \rho \{ \dot{R}_x^2 + \dot{R}_y^2 + \dot{R}_z^2 \} \, dA \quad dx \tag{5.29}$$

Again the actual computation of the knietic energy is lengthy, but straightforward. One replaces the sin(•) and cos(•) by their small θ angle approximations, substitutes for the occurrences of u, v, w, and θ and their time derivatives in Equation 5.28 and inserts the resulting expressions for $\dot{R}_x$, $\dot{R}_y$, and $\dot{R}_z$ into Equation 5.29. The time derivatives:

$$\begin{Bmatrix} \dot{v} \\ \dot{w} \\ \dot{\theta} \\ \dot{u} \end{Bmatrix} = [\Phi]\{\dot{q}\} \tag{5.30}$$

Performing the integration over the cross-sectional area, A , in Equation 5.29 yields an expression containing mass properties of the cross-section similar to those cited previously in the computation of the stiffness matrix due to blade rotation. The kinetic energy now has the following form:

$$\text{K.E.} = \frac{1}{2}\int_0^{\ell} \{\dot{q}\}^T[A_2]\{\dot{q}\} + \Omega\{\dot{q}\}^T[A_1]\{q\} + \Omega^2(\{q\}^T[A_0]\{q\} + \{q\}^T\{B_0\} + C_0)\, dx \tag{5.31}$$

where $[A_2]$, $[A_1]$, $[A_0]$, $\{B_0\}$, and C_0 are appropriately dimensioned and are functions of the element interpolation polynomials and cross-sectional properties. The standard application of the variational calculus in Hamilton's Principle then results in:

$$\delta(\text{K.E.}) = -\{\delta q\}^T \int_0^{\ell} [A_2]\{\ddot{q}\} + \Omega([A_1]-[A_1]^T)\{\dot{q}\} - \Omega^2([A_0]\{q\}+\{B_0\})\, dx$$

or,
$$\delta(\text{K.E.}) = -\{\delta q\}^T ([M]\{\ddot{q}\} + [G]\{\dot{q}\} + [K_T]\{q\} - \{f_{rot}\}) \tag{5.32}$$

where,
$$[M] = \int_0^{\ell} [A_2]\, dx \quad ; \quad [G] = \Omega \int_0^{\ell} [A_1]-[A_1]^T\, dx$$

$$[K_T] = \Omega^2 \int_0^{\ell} [A_0]\, dx \quad \text{and} \quad \{f_{rot}\} = \Omega^2 \int_0^{\ell} \{B_0\}\, dx \tag{5.33}$$

[M] is recognized as the mass matrix for the element, [G] is an anti-symmetric gyroscopic matrix, $[K_T]$ contributes to the stiffness matrix, and $\{f_{rot}\}$ represents the nodal forces due to blade rotation. It is pointed out that the matrix, $[K_T]$, and nodal force vector, $\{f_{rot}\}$, could also be obtained by considering the body force due to blade rotation, **f**, as a distributed external force. Imposing virtual displacements upon the blade under this distributed load results in the formation of an external work term:

$$W_r^e = \int_0^{\ell} \int_A f_x \delta u + f_y \delta v + f_z \delta w + (y f_z - z f_y) \delta\theta \, dA \, dx_{ie} \qquad (5.34)$$

Substituting for the forces, f_x, f_y, f_z via Equation 5.21, replacing the deformations, u , v , w , and θ by their approximations, Equation 5.5, and evaluating the integral reproduces the $[K_T]$ and $\{f_{rot}\}$ derived via the Hamilton's Principle.

It is easy to show that the gyroscopic term $[G]\{\dot{q}\}$ does no work, i.e., it introduces no damping. The elements of [G] are small in comparison to the corresponding mass and stiffness matrix components, and their contribution to the overall solution is to shift the natural frequencies slightly and introduce a small degree of coupling between the modes obtained when neglecting [G] . If the gyroscopic terms were to be retained in the eigencalculation for mode shapes and frequencies, this would entail substantial increase in the programming complexity involved in the eigencalculation. It was judged that the additional computational effort involved in accounting for gyroscopic terms is unjustified in light of their relative unimportance in the context of helicopter forward flight dynamic analysis. Hence, in RotorCRAFT the gyroscopic terms have been neglected.

5.2.3 Assembly of the Global Mass and Stiffness Matrices

The element matrices obtained above are employed in the formation of the corresponding global matrices for the complete helicopter blade. The assembly process involves two sub-procedures: the first involves referring the elemental matrices and nodal forces to the global axes, and the second defines the array indexing that relates the local degrees of freedom for each element to the global ones.

Rotation of the element matrices and nodal forces into a global coordinate frame is accomplished in the standard manner:

$$[K_{global}] = [T_{GL}][K_{local}][T_{GL}]^T \; ; \; [M_{global}] = [T_{GL}][M_{local}][T_{GL}]^T$$

$$\{F^{rot}\}_{global} = \{F^{rot}\}_{local}[T_{GL}]^T$$

as may be easily verified by noting that the kinetic and potential energies and the virtual work are independent of the choice of reference frame. Here, $[T_{GL}]$ is the transformation matrix described in Section 5.2 relating local and global generalized d.o.f.: $\{X_{global}\} = [T_{GL}]\{q_{local}\}$.

The blade elements are then laid end to end in sequence from blade root to blade tip. Global deformations are defined as outlined in Equations 5.9 and 5.10. However, the ordering of the global degrees of freedom is different from the local ones, Equation 5.4.

Each element degree of freedom is associated with a global one via an indexing array or splay matrix, C(k,ie) , where k is the local degree of freedom (k=1,2,...14) , ie is the element number, and C(k,ie) is the global degree of freedom. Having specified a C(k,ie) for each element then the global matrices may be constructed by 'splaying' components of the elemental mass and stiffness matrices into their corresponding positions in the global matrices. For example, the [i,j] entry of the elemental stiffness matrix for finite element, ie, is added to the [C(i,ie),C(j,ie)] entry of the global stiffness matrix. In like manner, the global nodal force vector is built up from nodal forces for each element.

It remains to specify the actual ordering of the global degrees of freedom. Degrees of freedom are numbered upwards starting at the blade root. Using the definitions for global displacements and rotations given in Section 5.2, Equations 5.9 and 5.10, the global degrees of freedom are summarized in Table 5-1 (see also Fig. 5-4).

Thus far, the boundary conditions at the root have not been imposed, and some of the root degrees of freedom are eliminated when these are applied. For articulated blades, it is implicitly assumed in RotorCRAFT that the blade is freely hinged in both flap and lag directions, but that the remaining degrees of freedom at the root - the three translational displacements and the twist about the X axis - are constrained. Thus, the rows and columns of the global mass and stiffness matrices corresponding to these four degrees of freedom are removed prior to conducting the modal analysis. For cantilevered blades, by definition all root deformations are zero and thus all six degrees of freedom at the root are similarly eliminated. However, although the rows and columns corresponding to the constrained degrees of freedom are removed when computing the natural blade modes, they are employed when determining the inertia forces introduced due to cyclic pitching.

Let the global mass and stiffness matrices for the blade be given by:

$$M = \begin{bmatrix} M_{cc} & : & M_{cr} \\ \cdots & \cdots & \cdots \\ M_{rc} & : & M_{rr} \end{bmatrix} \quad ; \quad K = \begin{bmatrix} K_{cc} & : & K_{cr} \\ \cdots & \cdots & \cdots \\ K_{rc} & : & K_{rr} \end{bmatrix} \tag{5.35}$$

where the matrices have been partitioned into submatrices associated with constrained and unconstrained nodal degrees of freedom respectively. Submatrices, $[M_{rr}]$ and $[K_{rr}]$ are the mass and stiffness matrices for unconstrained deformations and are used in computing modal properties. The constrained degrees of freedom are associated with the translational deformations, U , V , and V , and also the twist rotation, R_X , at the blade root. For cantilevered beams, the constrained degrees of freedom also include the rotations, R_Y and R_Z . Of particular interest are the matrix partitions associated with the root twist displacement, θ_C , which shall be required for computing the effects of cyclic pitch. Although the twist deformation is zero at the root, it is clear that there is a finite rigid body rotation occurring at the root due to cyclic pitching and this will introduce an associated inertia term into the equations of motion governing the remaining degrees of freedom. This is expanded upon in Appendix A.

TABLE 5-1

Specification of the Global Degrees of Freedom For Element, ie.

	Global Deformation	Degree of Freedom
Left-hand node of element, ie:	V	Q_{8ie-7}
	R_Z	Q_{8ie-6}
	W	Q_{8ie-5}
	R_Y	Q_{8ie-4}
	R_X	Q_{8ie-3}
	U	Q_{8ie-2}
Mid-node of element, ie:	q_{10}	Q_{8ie-1}
	q_{13}	Q_{8ie}
Right-hand node of element, ie:	V	Q_{8ie+1}
	R_Z	Q_{8ie+2}
	W	Q_{8ie+3}
	R_Y	Q_{8ie+4}
	R_X	Q_{8ie+5}
	U	Q_{8ie+6}

5.3 Computation of Modal Properties

The dynamic analysis in the RotorCRAFT code is formulated in terms of the response modes of the blade. Thus, the information contained in the blade mass and stiffness matrices is used to obtain a set of mode shapes and their corresponding modal frequencies and masses. The standard computation of these modes entails solving the generalized eigenvalue problem:

$$[K_{rr}]\{x_i\} = \omega_i^2[M_{rr}]\{x_i\} \tag{5.36}$$

where ω_i is the natural frequency of the i-th mode, and $\{x_i\}$ is the corresponding eigenvector, or, mode shape.

Equation 5.36 is solved using the generalized Jacobi iteration method which is efficient and accurate, and can be programmed compactly. The scheme, which is described in Reference 42, solves for all of the eigenvalues/vectors simultaneously. These are then ordered in ascending frequency, and sorted into the dominant type of deformation present in each mode: bending (flap and lag), torsion or extension. The number of modes of each type retained in the dynamic analysis in RotorCRAFT is specified by the user.

Appendix A contains a description of the approach used for carrying out the computation of the generalized masses and the natural frequencies associated with the rotor blade. Additional information on the input required for the RotorCRAFT dynamic model can be found in Reference 39. Documentation there and in the Appendix discusses the requirements for input to the dynamic analysis as well as the provision for optional computation of modal properties given appropriate inputs on the blade's cross-sectional properties.

6. STRUCTURE AND OPERATION OF THE FORWARD FLIGHT AIRLOADS CODE

6.1 Outline

As discussed above, the RotorCRAFT analysis is designed to solve for the aerodynamic loads on isolated helicopter rotors in steady forward flight. Presently, the rotor hub is assumed to be fixed in space and the rotor shaft is assumed to be oriented at a fixed angle with respect to the free stream. Given this and the absence of interference effects from bodies or other rotors, the analysis in its present form is most easily characterized as a simulation of wind tunnel experiments. This circumstance has conditioned the choice of solution method, which is directed at obtaining periodic solutions for the wake geometry, the blade motion, and the aerodynamics loads. This objective was judged to be appropriate for this particular effort, given the the focus on steady-state forward flight. The "transient" solution achieved during the iteration process does not represent a time-accurate calculation of rotor aerodynamics; only the converged result can be considered physically valid and consistent. The approach used to obtain this converged result is now described.

The outermost loop in the iteration process is the computation of the evolution of the wake geometry over one rotor revolution with blade motion and aerodynamic loading fixed. The simulation is ordinarily run for a discrete number of rotor revolutions, and between each revolution the cyclic pitch inputs and the collective are adjusted to meet the conditions specified by the user for thrust and first harmonic flapping response (ordinarily, zero first harmonic flapping is desired, though many experimental cases in the literature have been run with nonzero flapping). This trim procedure represents the second loop within the overall iteration. Finally, the innermost loop is the calculation of the blade motion that is consistent with the current values of the control settings; this calculation is carried out using the dynamic model described in Section 5 and is performed assuming the wake-induced downwash is fixed at the most recent estimate obtained from the outer loop involving the wake evolution.

The first step in starting this overall procedure is to determine an initial estimate for the blade motion and the cyclic controls, using a simple strip theory aerodynamic loads analysis and an estimate of wake-induced velocity based on a simple, prescribed downwash distribution. Using the blade motion and bound circulation estimates so generated, the first loop of the analysis proceeds, beginning with a kinematic wake whose geometry is determined by the free stream and the downwash at the rotor disk. The wake then is allowed to evolve for one rotor revolution, during which the time history of the wake-induced flow field at each evaluation point on the rotor blade is computed and stored. At the end of this revolution, this time history of wake-induced flow is passed to a trim and dynamics routine that updates the control settings and the blade motion solution to be consistent with the free wake flow field.

Using the updated downwash, the program then checks to see if the first harmonic components of rigid flapping are within a specified tolerance of the desired level. If not, the cyclic pitch is adjusted and the blade motion calculation repeated until they are. The iteration history is tracked and previous results are used to accelerate the convergence process. Once trim has been achieved, the thrust is checked to see if it lies within a specified tolerance of the desired level. If not, the collective is adjusted and the steps just above are repeated until this condition is met. This process has proved to be sufficiently robust to handle a wide variety of rotor configurations, as will be evident from the sample cases presented below. A flow chart of the sequence of events in the trim cycle is given in

Figure 6-1; more information in the input requirements for the analysis can be found in Reference 39.

6.2 Blade Dynamics and Trim Procedures

The following discussion supplements the outline just above and provides additional background information on the operation of the analysis, in particular methods used to obtain the rotor trim. The determination of the initial blade motion and control settings (collective and cyclic) to be used with the free wake rotor calculation ordinarily proceeds in two steps. First, after input and initialization, the strip theory aerodynamic analysis of the rotor blade is used in conjunction with a harmonic balance dynamic analysis to determine a preliminary estimate of the blade motion. This calculation uses a simple inflow downwash model similar to that in from Reference 21 when determining generalized forces:

$$w(r,\psi) = \left(\frac{C_T}{2\mu}\right)\Omega R\left(1 + \sqrt{2}\left(\frac{r}{R}\right)\cos\psi - \mu\alpha_s\right) \tag{6.1}$$

The harmonic balance solver invokes a blade dynamic model involving only rigid flapping and first elastic bending. The calculation is particularly straightforward because of the use of approximate mode shapes and because of a simple treatment of compressibility effects that allows analytical evaluation of the generalized forces on the blade. Higher bending modes and torsional deflection are assumed to be zero for the purpose of this preliminary calculation.

This strip theory/harmonic balance calculation contains an internal trim iteration so that the blade motion, bound circulation, and control settings are derived for the specified flight condition . These values are used to initialize the appropriate quantities for the full free wake/vortex lattice/finite element calculation. It is sometimes desirable to bypass this strip theory initialization for repeat calculations at a specified flight condition since the trim control settings from a prior run will usually provide a better starting point for the overall trim calculation than an initialization based on the simple flow field model described above. The implementation of this option is described in Reference 39.

This strip theory blade dynamics analysis was developed originally for the work described in Reference 13 and was retained as the primary source for blade motion calculations through the work reported in Reference 15. It has now been superseded by the dynamic model described in Section 5, though it may still be invoked to provide blade motion information for free wake calculations, if desired. This capability is useful for illustrating the effects of the dynamic model of the blade on airload calculations.

This preliminary solution for blade motion is then used as input to the second portion of the initialization procedure. The trim solution derived from strip theory is used to drive the vortex lattice model of the rotor blade, but with the wake-induced downwash still assumed to be in the form given in Equation 6.1. The use of the vortex lattice model will produce new generalized forces, and so a new blade motion and trim solution must be obtained to produce a consistent calculation.

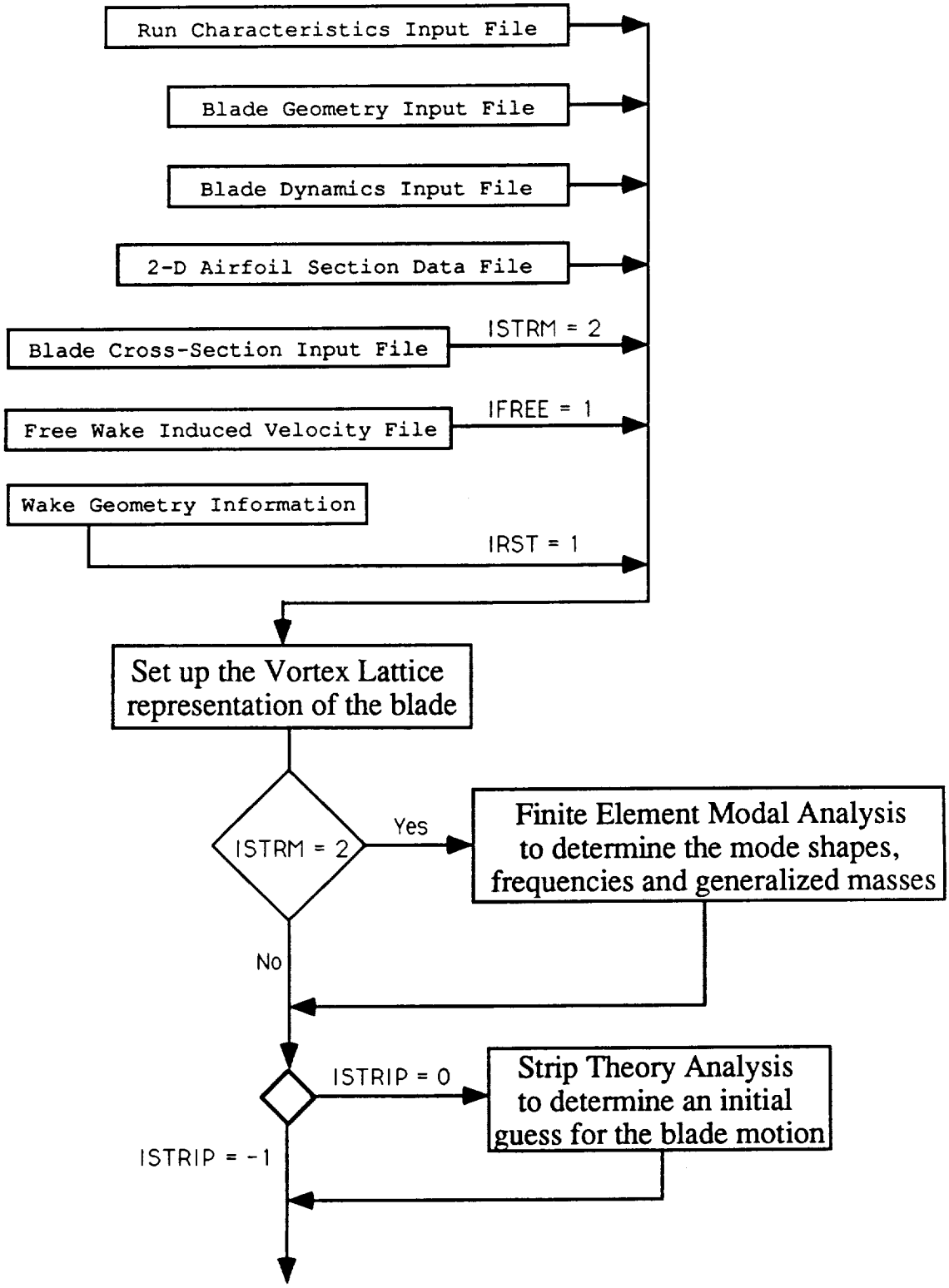

Figure 6-1. Flow chart of the RotorCRAFT analysis.

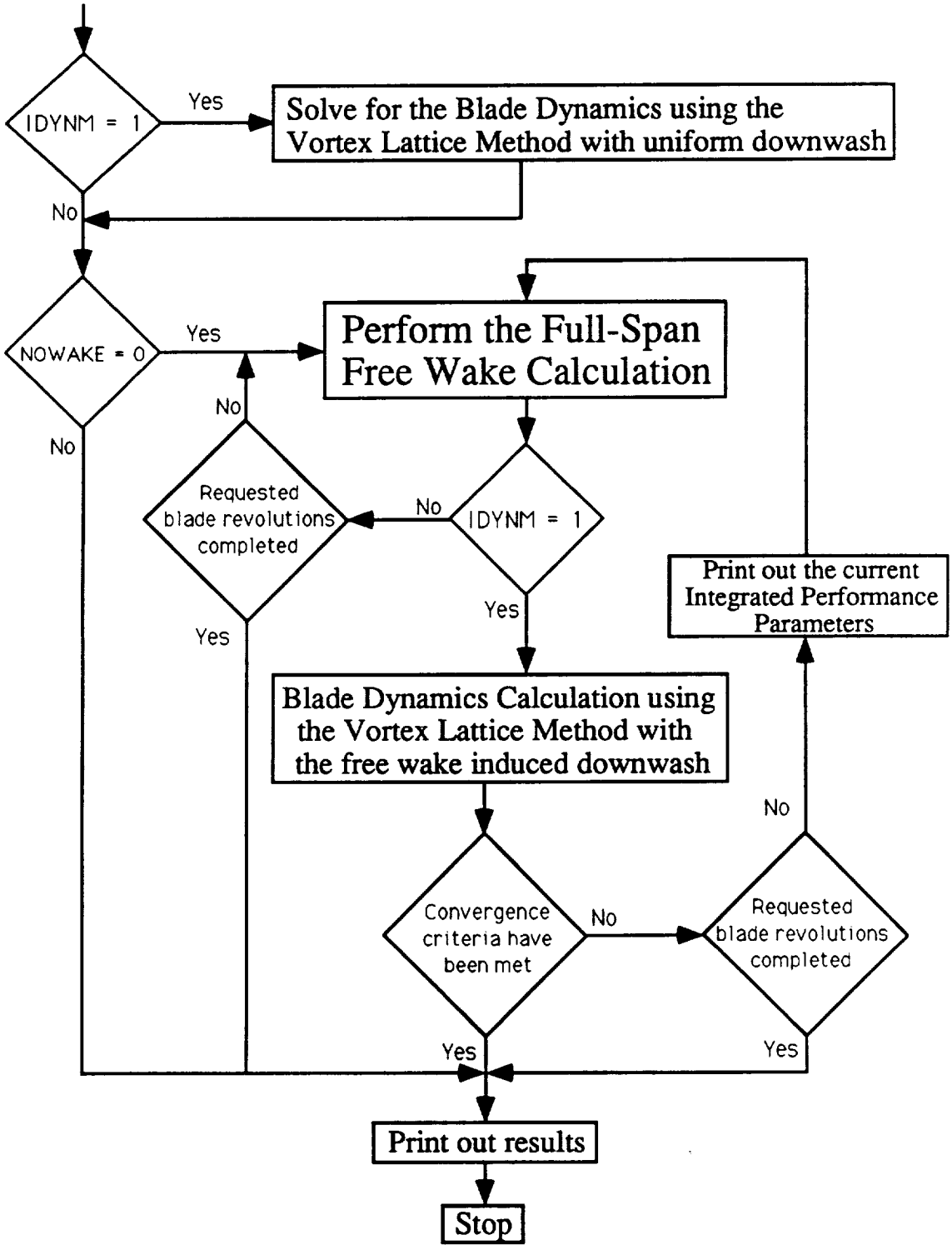

Figure 6-1 (Cont'd). Flow chart of the RotorCRAFT analysis.

To obtain this solution, a call is made to a harmonic analysis solution that is more general than the simple harmonic balance solver described above, one that can accommodate numerically computed generalized force distributions along the blades. This solution method is similar in most respects to that described in Reference 5 . The structural displacement of the blade is represented by a summation of orthogonal modes, each satisfying the equation of motion:

$$\frac{\partial^2 \eta_i}{\partial \psi^2} + \omega_{\eta_i}^2 \eta_i = G_i \left(\eta_i , \frac{\partial \eta_i}{\partial \psi} , \psi \right) \qquad (6.2)$$

where η_i is the modal amplitude of the ith mode $\phi_i(r)$. The structural displacement is

$$z(r,\psi) = \sum_i \phi_i(r)\, \eta_i(\psi) \qquad i = 1, 2, ...N_m \qquad (6.3)$$

Here, ω_{η_i} is the frequency (normalized by the blade rotation Ω) of mode $\phi_i(r)$ and G_i is the corresponding generalized force. The G_i term contains the aerodynamic damping. In order to solve the equation using the this approach, damping is required on the left-hand side of the equation. An additional artificial damping term , c_i , is added to both sides of the equation, leaving

$$F_i = G_i + [c_i] \frac{\partial \eta_i}{\partial \psi} \qquad (6.4)$$

The formulation is simplified by Fourier transforming both the displacements η_i and the generalized forces F_i . In the following, the modal subscript 'i' is dropped for clarity, but the procedure is applied to each of the modal responses. The solution procedure ordinarily starts with an initial guess for the harmonics of the Fourier transformed displacements, $\tilde{\eta}_n$, based on the strip theory calculation mentioned above. The modal amplitude η_j and amplitude rates $\partial\eta_j/\partial\psi$ at the azimuth j are obtained from the inverse Fourier transform of the $\tilde{\eta}_n$'s . Given the values of η_j and $\partial\eta_j/\partial\psi$, a new value for the generalized force F_j is determined at this azimuth using numerical integration of the generalized forces over the vortex lattice. The difference between this new value and the previous value of F_j creates a difference in each of the harmonics of the Fourier transformed generalized forces, $\Delta\tilde{F}_n$, which is used to update the corresponding $\tilde{\eta}_n$'s . This process is then repeated at the next azimuth j+1 using the the new $\tilde{\eta}_n$'s. After a complete revolution, the RMS change in the $\tilde{\eta}_n$'s is evaluated over the previous cycle and the process is stopped if it is less than 1.0% of the RMS value of the $\tilde{\eta}_n$'s themselves.

With the blade dynamics converged, the issue of selecting the pitch controls to achieve the desired trim state can be addressed. The options are:

i) For thrust: fixed collective or fixed C_T with collective adjusting until the requested C_T is obtained.

ii) For first harmonic flapping angles: fixed cyclic inputs A_{1w} and B_{1w} or fixed first harmonic flapping a_{1s} and b_{1s} , with A_{1w} and B_{1w} adjusting until the selected values for a_{1s} and b_{1s} are obtained.

Once the blade motion has been determined, the problem of adjusting cyclic pitch to achieve the requested level of flapping is addressed. The partial derivatives $\partial a_{1s}/\partial A_{1w}$, $\partial b_{1s}/\partial A_{1w}$, $\partial a_{1s}/\partial B_{1w}$, and $\partial b_{1s}/\partial B_{1w}$ are determined numerically. If the first harmonics of the rigid flapping mode differ from the user requested values of a_{1s} and b_{1s} by more than a specified tolerance, A_{1w} and B_{1w} are adjusted according to the calculated partial derivatives and the blade dynamics equations are re-solved. This process is repeated until the convergence condition has been satisfied. Once this step has been completed successfully, the thrust coefficient is checked to see if it differs from the desired value by less than a percentage specified by the user. If it does not, the collective is adjusted and the steps just described are repeated until it does. The partial derivative $\partial C_T/\partial\theta_0$ is calculated while iterating in order to facilitate rapid convergence

All of the steps described to this point in the section are carried out between revolutions of the main rotor wake. The trim process proceeds with a fixed induced velocity distribution from the previous cycle of the wake calculation. After the blade dynamics calculation is complete, the new blade motion and bound circulation distribution around the azimuth are available for application to the next cycle of the free wake calculation. The new free wake cycle is performed using updated information on wake-induced velocity on the blade and around the azimuth. Then the blade dynamics is repeated once again.

Currently, the user has the option of applying overall convergence criteria to the complete calculation, as well. The criteria presently in place allow the calculation to be terminated when the thrust coefficient and the cyclic pitch settings are repeatable from one free wake revolution to the next within a specified tolerance. Reference 39 contains substantial additional discussion of the actual implementation and operation of these procedures within the context of the RotorCRAFT code.

7. DATA CORRELATION STUDIES

7.1 Objective

As is clear from the discussion in Sections 1 and 2, the primary initial motivation for the development of the current RotorCRAFT analysis was to capture experimental results on the unsteady loading on rotor blades, particularly those that influence vibratory loading. In pursuit of this objective, though, it must be kept in mind that the various frequency components of rotor loading are closely coupled, and that there is strong interaction between the relatively high-frequency components of loading that govern vibratory excitation and the low-frequency components that establish blade trim and the operating conditions of the rotor. These two problems cannot be easily decoupled and so it was judged essential to first address the ability of RotorCRAFT to predict the steady and low-frequency loads that establish rotor trim. Indeed, as the extensive discussion by Harris in Reference 18 makes clear, even the computation of these quantities is not yet on a satisfactory basis for day-to-day calculations in the rotorcraft industry.

After carrying out correlations focusing on steady and low-frequency loading, several correlation exercises pertaining to unsteady loads will be described. These will include cases in a wide variety of flight conditions and will examine rotor loading at several representative points on the rotor blades in each configuration. These sample calculations will provide examples of the wide applicability of the code, but will also note some of the limitations inherent in both the analysis and the experimental data .

In his review of aerodynamic loads data, Hooper (Ref. 6) noted the relative paucity of complete and reliable airloads data on modern rotor configurations. The shortcomings of existing rotor data sets are also discussed by Johnson in Reference 8. A wide variety of problems with existing data are cited by these reviewers, including sparseness of pressure transducers for the chordwise integration of loads, incomplete coverage of radial stations, and excessive levels of unsteadiness and noise, as well as the presence of poorly documented problems with individual experiments. In spite of these reservations, several data sets do exist in the public domain that are adequate for illustrating the major features of the performance of the RotorCRAFT analysis. Those limitations in the data that may affect the conclusions drawn from the correlation will be noted in each case.

Finally, special attention will be paid to a few particular cases of theory/experiment correlation that illustrate the advantages associated with the implementation of full-span rotor wake modeling. This will have largely to do with the features of rotor loading that are captured with this wake model that are absent from more simplified treatments.

7.2 Performance and Trim Calculations

A logical first step in the study of rotor load correlation is the comparison of measurements and predictions of integrated rotor loading. A candidate data set for such a comparison is the record of wind tunnel tests described Reference 43. These tests involved full-scale experiments on both articulated and teetering rotors and measured integrated forces and moments for a wide range of shaft angle of attack at advance ratios 0.3 , 0.4 , and 0.46 . The comparisons shown here will deal only with the four-bladed, articulated rotors within this data set and will cover the following cases and flight conditions: rotors with -8° and 0° linear twist, operating at advance ratio 0.3 and 0.4 and at shaft angle of attack -5°, 0°, and +5°. The rotor configuration and planform for the -8° case is that of the H-34 main rotor, and the 0° twist rotor was apparently identical except for the lack of

twist. The planform properties are given in Table 7-1; the structural properties of the blade were not specifically stated there but were assumed to be the same as those given for the H-34 rotor blade in Reference 44.

The test results in Reference 43 presented integrated rotor lift and propulsive force coefficients normalized by solidity, as well as integrated pitching moment, rolling moment, and torque. The shaft axis T , H , and Y forces in the RotorCRAFT output were resolved into the wind axis system for comparison to these results. Calculations for a range of collective pitch inputs (all trimmed to zero first harmonic flapping, as was stipulated in Reference 43) were carried out and the comparison to experimental results are shown below.

The configuration selected for the model was kept relatively simple for these calculations. The vortex lattice used on the blades consisted of thirty quadrilaterals spanwise and a single quad chordwise. The default settings for the core size were selected and no adjustment was made during the course of these calculations. The wake structure featured a maximum of 16 filaments trailing from Zone 1 and a maximum of six from the tip filament region, Zone 2. One turn of full-span free wake was used along with one turn of the free wake extensions. Additional far wake was added during numerical experiments, but the change in rotor loading due to the addition of rotor wake beyond two turns was negligible for the cases examined. NACA 0012 airfoil section data was available in C81 format for use in providing drag characteristics. The structural and dynamic parameters of the blade were input to allow the code to compute the blade's mode shapes and natural frequencies. The dynamic model of the blade called for three out-of-plane modes (rigid flapping, plus two elastic bending modes). The computation used twenty four time steps per revolution and most of the cases discussed below were found to converge well within three rotor revolutions.

Figure 7-1 shows the correlation of rotor lift and torque for the case of advance ratio 0.3 , blade twist of -8°, and shaft angles of -5° , 0° , and +5°; the plot shows the predicted curve as well as the experimentally measured points. The correlation is close over the range of collective pitch settings examined, though the predictions have a tendency to overpredict torque over most of this range. The rise in power required that accompanies stall appears to be captured, though the power rise begins slightly earlier than the data suggests that it should. The fact that the difference between predictions and experiment is reasonably consistent across the span for all lift coefficients suggests that profile power may be overestimated. One possible source for such an overestimation is the absence of tip relief in the drag calculation. At present, there is no allowance for a reduction in the effective Mach number in the tip region. Limited numerical experiments with this issue have indicated that reasonable approximations to tip effects provide an effect of the right sign to account for overprediction of torque though the magnitude may be too small. Also, since the largest errors appear around the onset of stall, it may be that the current approach to modeling the aerodynamic loads in the presence of blade stall may be inadequate. The discussion in the summary below will briefly describe work that is underway to improve the stall model. In addition, the sectional drag data from the airfoil tables may be in error.

Figure 7-2 shows similar results for the case of the rotor with untwisted blades, again at advance ratio 0.3. Largely the same results are observed: a close tracking of the predicted power coefficient with some small overprediction across the full range of the data observed, except for a tendency to underprediction at high thrust levels. Figures 7-3 and 7-4 show more restricted comparisons of the predicted and measured power over the thrust range of interest at advance ratio 0.4 ; the figures show results for the twisted and

TABLE 7-1

SPECIFICATIONS OF THE H-34 MAIN ROTOR

Number of Blades	4
Radius	28.0 ft
Chord	1.366 ft (constant)
Solidity	.0622
Root Cutout	16% of radius
Flap Hinge Location	3.7% of radius
Twist	-8° (Linear)
Airfoil	NACA 0012
Rotor Angular Velocity	Variable in flight tests 23.2 rad/sec in wind tunnel tests

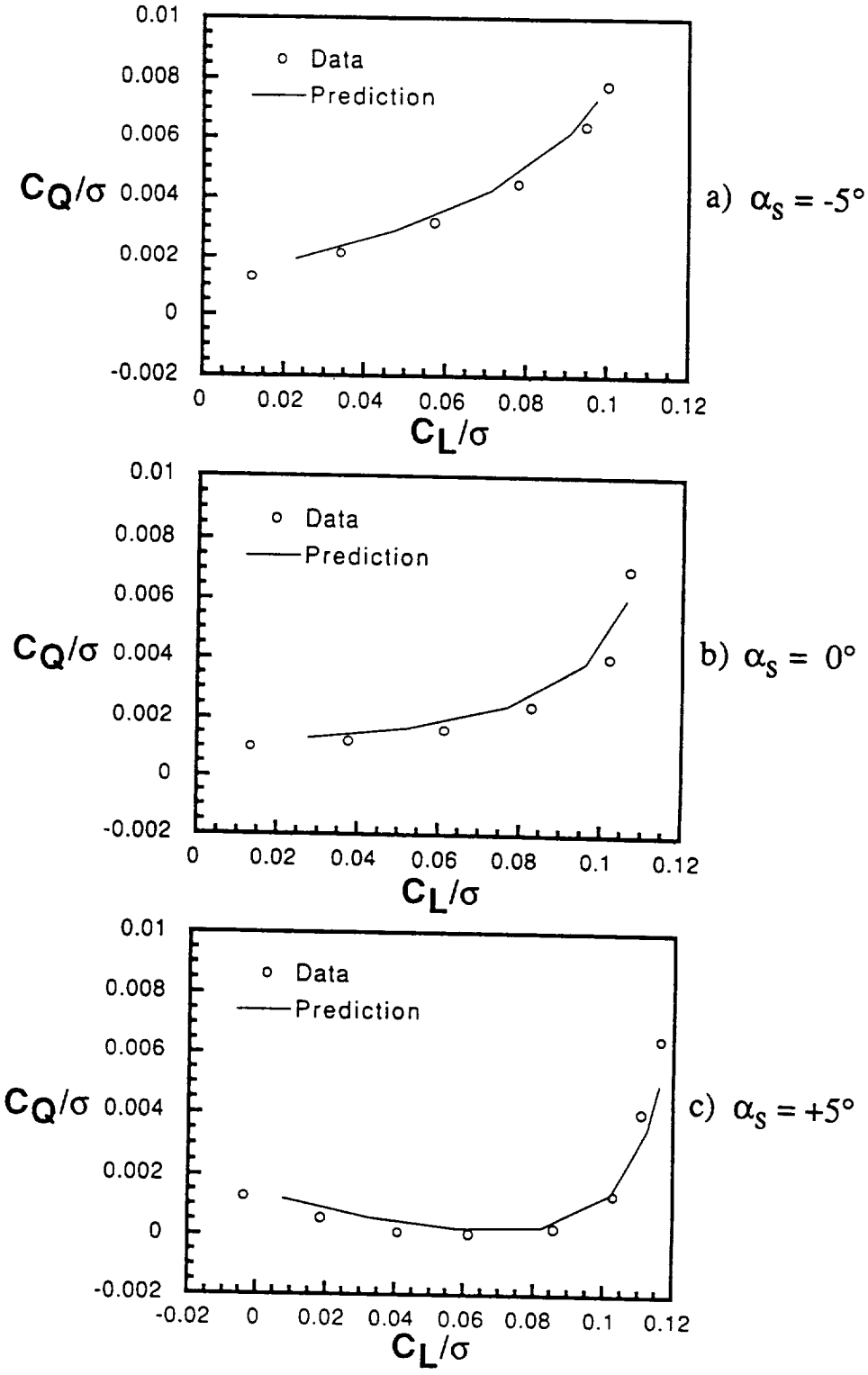

Figure 7-1. Predicted and measured performance for a four-bladed rotor with -8 deg. linear twist at advance ratio 0.3 .

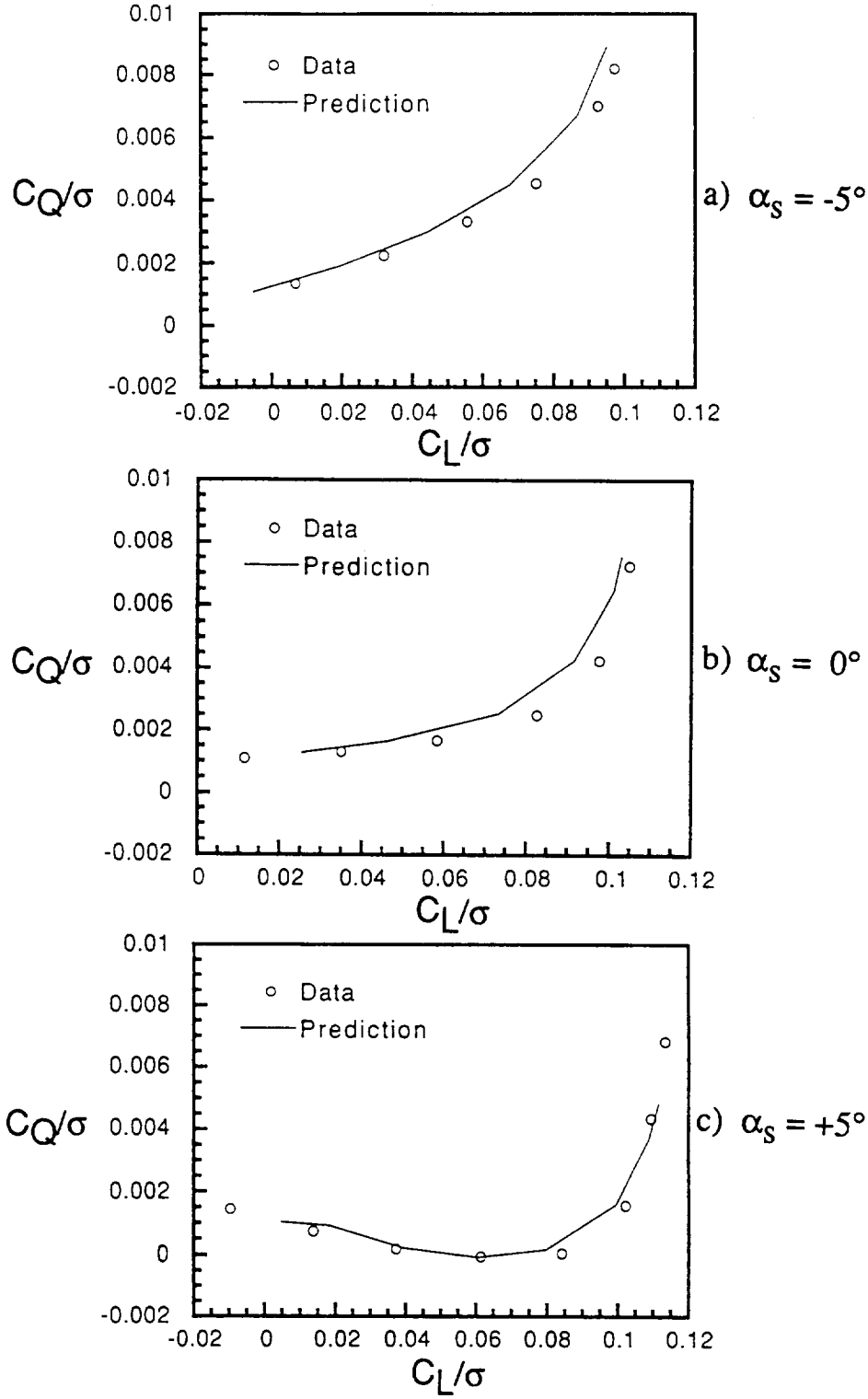

Figure 7-2. Predicted and measured performance for a four-bladed rotor with untwisted blades at advance ratio 0.3 .

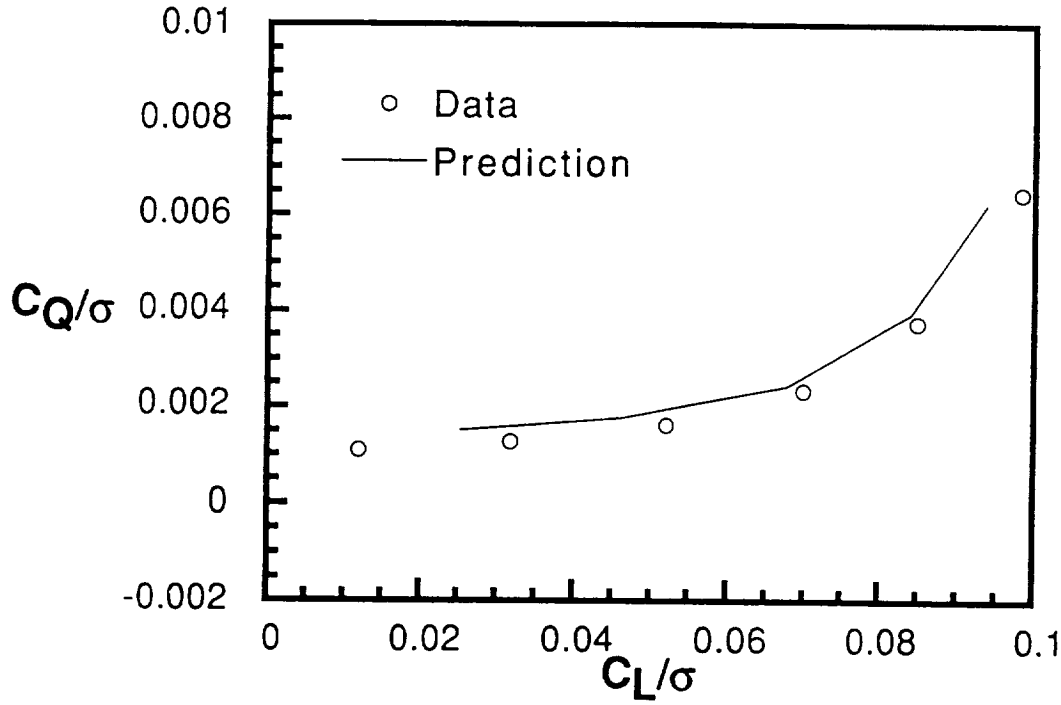

Figure 7-3. Predicted and measured performance for a four-bladed rotor with -8° linear twist at advance ratio 0.4 and 0° shaft angle of attack.

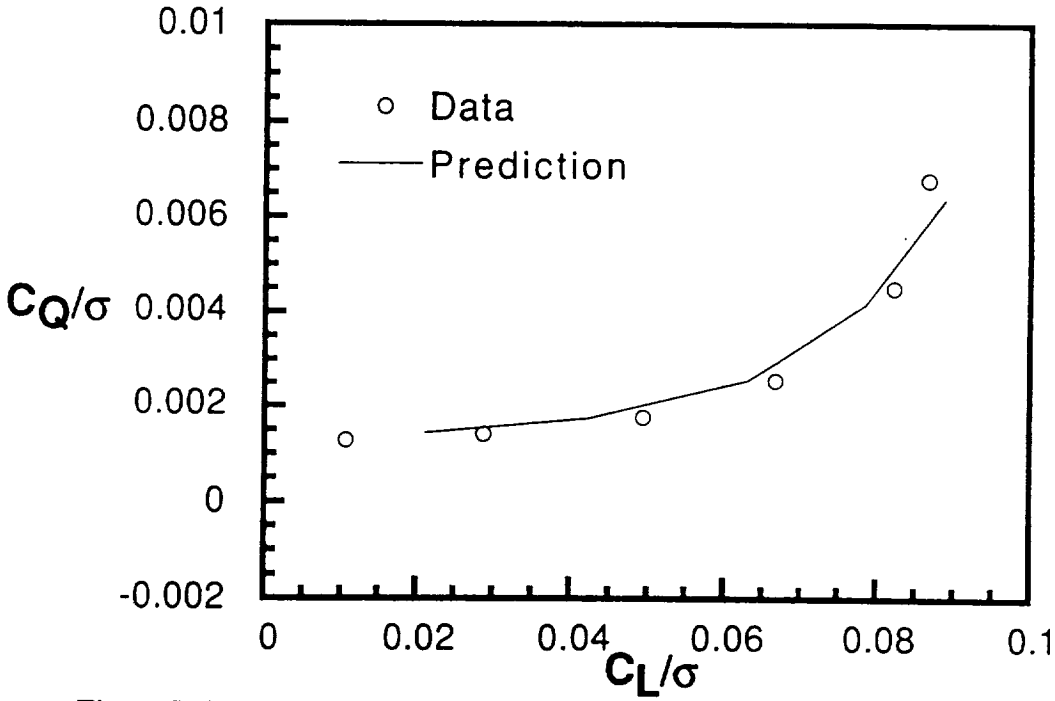

Figure 7-4. Predicted and measured performance for a four-bladed rotor with untwisted blades at advance ratio 0.4 and 0° shaft angle of attack.

untwisted blade, respectively, for the case of $\alpha_s = 0^\circ$. These comparisons show much the same trends as the results of the calculations at advance ratio 0.3.

Along with integrated performance, the prediction of rotor blade motion is important to the understanding of rotor trim. The prediction of the blade's flapping motion is in general a more sensitive calculation than the computation of integrated loading. This is particularly true at low forward speeds, where the calculation of the effects of the distorted rotor wake and its interaction with the blades has a strong influence on the blade motion. This sensitivity was well documented in an experimental study using a model rotor (Ref. 45). This test used a model rotor whose specifications are summarized in Table 7-2. The test was carried out in the Boeing Helicopters V/STOL wind tunnel using a four-bladed model rotor; the forces and moments on the rotor as well as the blade's coning and flapping motion were recorded for a series of runs from advance ratio 0.0 to 0.24. The runs to be discussed here were carried out at essentially a constant thrust level of C_T/σ of 0.08, with the shaft angle varied to keep α_{TPP} at approximately 1.0°.

The test was carried out on a balance simulating the rear pylon of a tandem helicopter, so the results may well contain body interference effects. The discussion in Reference 45 does not elaborate on this possibility, though several data points described as being taken in a "previous isolated rotor test " are presented. In addition, the measured lateral flapping presented in a nominal hover condition of advance ratio 0.0 was 0.34°, suggesting some type of interference effect. Finally, the discussion in Reference 45 quotes a measurement accuracy of 0.25° on the flapping angles presented. Even though there are substantial experimental uncertainties associated with this data, the qualitative results of this experiment and their importance to the issues of low speed trim are not in doubt, as is discussed at length in Reference 11.

Several computational efforts (including Refs. 11 and 46) have focused on recovering the flapping behavior measured in this test. Previous work in Reference 46 showed the sensitivity of the predicted flapping to the choice of tip vortex core size with a single-tip-vortex wake model. As discussed in Section 3.2.4, one objective of the present effort was to reduce the role of vortex core size as a modelling parameter. The calculations presented here for low speed trim all use the default core selection procedure described earlier, namely that the core size of each filament adjusts according to the spacing of the filament release points. For these particular calculations, a "floor" or minimum allowable core size of .02R was selected for all filaments.

For these calculations, a vortex lattice with 30 quadrilaterals spanwise and one chordwise was used. The blade dynamics model used a three-mode approximation, with the rigid flapping, first elastic bending, and first elastic torsion mode included. The wake model featured one turn of full span free wake, three turns of free wake extensions, and included the far wake summation described in Section 3. The full-span wake model used a maximum of 12 filaments in Zone 1 and two filaments in Zone 2 (the appearance of negative tip loading was not anticipated in these calculations and was not, in fact, observed).

Figure 7-5 shows the measured and computed lateral flapping angles for a series of cases from advance ratio 0.06 to 0.24. Error bars corresponding to the nominal 0.25° experimental uncertainty in angle measurement are used with the data points. As is evident, the computations fall well within the error bars for the whole range of the test. The peak lateral flap amplitude was observed at advance ratio 0.08, as in the experiment, but the trend to reduced flapping at lower speeds could not be reproduced because of poorly

TABLE 7-2

SPECIFICATIONS OF FLAPPING TEST MODEL ROTOR

Number of Blades	4
Radius	2.73 ft
Chord	0.19 ft
Solidity	.0892
Root Cutout	19.2% of radius
Flap Hinge Location	2.3 % of radius
Twist	-9.14° (Linear)
Airfoil	23010-1.58
Rotor Angular Velocity	164.8 rad/sec

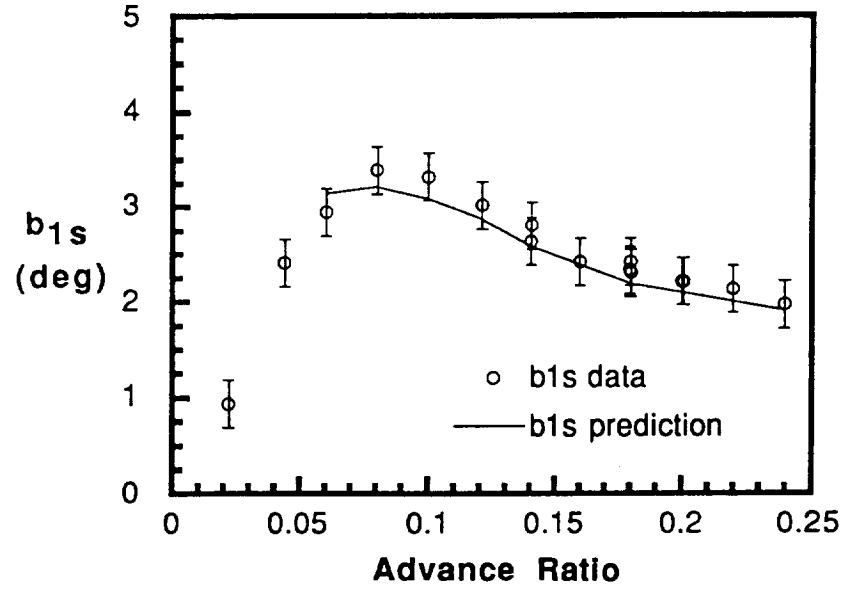

Figure 7-5. Predicted and measured lateral flap angle vs. advance ratio for a four-bladed model rotor at $C_T = .0071$.

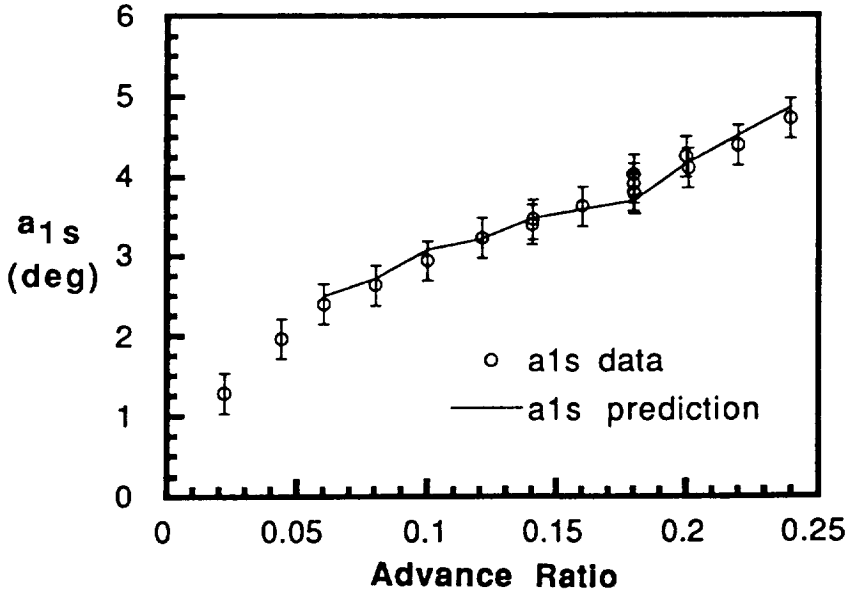

Figure 7-6. Predicted and measured longitudinal flap angle vs. advance ratio for a four-bladed model rotor at $C_T = .0071$.

C-2

converged time-marching solutions. The lowest speed for which a meaningful answer for blade motion could be obtained was advance ratio 0.06 ; this case required nine rotor revolutions to converge, while eight were used for advance ratio 0.08 to 0.12 and five for all cases with higher advance ratio. The poor convergence properties of low advance ratio cases was anticipated and is discussed in Reference 11. With a Lagrangian wake model such difficulties are inevitable at low speed, though new methods like that documented in Reference 47 may ultimately offer a way to circumvent them.

Figure 7-6 shows the results for predicted and measured longitudinal flap angle, and again the predictions fall within the nominal error bars. The good correlation achieved with both lateral and longitudinal flapping at low speed, along with the results presented on integrated performance above, indicate that the full-span wake model captures many of the important features of the wake-induced flow field for both high and low speed flight.

7.3 H-34 Flight Test

Reference 48 contains tabulated measurements of aerodynamic loading on an H-34 main rotor in flight tests in a wide variety of flight conditions. For purposes of the present correlation study, two of these cases were selected. The first was a low forward speed case with advance ratio 0.13 and shaft angle of attack -0.7° (Flight 6 of the cases considered in Ref. 48). The second case was at a relatively high advance ratio of 0.29 at a shaft angle of attack of -6.9° (Flight 19 in Ref. 48).

The physical description of the rotor blades used here is almost identical to that given in Table 7-1. Here, the blades were equipped with a trailing edge tab that was deflected 4° upward between r/R = 0.85 and 0.9 . (The effect of this tab is neglected in the calculations that follow). The experimental installation for these tests featured pressure transducers placed chordwise along the blade at five to eleven radial stations from 0.25R to 0.95R . The time-varying lift force was integrated at each of these stations, and the resulting sectional loads are presented in tabular form in Reference 48, along with harmonic analysis of these loads and of the pitch and flap motion of the rotor blade.

The calculations carried out for each of these cases trimmed the rotor using the information on gross weight, air density, and tip speed given in Reference 48. The H-34 used in these tests had a variable RPM rotor, so the tip speed in general changed with each flight condition. The tip speed varied for most of the experiments; for the 0.13 case the tip speed was 648 fps, while for the 0.29 case it was 690 fps. The thrust coefficient for the 0.13 case was 0.0047 , and for the 0.29 case it was 0.0056 . In each of the calculations, the rotor was trimmed to zero first harmonic flapping to simulate the zero hub moment condition of an aircraft in free flight. Reference 48 notes that the pressure transducers on the blade were subject to a 4.5° phase lag; the results below have been phase-shifted to eliminate this effect.

The computations were carried out with a model configuration identical to that employed for the full-scale H-34 rotor discussed in the previous section. A 30x1 grid of vortex quadrilaterals was used on the blade and a four-mode dynamic model, consisting of rigid flapping, the first two elastic bending modes of the blade, and the first elastic torsion mode. Both cases used 24 time steps per revolution, though the wake model differed substantially for the two cases. For the low speed case, a wake with twelve filaments in Zone 1 and two in Zone 2 was used in the full-span wake region, which covered one turn of wake. After this point, two turns of two-filament free wake extension were employed, followed by two prescribed turns in the intermediate wake and finally the analytical summation of the far wake influence. In the high speed case, on the other hand, only two

turns of wake were used: one turn of full-span free wake using 16 filaments in Zone 1 and six in Zone 2, and a second turn of two-filament free wake extension. It was observed that five rotor revolutions were required to converge the solution at advance ratio 0.13 , while three sufficed in the 0.29 case because of the convection dominance of the free stream. Default core sizes were used in all cases.

In each case, airloads were computed at four radial stations: r/R = 0.75 , 0.85 , 0.9 , and 0.95 . The results for the 0.13 case are shown in Figure 7-7. Both the data and the calculation display the 'peaky' loads in the first and fourth quadrants characteristic of wake interactions with the rotor in low speed flight. For this case, the correlation for radial stations 0.75 , 0.85 , and 0.9 is quite close, indicating that the wake-induced effects in low speed are being captured well. At r/R = 0.95 , however, substantial underprediction of loads occurs on the retreating side. The cause of this is unclear, though the neglect of the moments caused by the trailing edge tab may be one reason. A trailing edge tab deflected upwards would lead to a nose-up pitching moment that could contribute to an increase in sectional loading near the tip.

The results for the advance ratio 0.29 case are shown in Figure 7-8, and they exhibit consistently good correlation with the measured loads. However, the loads experienced in this particular flight condition have less of the high-frequency loading than the wind tunnel tests of an isolated rotor discussed in Reference 44, as will be discussed below.

7.4 SA-349 Flight Test

The source for the data used in these comparisons is Reference 49, which documents flight tests undertaken in 1986 featuring an SA-349. This helicopter has a three bladed rotor with blades of radius 17.2 ft. and chord 1.15 ft. Each blade has five degrees of washout between the blade cutout and the 92.5% radial station, with an untwisted planform outboard of that point. The flight tests covered a wide range of operating conditions from advance ratios 0.14 up to 0.38 and included cases in turning flight. The level flight case presented here pertains to a rotor at advance ratio 0.14 and a thrust coefficient of 0.00427.

The blades were instrumented with pressure transducers at three radial stations (r/R = 0.75 , 0.88 , and 0.97) to provide chordwise load distributions, and these pressure distributions were integrated to produce the sectional normal force. Reference 49 provides filtered frequency spectra of both the normal force and the pitching moment at each of the stations, drawn from time histories averaged over six rotor revolutions. As discussed by Johnson in Reference 8, the data is subject to considerable unsteadiness and noise, and so the repeatability of particular details of the rotor load time history is uncertain. In these cases, the primary focus of the correlation study should be on capturing the major features of the loading as closely as possible.

The structural properties of the SA349 rotor blade were taken from the appendices of Reference 49, and they were used in the computation of the modal properties of the blades. In each of the calculations below, three bending modes (rigid flapping and the first two elastic bending modes) as well as the first elastic torsion mode were retained. Default core size selection was again invoked.

The case considered was Test 2 of Reference 49 (advance ratio 0.14, $C_T/\sigma = .067$). These calculations were run with one turn of full-span free wake and two turns of free

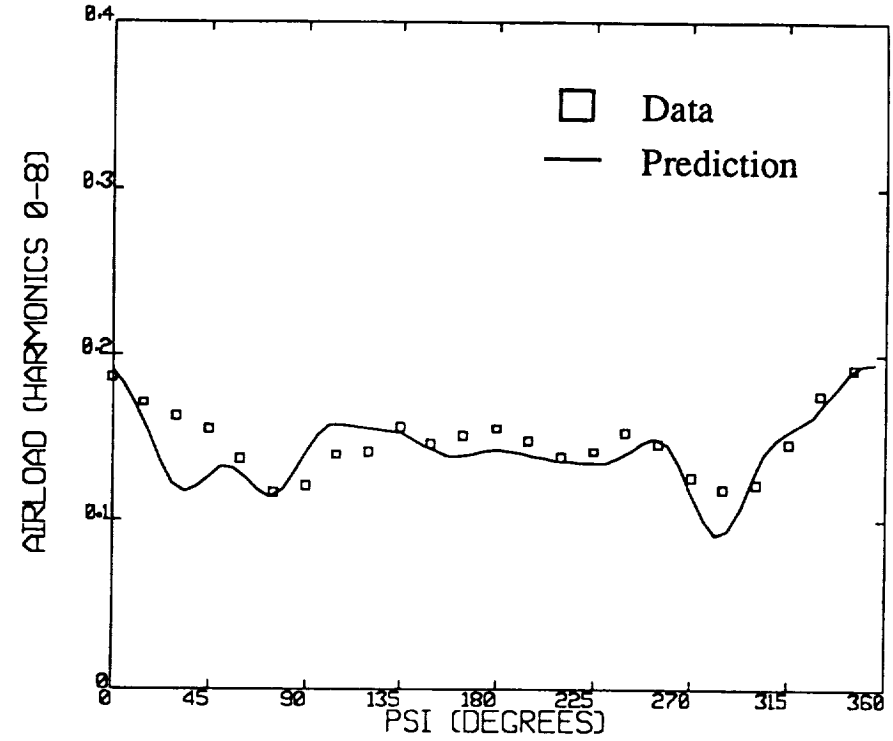

a) r/R = 0.75

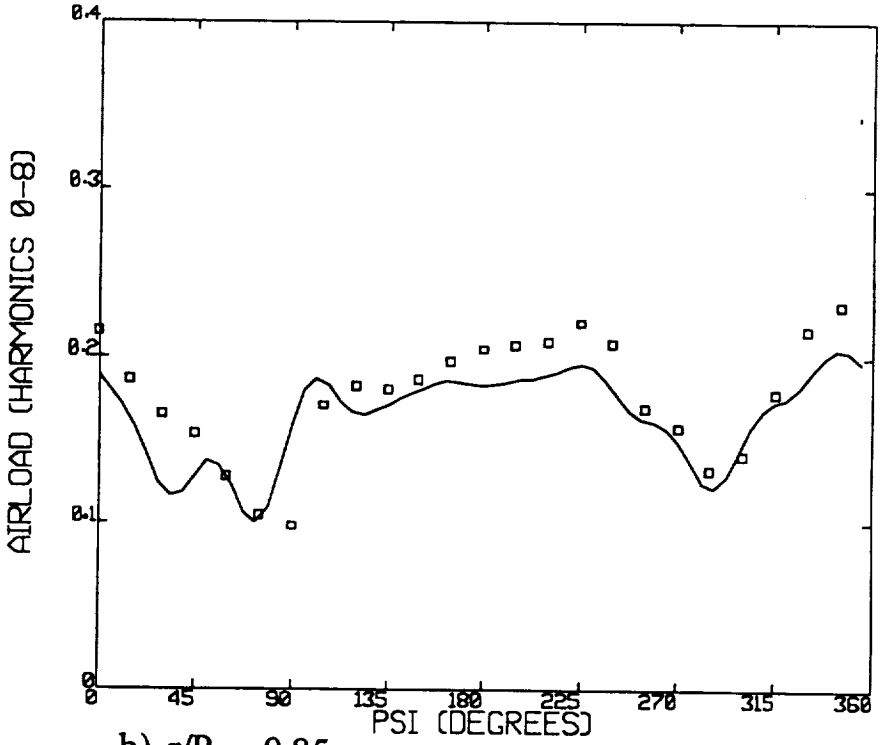

b) r/R = 0.85

Figure 7-7. H-34 flight test plot of nondimensional airload vs. azimuth, advance ratio 0.13 .

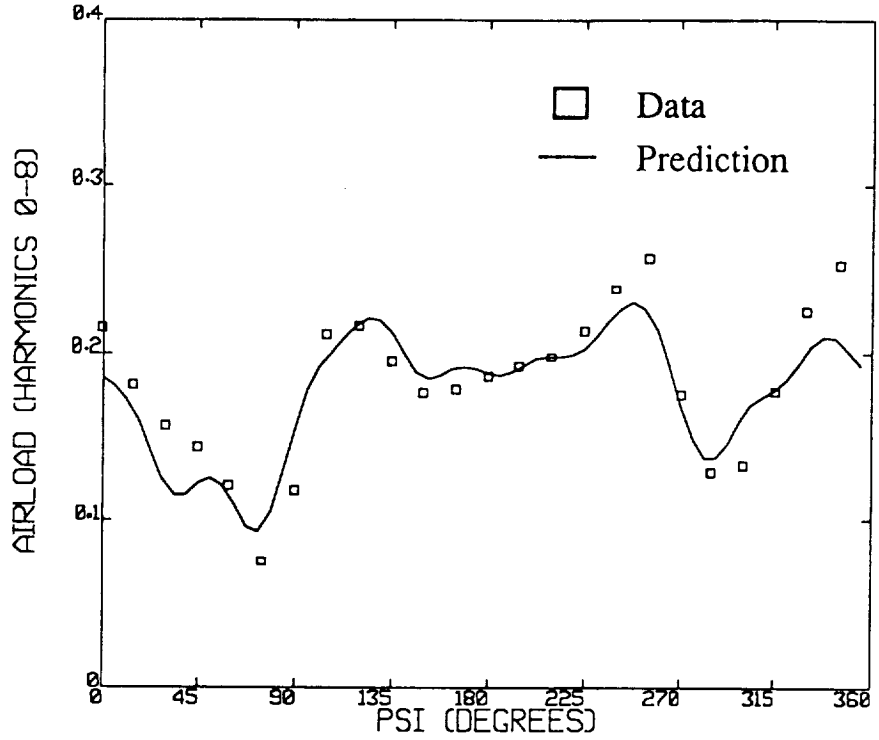

c) r/R = 0.9

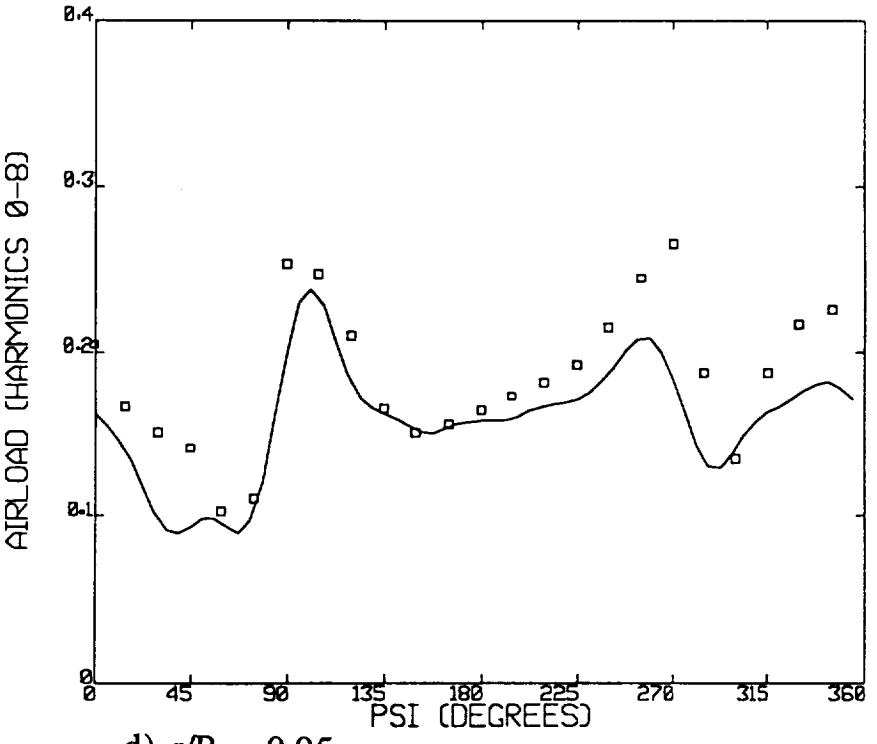

d) r/R = 0.95

Figure 7-7 (Cont'd). H-34 flight test plot of nondimensional airload vs. azimuth, advance ratio 0.13 .

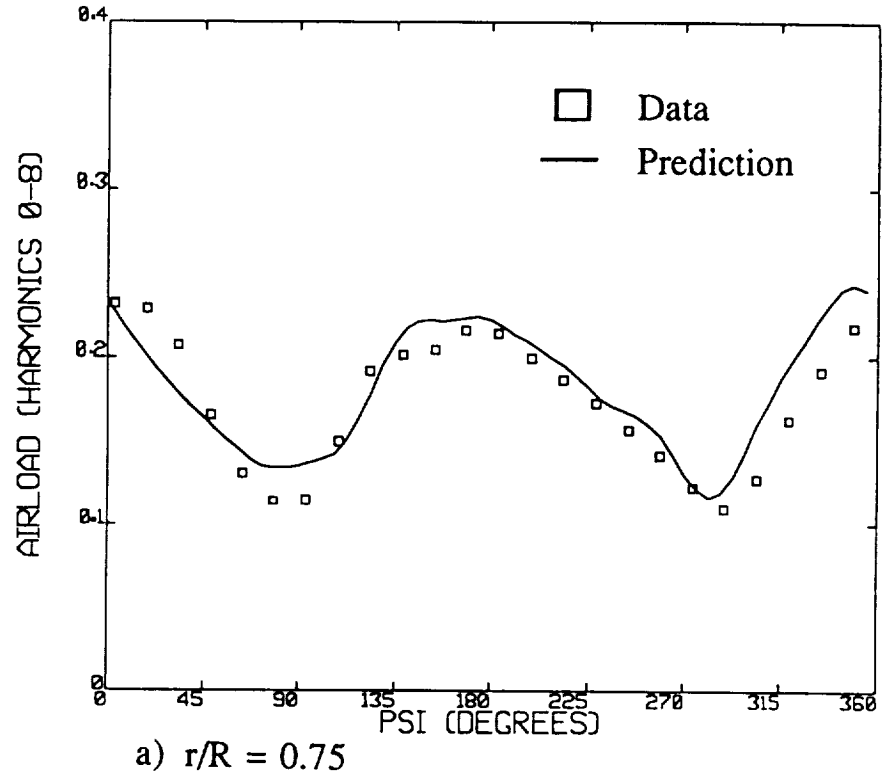

a) r/R = 0.75

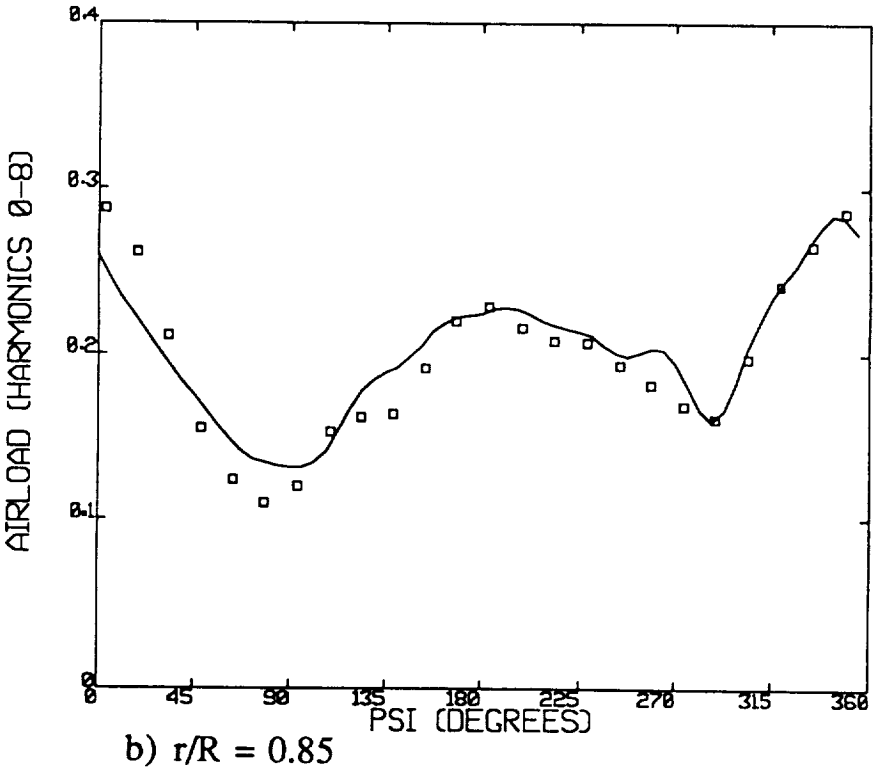

b) r/R = 0.85

Figure 7-8. H-34 flight test plot of nondimensional airload vs. azimuth, advance ratio 0.29 .

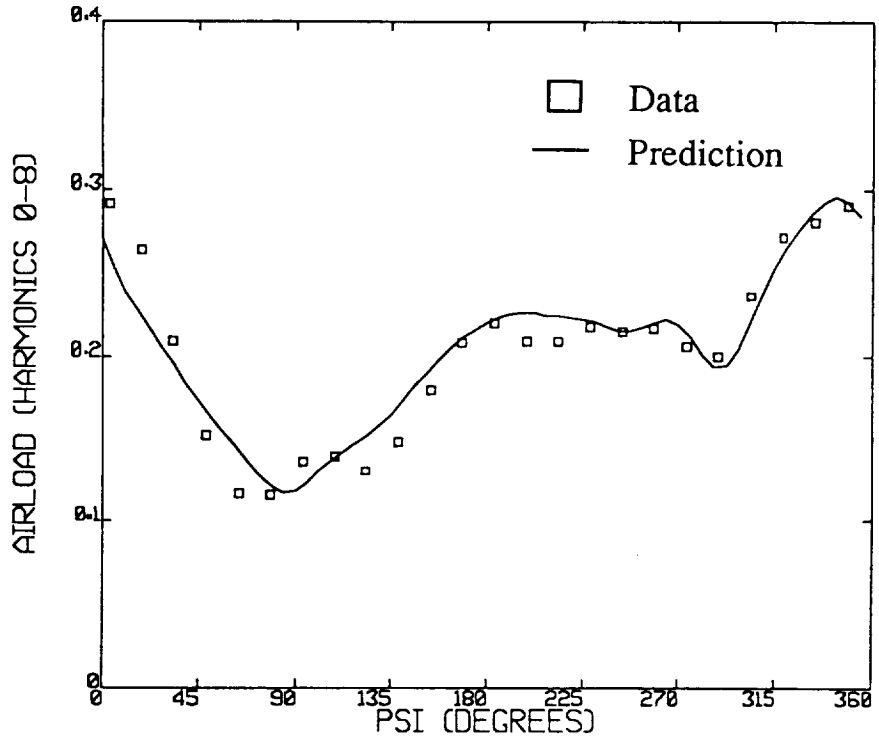

c) r/R = 0.9

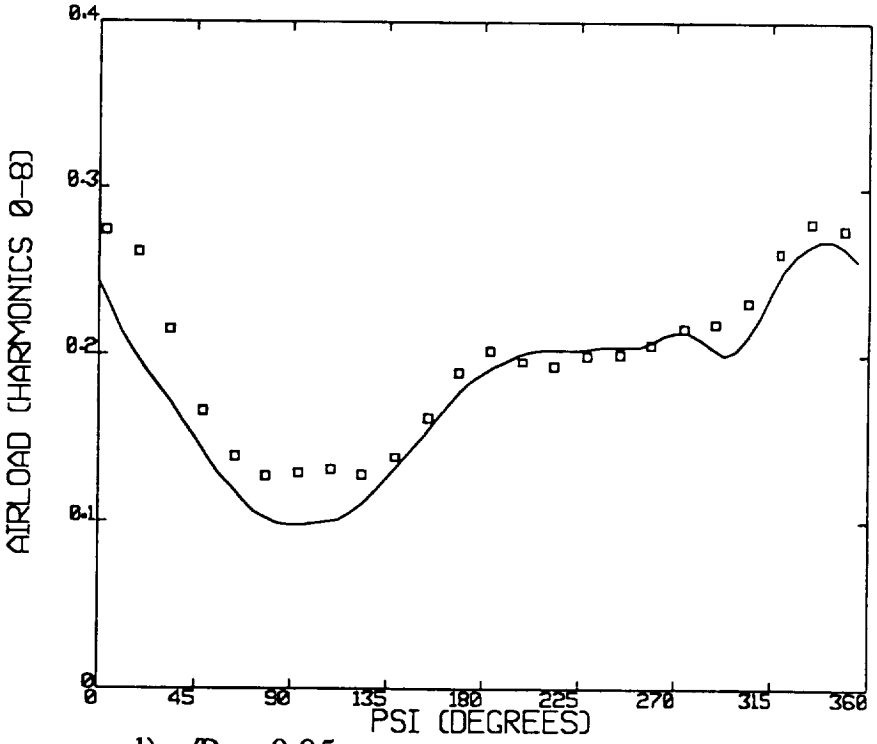

d) r/R = 0.95

Figure 7-8 (Cont'd). H-34 flight test plot of nondimensional airload vs. azimuth, advance ratio 0.29 .

wake extensions; two turns of prescribed wake were also used, and the far field wake summation was invoked. The blade loading solutions were found to be adequately converged after five rotor revolutions.

Figure 7-9 shows the predicted and measured time histories of nondimensional airload for this case. As is evident, the agreement is good for nearly all azimuthal locations, r/R=0.75 and r/R=0.97 . The correlation at r/R=0.88 is worse in certain particulars, notably in overpredicting the loads in the vicinity of the 180° azimuthal station. It is noteworthy that Johnson in Reference 8 shows a similar overprediction in this region. This may suggest that a problem exists with the data, or that there is a shared flaw in the analysis of Reference 8 and the current version of RotorCRAFT.

7.5 H-34 Wind Tunnel Test

In Reference 6, Hooper discussed the measured airloads from a wind tunnel test of a full-scale H-34 main rotor (Ref. 44). This data set represents one of the few relatively complete data sets that are available for correlation studies in the technical literature. As Hooper notes, the airload data clearly exhibits some of the dominant mechanisms that lead to large vibratory airloads in high-speed forward flight and thus is a very useful point of reference for correlation efforts. However, the experimental report indicates that the H-34 wind tunnel tests were run with a control system that caused the cyclic pitch of two of the rotor blades to differ from that applied to the other two. This "split tip-path plane" introduces an unwelcome ambiguity into the interpretation of the trim condition for the test.

In addition, examination of the spanwise load distribution in the experimental data reveals an unusual feature in the tip loading. Figure 7-10 shows plots of the nondimensional thrust measured for the H-34 at the following radial stations: 0.25R , 0.4R , 0.55R , 0.75R , 0.85R , 0.9R , and 0.95R . Note the presence of a 'notch' in the loading distribution at the 0.9R station. The presence of this feature is somewhat counterintuitive, since one would typically expect a smoother roll-off in the loading near the tip, particularly for azimuth angles around 0° . This feature may be due to a systematic experimental problem, such as a biased measurement device or poor calibration. It is also possible that it can be attributed to an actual physical phenomenon, such as the irregular tip loading due to side edge separation noted in Reference 50.

The principal physical characteristics of the H-34 blade were given in Table 7-1; the rotor tested here featured -8° of linear twist. The rotor's angular velocity for this test was 23.2 rad/sec , yielding a rotor tip speed of 650 fps , or roughly Mach 0.58 at standard sea-level conditions. This tip speed is relatively low by the standards of modern rotorcraft, but even so is high enough to produce transonic flow on the advancing tip for flight conditions for advance ratios near 0.4 . Appendix B discusses some of the experimental uncertainties that can be introduced due to the presence of shock waves in transonic flow for such cases.

Calculations for the H-34 were undertaken using a blade dynamics model that included three out-of-plane bending modes (rigid flap mode and two elastic bending modes) as well as the first elastic torsion mode. Lag motion was neglected since it was judged unlikely that it would contribute significantly to vibratory airloading in this configuration. In each case, the computations were trimmed to the measured thrust coefficients and first harmonic flapping amplitudes given in the experimental results; in all cases, the nominal thrust coefficient was very nearly 0.0037 . For the computations to be discussed in this section, a vortex lattice grid using three quadrilaterals chordwise and 30 spanwise was used. The default core size option was also invoked, and the calculations were run using the

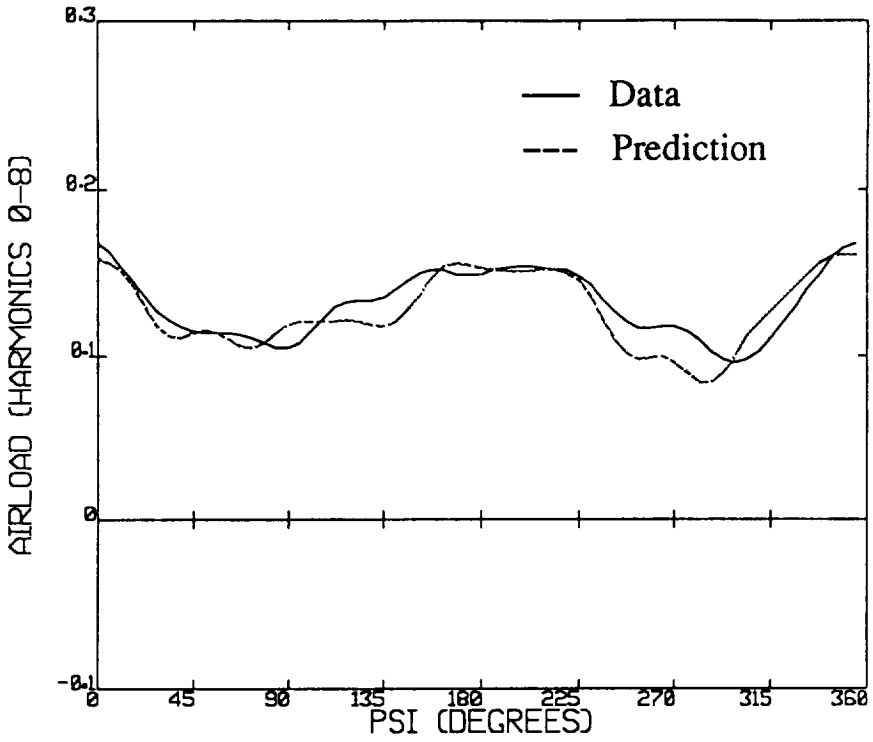

a) r/R = 0.75

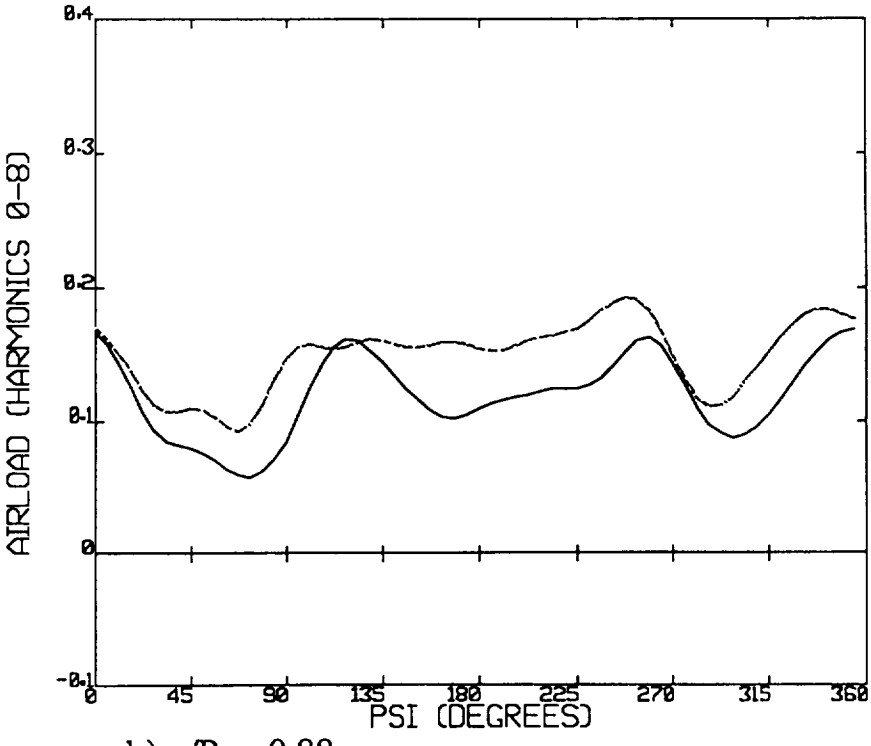

b) r/R = 0.88

Figure 7-9. SA-349 flight test plot of nondimensional airload vs. azimuth, advance ratio 0.14 , C_T = .00427 .

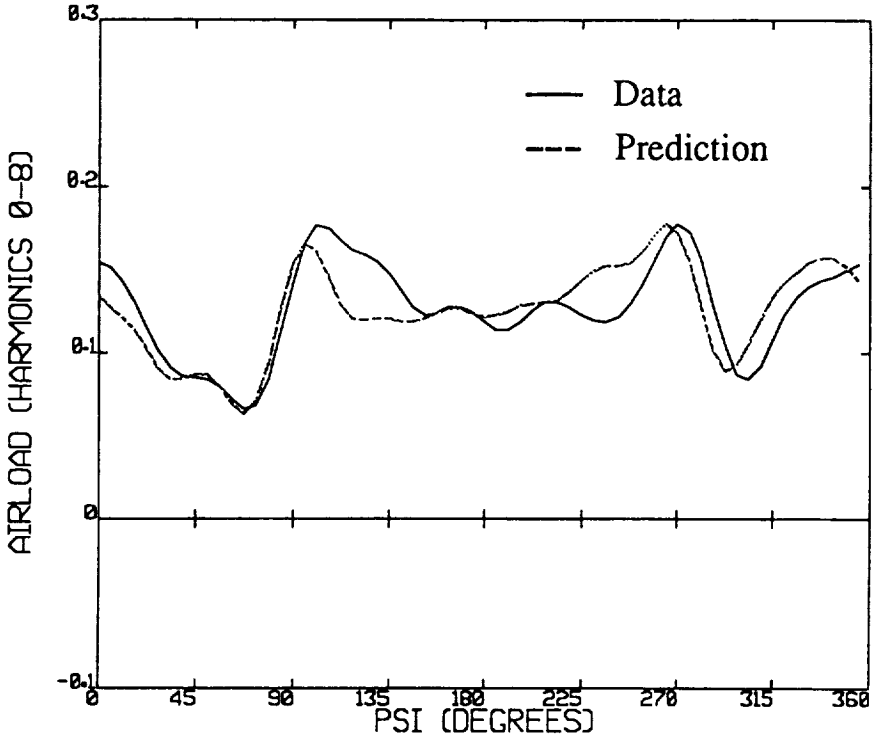

c) r/R = 0.97

Figure 7-9 (Cont'd). SA-349 flight test plot of nondimensional airload vs. azimuth, advance ratio 0.14 , C_T = .00427 .

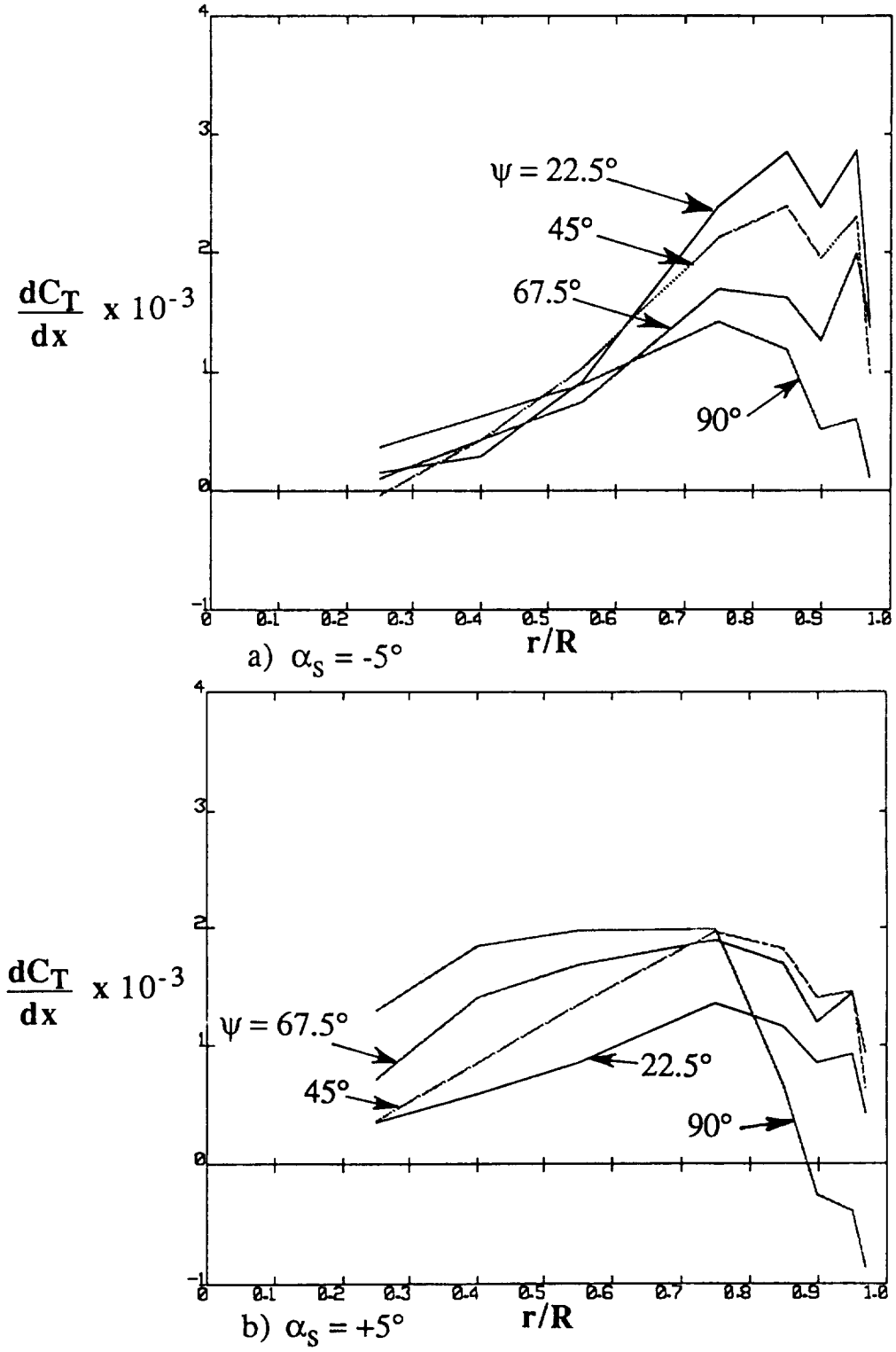

Figure 7-10. Experimental measure of spanwise thrust distribution for the H-34 wind tunnel test: advance ratio 0.39 , thrust coefficient .0037 .

option of looking up two-dimensional moment coefficients rather than computing the results from the vortex lattice solution itself.

The computations to be discussed here focus on three cases at advance ratio 0.39 : shaft angles of attack -5°, +5° , and 0° . After reviewing the results for airload predictions in the first two cases, the results of the 0° case will be examined in detail to explore the role of the full-span wake model in the prediction of vibratory airloading. The 0° case was chosen for particular attention since it involves very close interaction of the rotor wake with following blades, and thus the modeling of the rotor wake plays a particularly important role in these calculations.

All of the calculations shown below were performed using 24 time steps per revolution, though the predictions were Fourier-decomposed and reconstructed using only the first ten harmonics of the rotor rotation frequency. This was done to match the harmonic resolution of the experimental data. Also, the measurements include a five degree phase lag attributable to the pressure measurement system; the plots of the measured data that follow have not been adjusted to allow for this lag.

Figure 7-11 shows the measured and predicted time histories of the nondimensional thrust loading at five radial stations for the -5° case. At r/R = 0.4 and 0.55 , the agreement is very close, with the only significant differences appearing in the vicinity of $\psi = 0°$. The results at r/R = 0.75 show a significant phase error, though the levels are well predicted; part of the phase error can be accounted for from the experimental lag just described, but it does appear that the prediction leads the measurement nonetheless. At r/R = 0.85 , the level is significantly off and a phase error persists, though the level close to the tip (r/R =0.95) is well captured.

Largely similar results appear in Figure 7-12, depicting the correlation at +5 shaft angle of attack. The results at the inboard sections shown in 7-12a and 7-12b are well predicted, though more significant errors appear at r/R = 0.75 . Here, the size of an "up-down" pulse in the vicinity of $\psi = 0°$ is overpredicted and the phasing of the loading on the advancing side is in considerable error. However, both features improve for stations nearer the tip, as shown in Figures 7-12d and 7-12e; the size of the pulse in the $\psi = 0°$ region is closer to experiment and the phasing of the loading becomes considerably closer. Figure 7-13 shows a similar pattern for the loading in the case of 0° shaft angle of attack; close correlation inboard and near the tip, with more significant errors in level and phasing for intermediate stations.

7.6 Contributions of Full-Span Modeling in Airload Calculations

These results indicated that many of the features of the airloading are being captured for the H-34 case. A topic of special interest at this point is the source of the aerodynamic loading that contributes to vibratory loads on the rotor. This section focuses on one particular case and discusses in detail the influence of the current full-span wake model and the vortex lattice blade model on the prediction of the components of the rotor loading that contribute to vibration. The H-34 is a four-bladed rotor, and so the 3P , 4P , and 5P (three-, four-, and five-per-revolution) components of the aerodynamic loading will be the primary contributors to vibratory loads at the rotor hub. The first priority in this discussion is to identify the physical mechanisms leading to such loading.

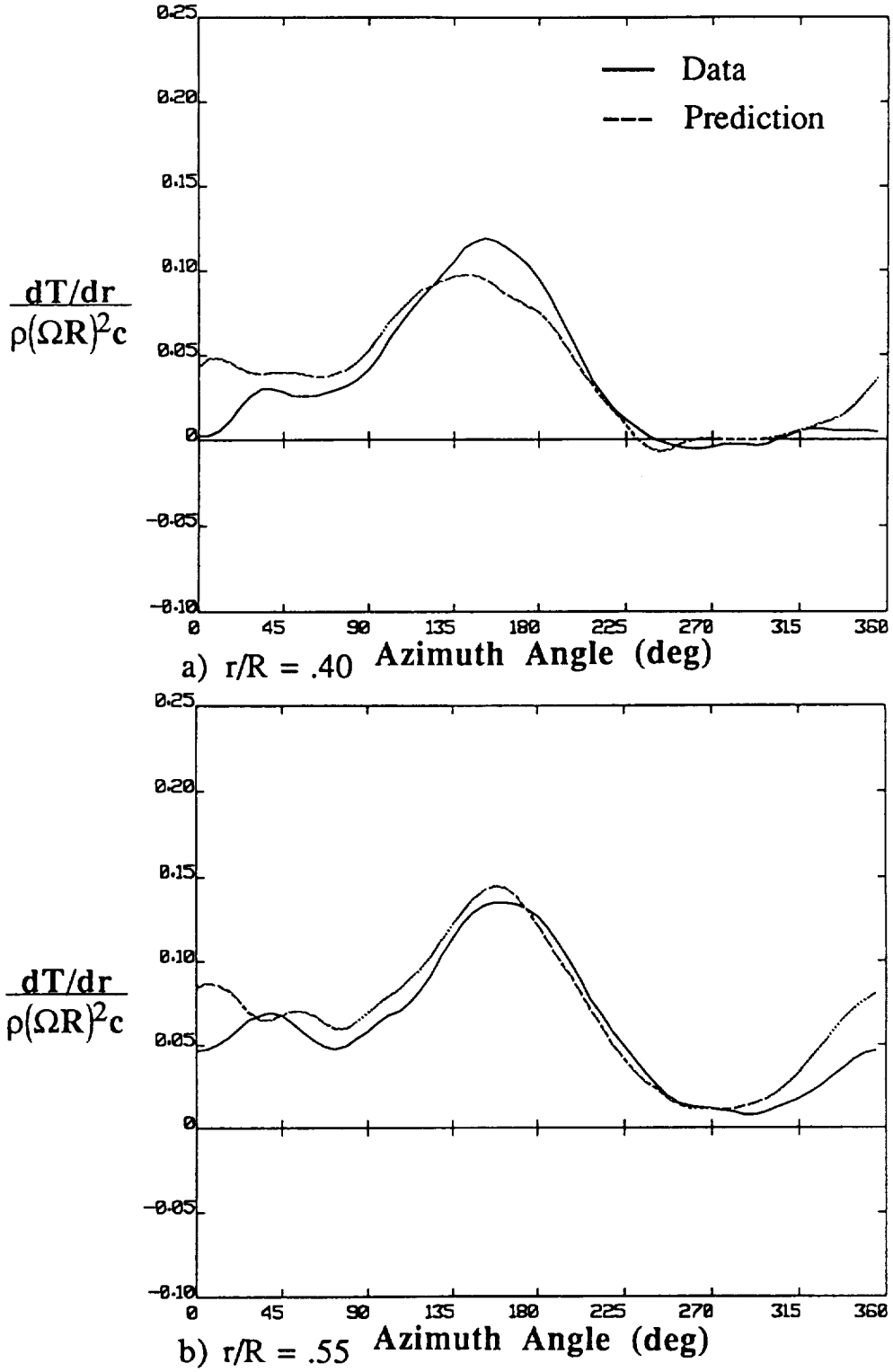

Figure 7-11. Nondimensional sectional thrust vs. azimuth angle for the H-34 rotor: advance ratio 0.39 , -5° shaft angle of attack.

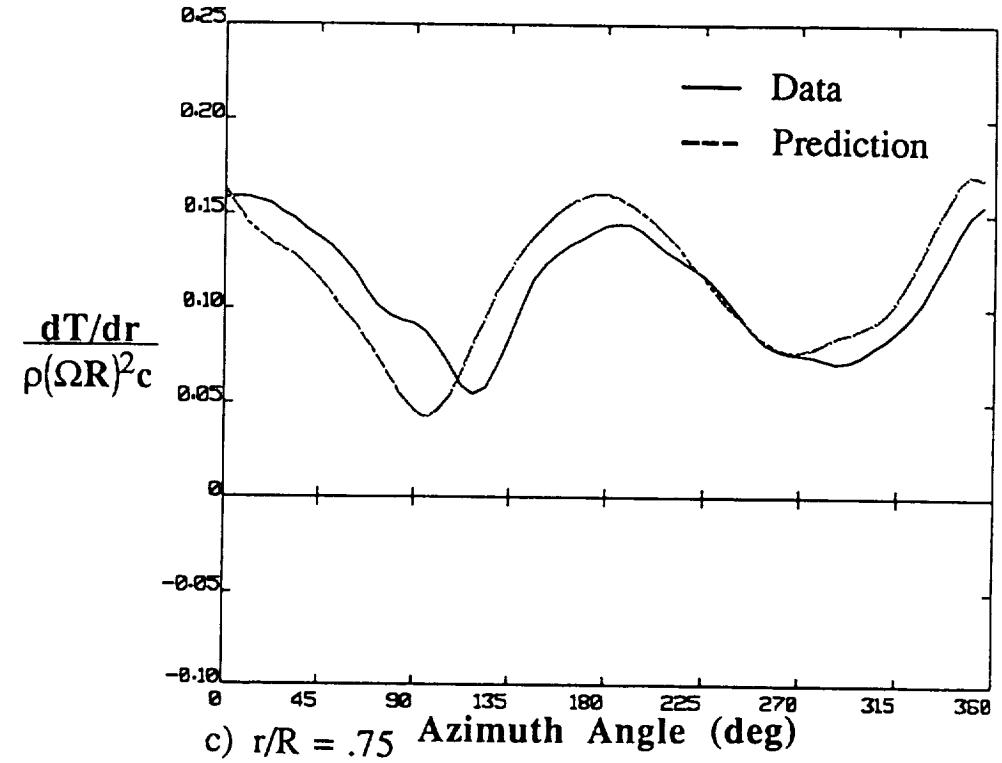

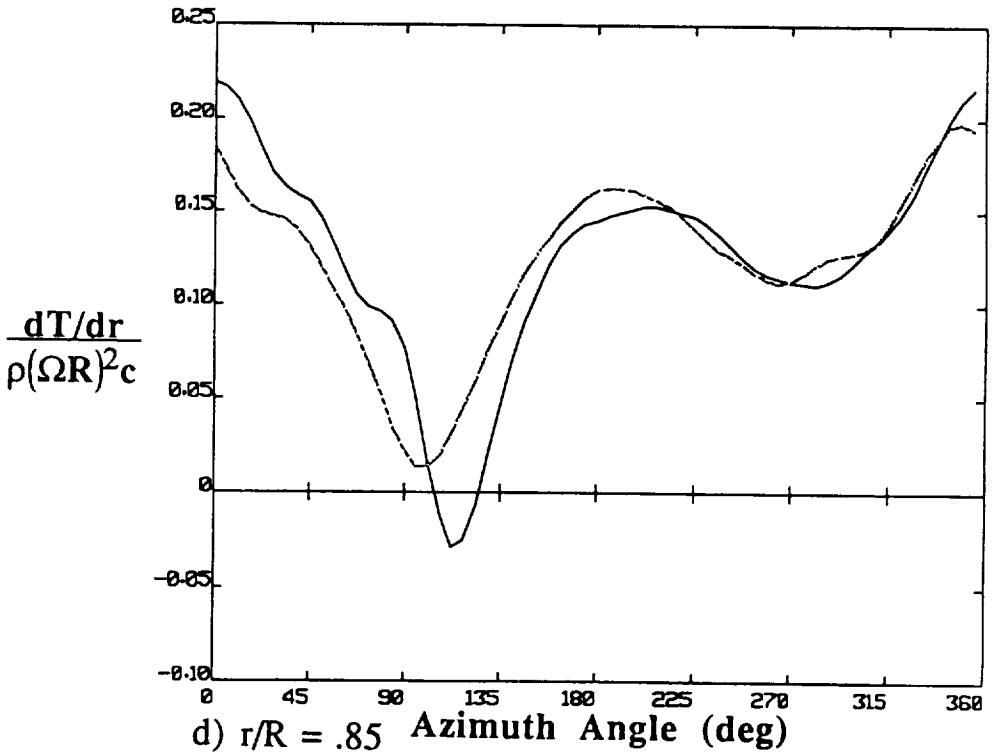

Figure 7-11 (Cont'd). Nondimensional sectional thrust vs. azimuth angle for the H-34 rotor: advance ratio 0.39 , -5° shaft angle of attack.

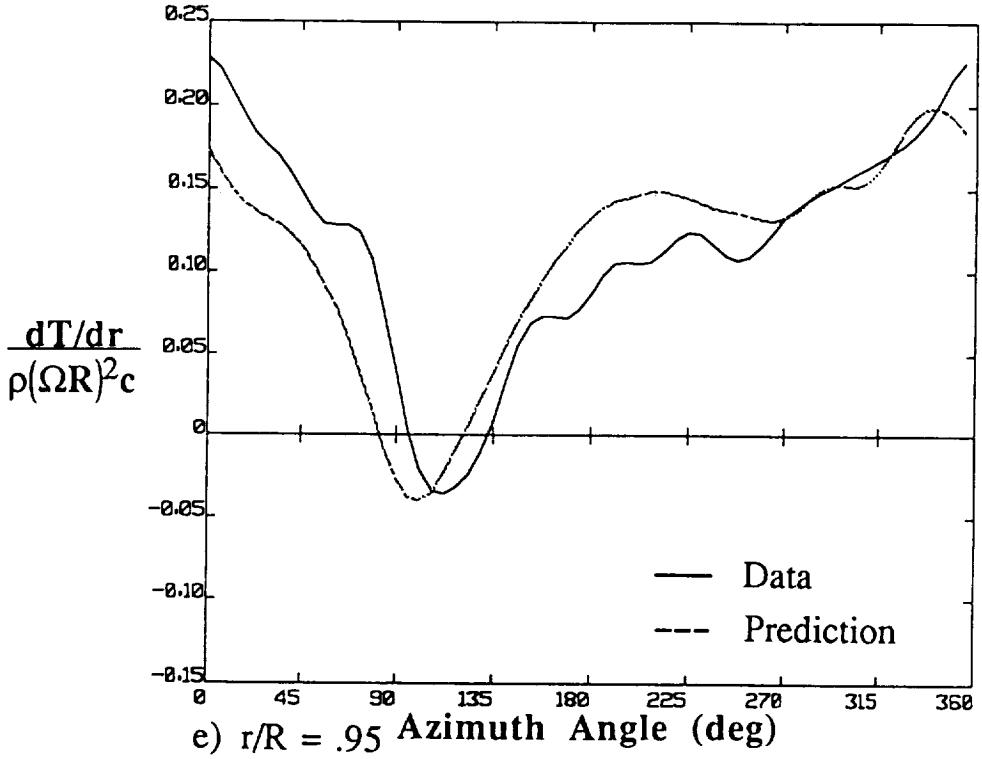

Figure 7-11 (Cont'd). Nondimensional sectional thrust vs. azimuth angle for the H-34 rotor: advance ratio 0.39 , -5° shaft angle of attack.

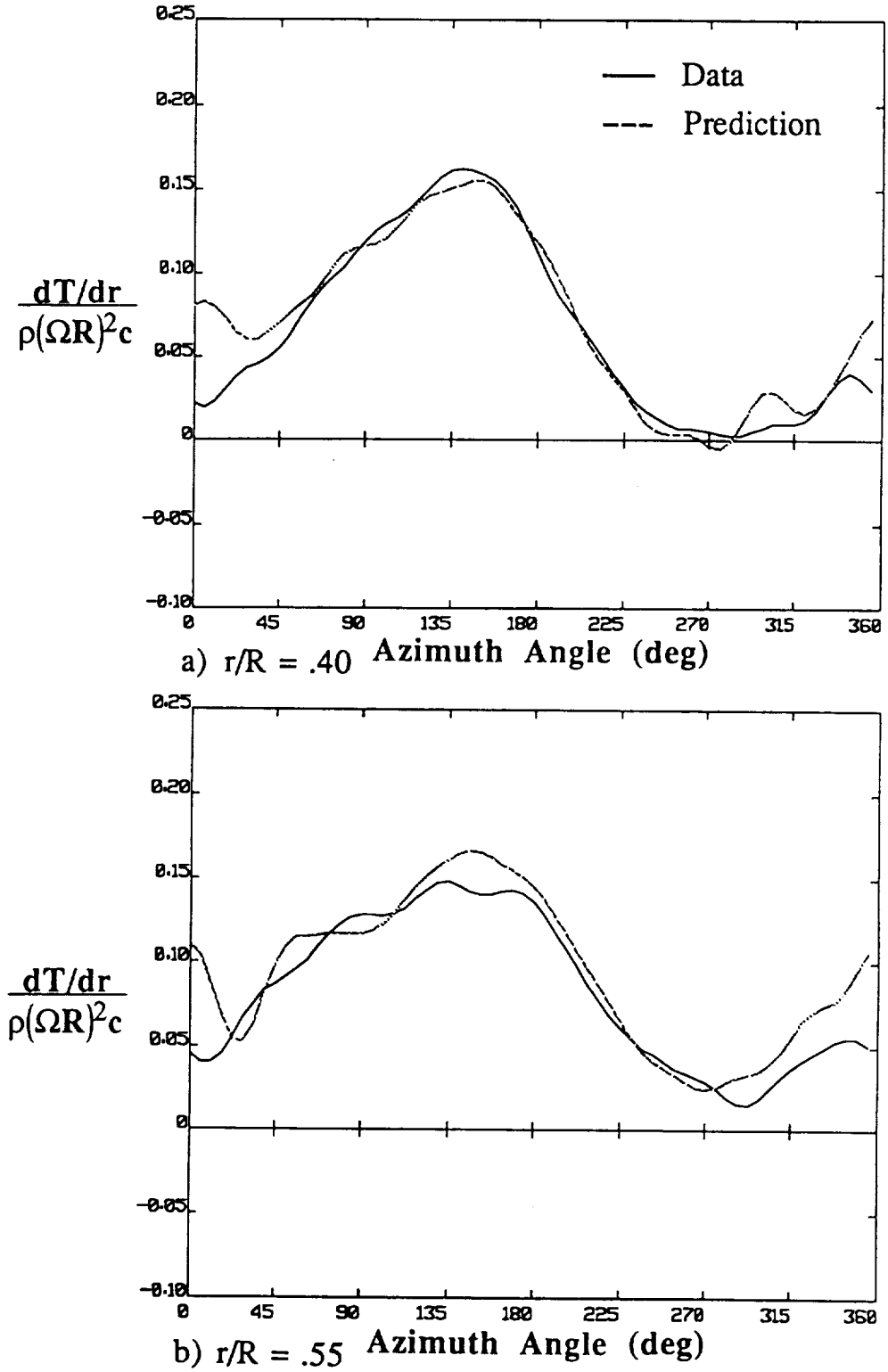

Figure 7-12. Nondimensional sectional thrust vs. azimuth angle for the H-34 rotor: advance ratio 0.39 , +5° shaft angle of attack.

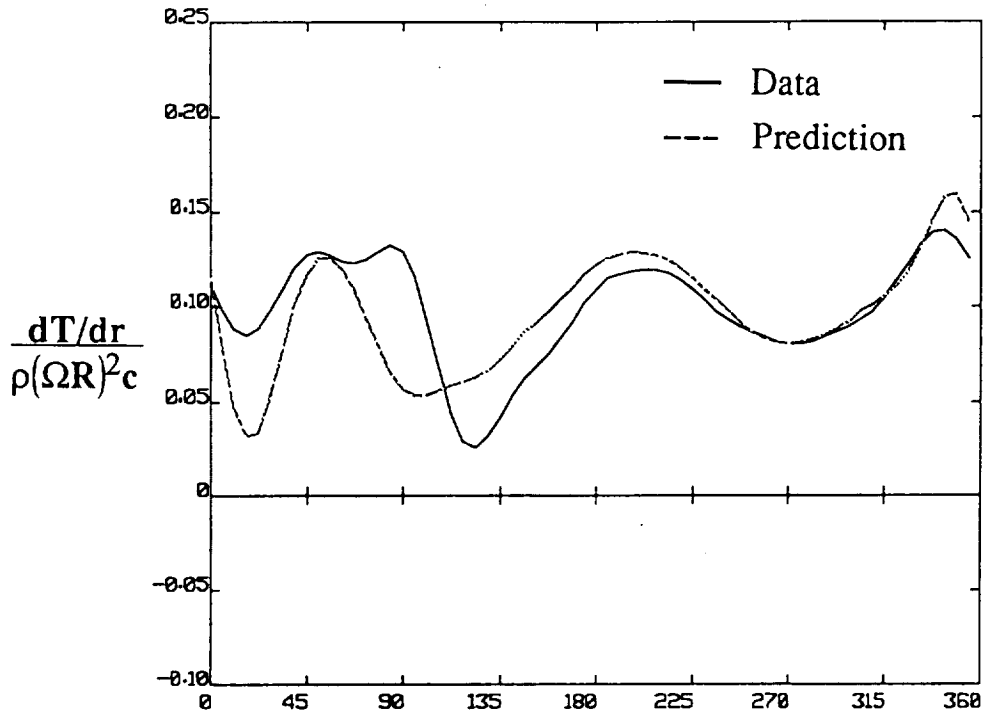

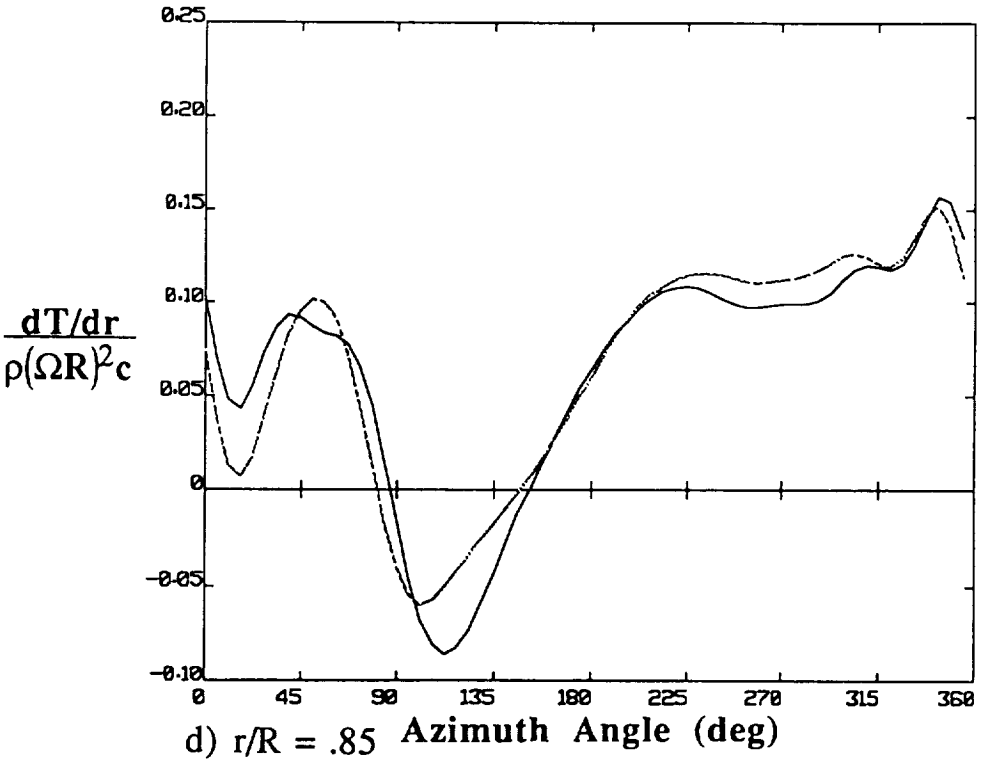

Figure 7-12 (Cont'd). Nondimensional sectional thrust vs. azimuth angle for the H-34 rotor: advance ratio 0.39 , +5° shaft angle of attack.

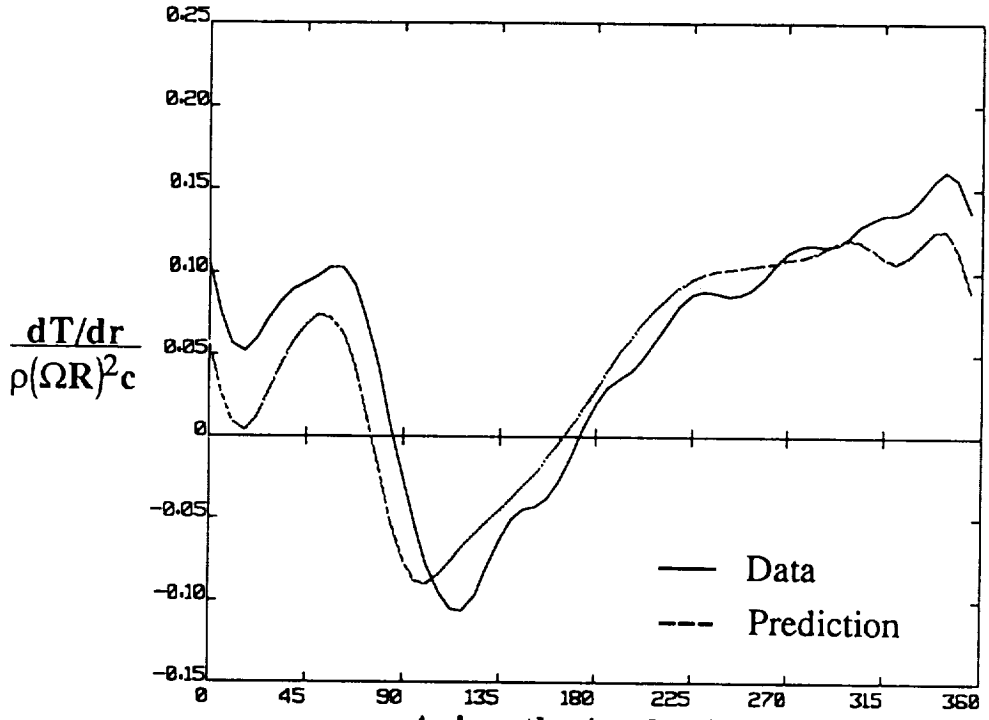

Figure 7-12 (Cont'd). Nondimensional sectional thrust vs. azimuth angle for the H-34 rotor: advance ratio 0.39 , +5° shaft angle of attack.

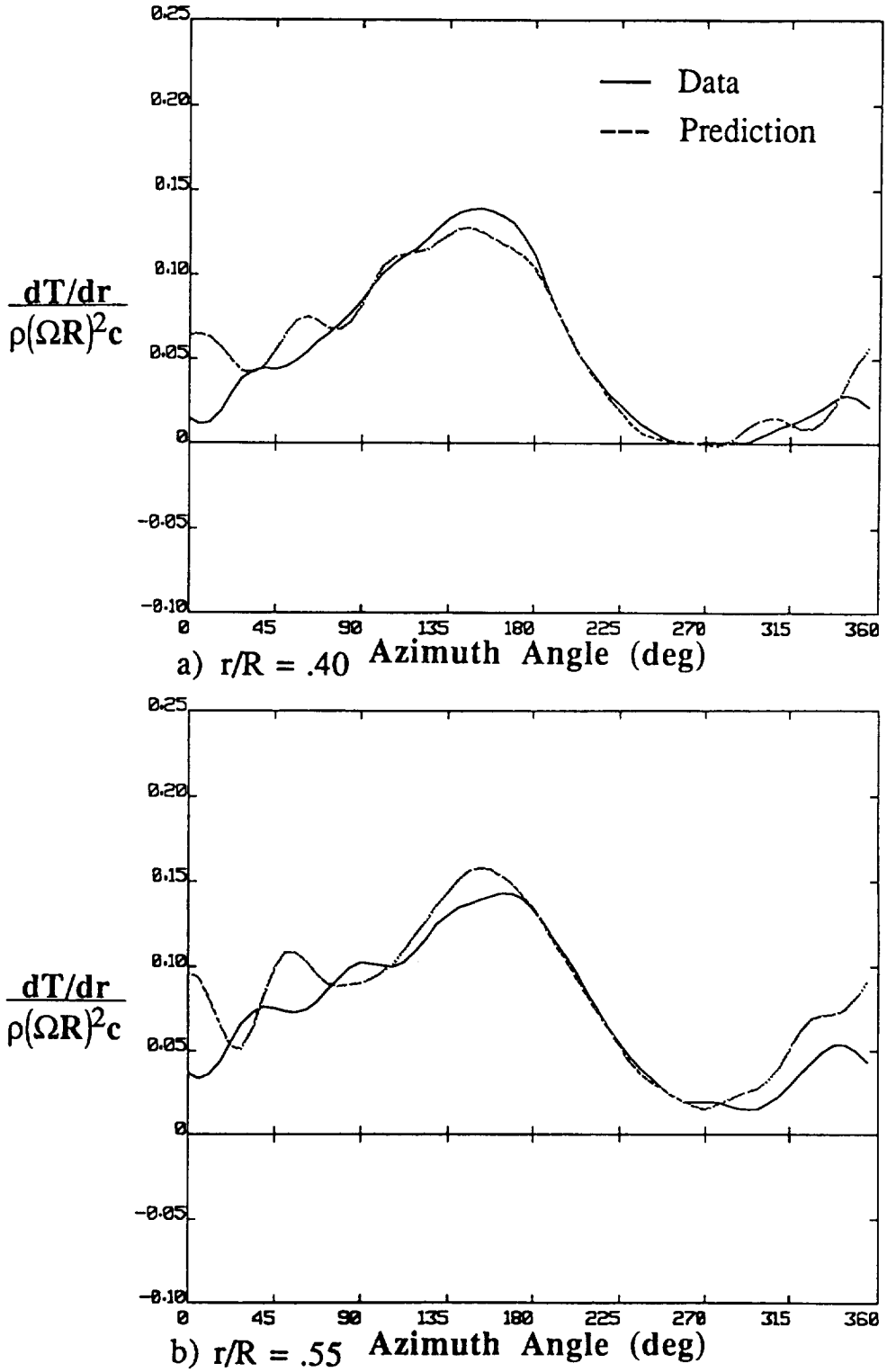

Figure 7-13. Nondimensional sectional thrust vs. azimuth angle for the H-34 rotor: advance ratio 0.39 , 0° shaft angle of attack.

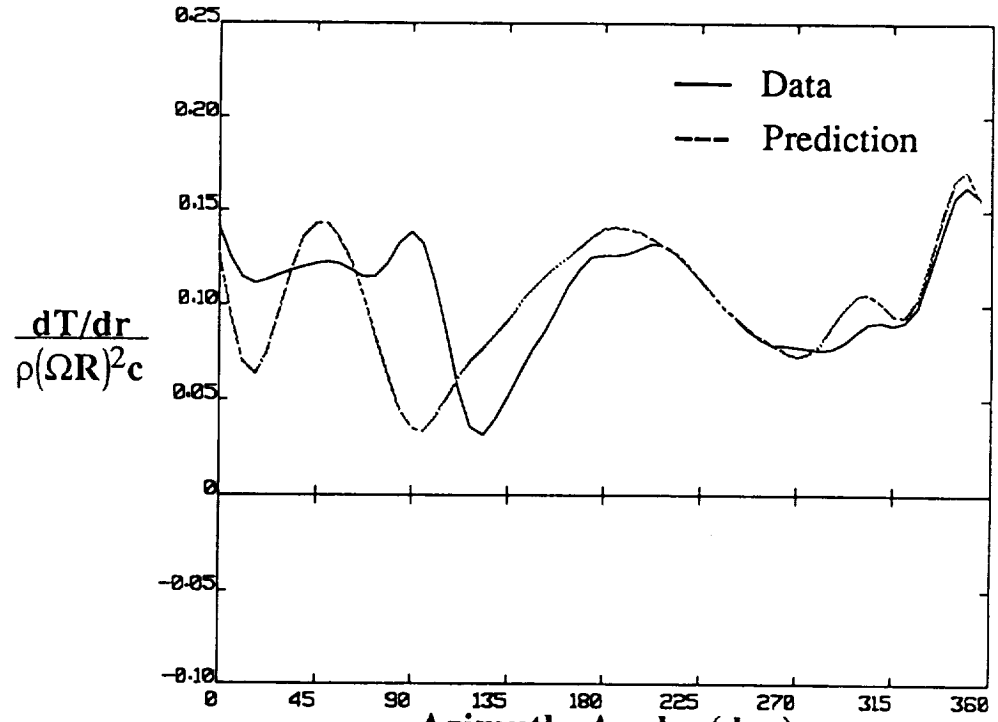

c) r/R = .75

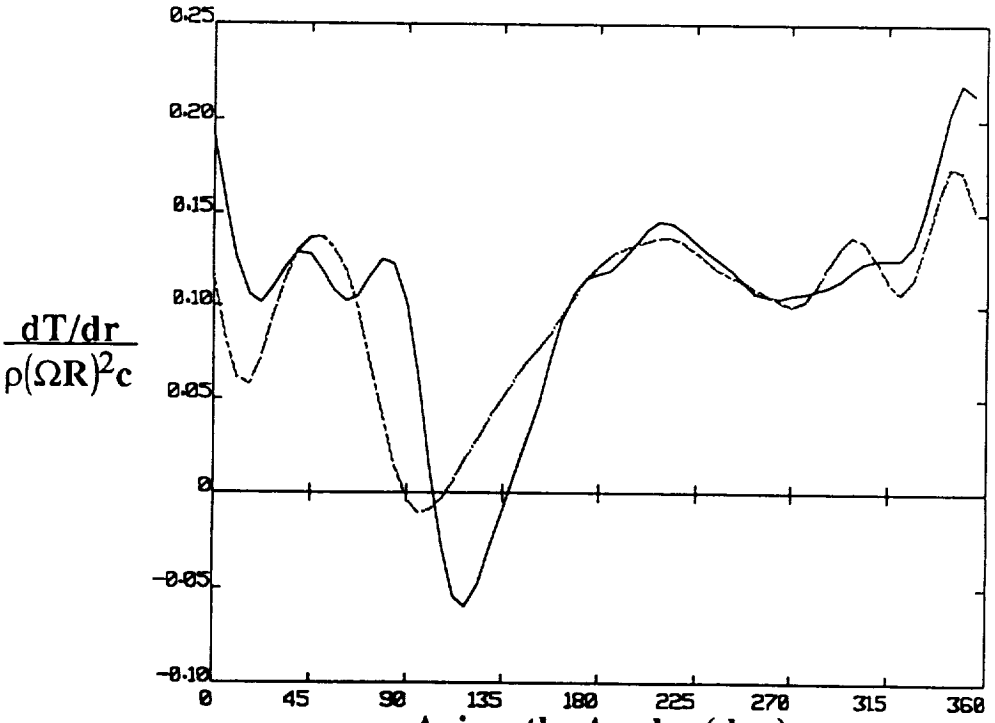

d) r/R = .85

Figure 7-13 (Cont'd). Nondimensional sectional thrust vs. azimuth angle for the H-34 rotor: advance ratio 0.39 , 0° shaft angle of attack.

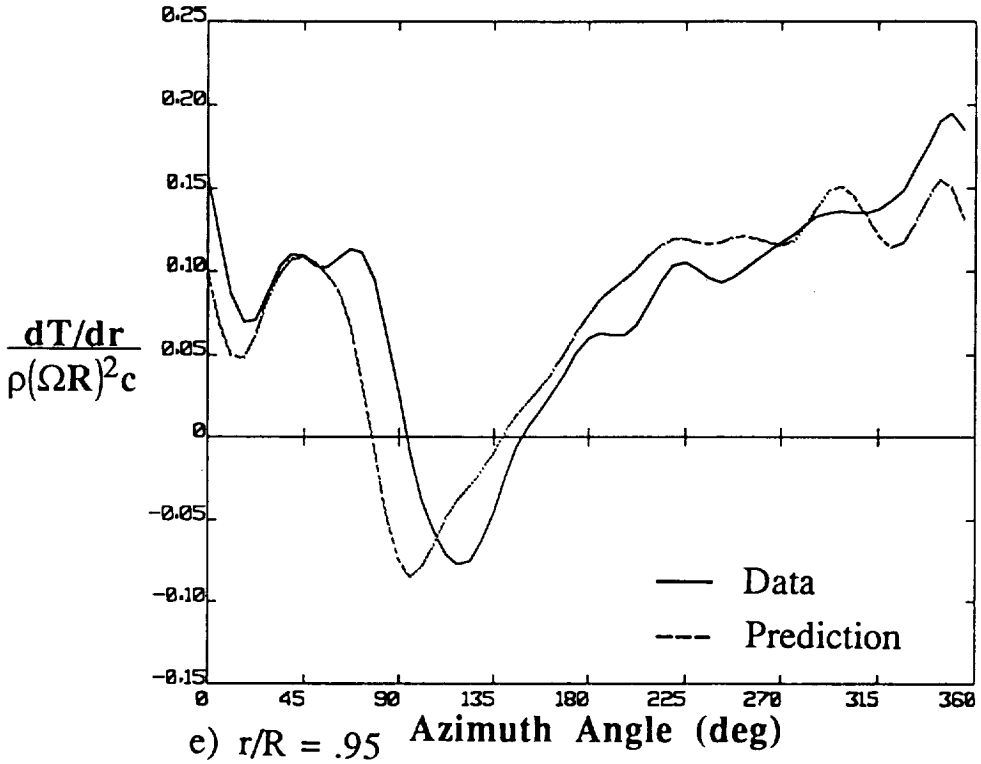

Figure 7-13 (Cont'd). Nondimensional sectional thrust vs. azimuth angle for the H-34 rotor: advance ratio 0.39 , 0° shaft angle of attack.

First note Figure 7-14, which shows the top view of the wake structure for the H-34 rotor and points out the major features of the vortex wake, including several closed loops corresponding to the wake of the negatively loaded tip vortex zone as well as the inboard wake, composed of several filaments trailing from the inboard portion of the blade. While providing substantial details of the structure of the wake, this figure only shows the wake of one blade at one instant and so is of limited usefulness in understanding the time varying flow field that characterizes blade/wake encounters. Figure 7-15 does not contain the complete details of the full-span wake, but it does show the major features of the wake of all of the blades as they interact with the reference blade (shaded black). The top portion of Figure 7-15 shows the time history of the upwash velocity (positive opposite the shaft Z axis) at the r/R=0.95 station on the reference blade for the shaft angle 0° case described in Figure 7-13. The letters A-D correspond to the various major wake/blade encounters around the azimuth.

Event A corresponds to the passage of the tip of the reference blade over the tip vortex trailed from a previous blade when passing through the third quadrant. Event B occurs because of the strong upwash/downwash experienced by the blade as it passes over the root vortex system. At the time indicated by Event C, the downwash induced by the combined effect of the root vortex and tip vortex systems at the reference blade is beginning to diminish, gradually reversing into an upwash velocity as the blade tip encounters the flow field generated by the opposite sign vorticity that trails from the negatively loaded tip region (Event D); note the the existence of negative loading at the tip in Figure 7-13e.

Because no flow field measurements are available for correlation to the predictions given in Figure 7-15, their validity can only be inferred through comparison to the loading data. Comparing the time history of upwash to the complete loading time history in Figure 7-13e suggests the wake-induced loading does behave much as indicated in Figure 7-15. However, the relationships involved are still clearer if only the higher harmonics of the airloads are plotted. Figure 7-16 shows both the predicted and measured time histories of airload at r/R = 0.95 with the lower harmonics (0 , 1 , and 2) removed. These residual higher harmonics are those that would generate the vibratory loads transmitted to the fuselage. Despite the complication introduced by the participation of structural deflection in the higher harmonic loading, the correspondence of the loading events to the wake-induced upwash is clear.

The predicted loading associated with event A in Figure 7-15 shows up in Figure 7-16, but it appears that the analysis overpredicts the size of this event. The characteristic up/down loading on the advancing side also is present, though its phasing leads the data by somewhat more than the five degrees of phase lag that can be accounted for in the data. The level of loading in this event is well predicted, an encouraging circumstance since many of the analyses discussed by Hooper in Reference 6 failed to achieve even qualitative correlation with the higher harmonic loading in this data set.

Another important feature of the higher harmonic loading is captured, namely the large up-down pulse around azimuth angle 0. Figure 7-15 makes clear that this event is associated with the passage of the blade over the portion of the wake composed of inboard trailing filaments. The presence of this detailed model of the inboard wake is thus clearly important for accurate reconstruction of the higher harmonic loading in this case. The importance of this mechanism suggests that the inboard wake deserves more detailed attention than it has received in rotor wake analyses to date. Analyses that use a single free tip vortex and smear out the inboard wake into a few large-core vortex filaments will miss this feature entirely, and it is clear that this interaction event makes a significant contribution to higher harmonic loading.

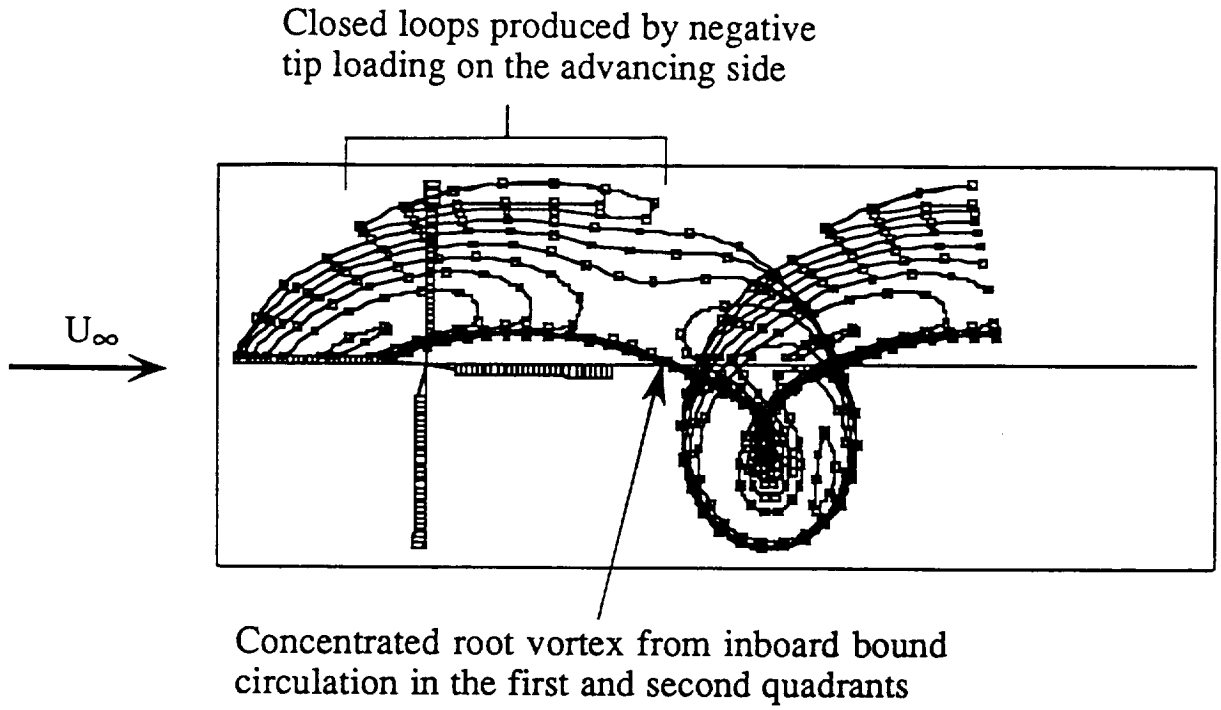

Figure 7-14. Top view of the wake of one blade of the H-34 rotor, reference blade at azimuth angle 180° . One and one quarter turns of full-span free wake shown.

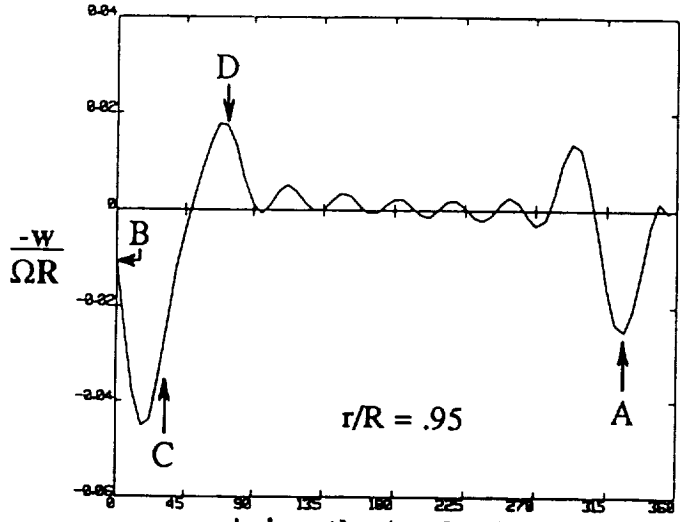

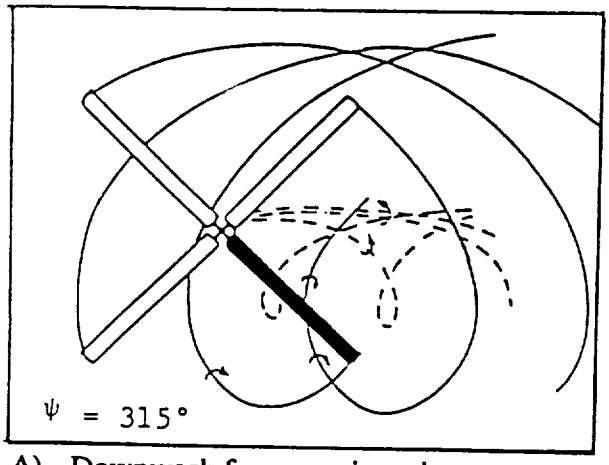

A) Downwash from previous tip vortex

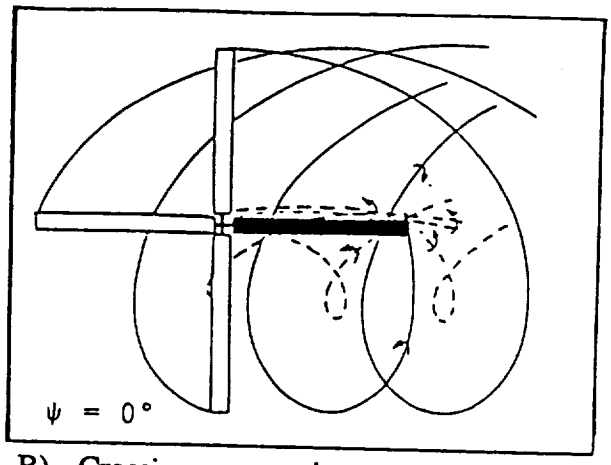

B) Crossing root vortices

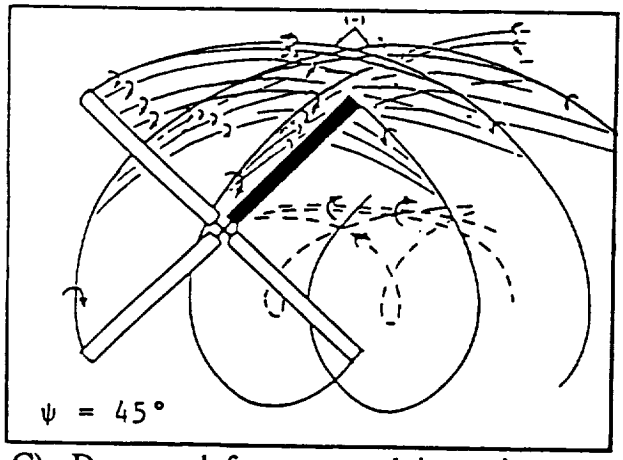

C) Downwash from root and tip vortices

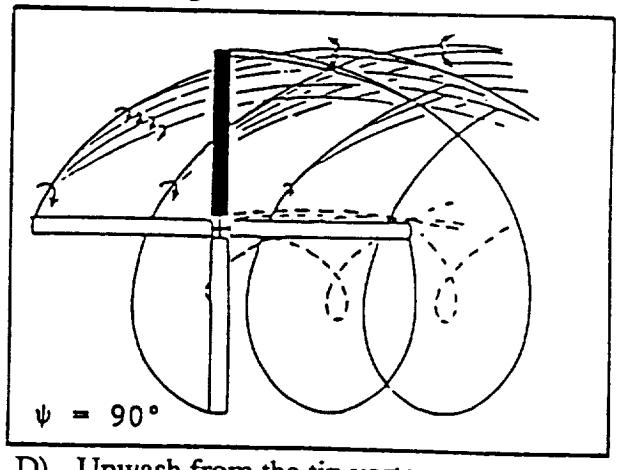

D) Upwash from the tip vortex system

Figure 7-15. Plot of upwash as a function of azimuth for the H-34 at advance ratio 0.39 , 0° shaft angle of attack. Events A-D correspond to the indicated blade/wake interaction events at $\psi = 315°$, 0° , 45° , and 90° .

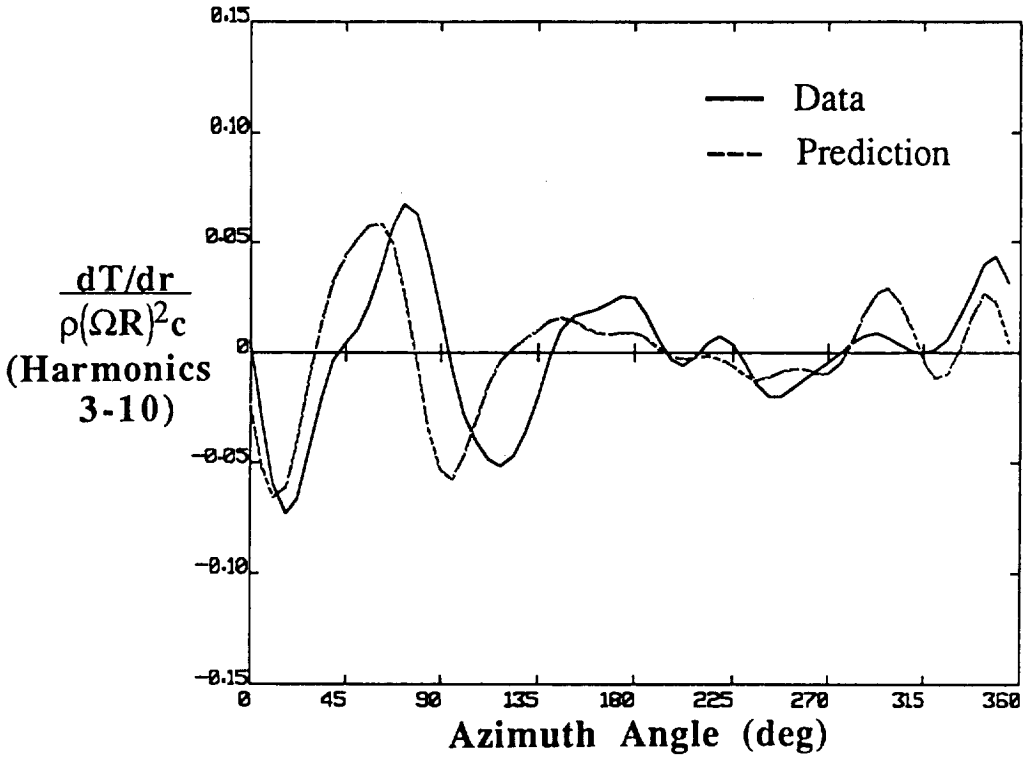

Figure 7-16. Higher harmonics (3P-10P) of airloading for the H-34 main rotor, advance ratio 0.39 , 0° shaft angle of attack.

In order to understand the mechanisms involved in these wake blade interactions more clearly, additional calculations were carried out with the intention of highlighting the contributions of various parts of the wake to the higher harmonic loading. This was accomplished by artificially inflating the vortex core size of filaments trailing from various portions of the blade. The results of this exercise are summarized in Figure 7-17. In Figure 7-17a, the baseline calculation of higher harmonics airloads for the 0° shaft angle case are shown along with the results of two supplementary calculations that were carried out with the core sizes for the trailing vortices set to one rotor radius, which should effectively delete their role in the calculation. The first case (labeled "tip vortices deleted") involved using this core adjustment on the vortices trailing from Zone 2 as well as the filaments trailing from the outer half of Zone 1, while leaving the remaining cores at the default sizes; the second case ("root vortices deleted") uses the adjusted cores on the filament on the inner half of Zone 1, while using default values for the remainder. In point of fact, since filaments trailed from the tip zone often loop around to join up with filaments from the root zone, this is not a truly consistent procedure for fully deleting the contributions of portions of the wake, but it does serve to emphasize the role of particular regions.

Figure 7-17a shows the results of these core modifications; 7-17b repeats them without the baseline calculation being plotted for clarity of comparison. The deletion of root vortex effects removes most of the up-down pulse around azimuth angle 0, while leaving strong contributions from the loading events around $\psi = 90$. This is intuitively reasonable, since Figure 7-15 indicates that the latter events are driven largely by interactions of the blade with wake trailed from the outboard regions of the blade. Conversely, the deletion of tip vortex events leaves the interaction around $\psi = 0$ as the major loading event; some residual loading in the first quadrant also remains. This comparison indicates the distinctive role of the inboard wake in the full-span wake model, and also highlights the contributions of the wake of the tip region. Clearly, both of these regions can make important contributions to the higher harmonic airloading of the rotor in high-speed flight conditions.

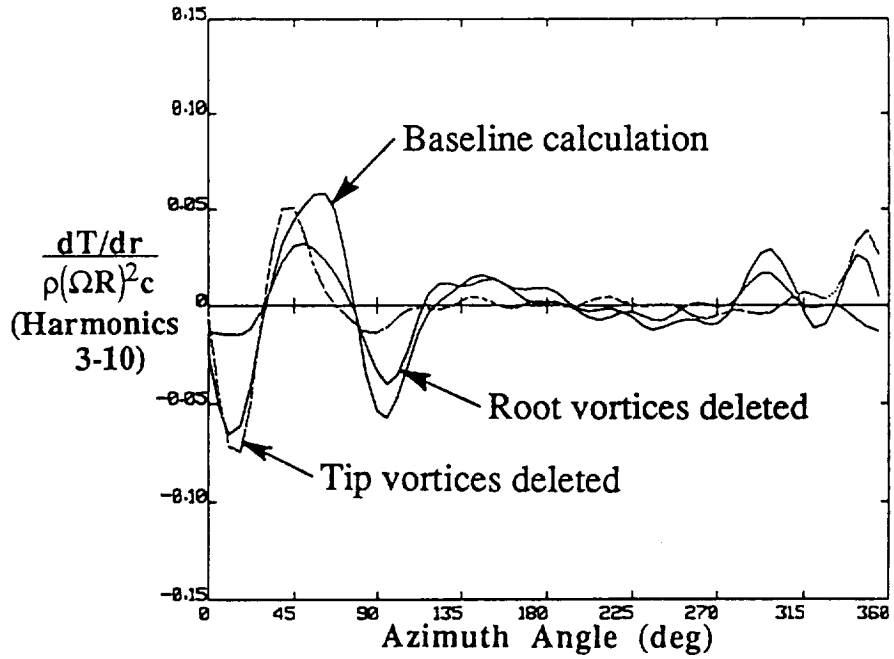

a) Comparison of all three results

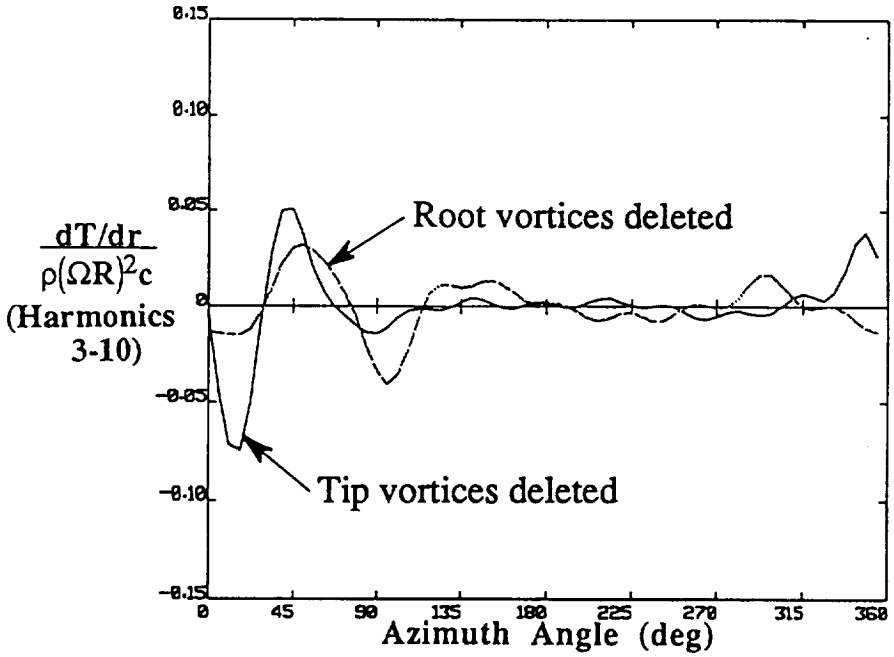

b) Case with tip vortices deleted and case with root vortices deleted

Figure 7-17. Comparison of predicted higher harmonic airloads using the complete wake model with two modified models: tip vortices deleted and root vortices deleted. (H-34 at advance ratio 0.39 , $\alpha_s = 0°$, r/R = 0.95)

8. SUMMARY

One of the primary objectives of this report has been to motivate the development of a new approach to helicopter rotor free wake modeling and to describe its implementation in the RotorCRAFT analysis. This description has included a discussion of the principles of full-span free wake modeling, focusing on the current approach to the discretization of the wake of the rotor blade into a set of constant-strength vortex filaments whose spacing and structure visibly reflect the time history of the loading on the rotor blades. As has been shown, this approach constitutes an exceptionally general and flexible model for the rotor wake of helicopters in both high-speed and low-speed flight.

Along with the description of the fundamental full-span model, another topic of interest has been the extension of this basic approach to include the potentially important effects of the far wake without impairing computational efficiency. The approach taken to this issue has featured the combination of a freely distorting two-filament extension of the full-span wake, several prescribed turns of discrete filamentary wake, and an analytical summation of remaining far wake effects for completeness. This combination of models will allow users of the RotorCRAFT analysis to tailor the structure of the far wake model to fit the particular flight condition of interest and to adapt to constraints on CPU time. Another important innovation in this last regard is the implementation of vortex elements based on Analytical Numerical Matching (ANM). Though not yet fully tested, sample problems run to date have indicated that free wake calculation using ANM may be expected to run in 30 to 50 percent less time than calculations using BCVEs with little or no sacrifice in accuracy. The ANM wake model may be invoked in the current code as an option, though the use of BCVEs is the preferred approach for the present.

The inclusion of a vortex lattice model of the blade has also been described, as have the modifications undertaken to the basic lattice model to incorporate the effects of viscous drag, yawed flow, and stall. The stall model currently in place has been found to produce qualitatively reasonable behavior in regions of high lift and is judged to be a substantial improvement relative to unmodified lattice models, which allow arbitrarily high generation of lift. As noted in Section 4, the current stall model directly replaces segments of the vortex lattice in stall with segments loaded according to two-dimensional tabulated coefficients. This approach can lead to sharp gradients in load at the boundary of stalled regions and so can produce unrealistic load distributions in some cases. An improved stall model is currently being explored that will operate by directly modifying the blade-on-blade influence coefficients in the vortex lattice solution method to reproduce the nonlinear lift behavior of particular sections. This improved model should produce smoother and hence more credible load distributions at stall boundaries and, if successful, will be included in the follow-on version of RotorCRAFT that is expected in early 1991.

A substantial portion of the discussion here has involved a description of the finite element structural model of the blade. As is clear from the discussion, this implementation permits considerable flexibility in the layout of the blade and introduces an important increment in sophistication of the model of blade deformation that was absent from earlier versions of the RotorCRAFT analysis.

The final portion of this report, containing the discussion of correlation runs with experimental data on rotor loading, was intended to both provide evidence of the code's suitability for application to challenging problems in rotor load prediction and to identify areas for further development. The calculations of integrated loading indicate a tendency to overpredict rotor torque required for a specified rotor lift, and it is speculated that one source of this overprediction is the absence of a compressibility tip relief model. This

effect and other candidate improvements to the current performance analysis will be considered as part of a continuing effort to improve the existing code.

As to the predictions of unsteady loading, the current version of RotorCRAFT produced good correlation with the SA-349 data and the H-34 flight test data, with some exceptions at particular radial stations. This indicates that RotorCRAFT performs well for rotors at low to moderate advance ratios. Correlation to high speed runs using the H-34 wind tunnel data set also produced generally favorable results both for overall loading at inboard stations and for stations near the rotor tip. However, substantial errors in level and phasing were observed, particularly for the .75R and .85R radial stations. The source of these errors is a topic of continuing investigation, though the exact extent of the problem is difficult to judge, given the uncertainties in the airload data measurements discussed in both Section 7.5 and Appendix B.

The final discussion of higher harmonic loading makes it clear that RotorCRAFT can capture significant features of the vibratory airloading of the H-34, and that the use of the full-span wake model is an essential component of this capability. This confirms the fundamental premise of this work, namely that the use of a full-span wake model is an essential prerequisite for accurate reconstruction of vibratory airloads in forward flight, However, it is equally clear that other features of the environment of typical rotors, notably the presence of transonic flow on the advancing side, can also play an important role in the determination of unsteady loading at high forward speeds. It is anticipated that this topic, along with enhancement of the current features of the code described above, will be prominent among the topics addressed in the continuing development of RotorCRAFT.

9. REFERENCES

1. Miller, R. H.: Rotor Blade Harmonic Air Loading. AIAA J., vol. 2, no. 7, July 1964.

2. Scully, M. P.: Computation of Helicopter Rotor Wake Geometry and its Influence on Rotor Harmonic Airloads. Massachusetts Institute of Technology Aeroelastic and Structures Research Laboratory, ASRL TR 178-1, March 1975.

3. Egolf, T. A.; and Landgrebe, A. J.: Helicopter Rotor Wake Geometry and its Influence in Forward Flight. Volumes I and II. NASA CR-3726 and 3727, October 1983.

4. Sadler, S. G.: Main Rotor Free Wake Geometry Effects on Blade Air Loads and Response for Helicopters in Steady Maneuvers. NASA CR-2110 and 2111, September 1972.

5. Johnson, W. J.: A Comprehensive Analytical Model of Rotorcraft Aerodynamics and Dynamics. NASA TM-81182, June 1980.

6. Hooper, W. E.: The Vibratory Airloading of Helicopter Rotors. Vertica, vol. 8, no. 2, 1984.

7. Miller, R. H.; and Ellis, S. C.: Prediction of Blade Airloads in Hovering and Forward Flight Using Free Wakes. Proceedings of the European Rotorcraft Forum, September 1986.

8. Johnson, W. R.: Wake Model for Helicopter Rotors in High Speed Flight. NASA CR-177507, November 1988.

9. Bliss, D. B.; Quackenbush, T. R.; and Bilanin, A. J.: A New Methodology for Helicopter Free Wake Analyses. Paper No. 83-39-75-0000 presented at the 39th Annual Forum of the American Helicopter Society, May 1983.

10. Bliss, D. B.; Teske, M. E.; and Quackenbush, T. R.: A New Methodology for Free Wake Analysis Using Curved Vortex Elements. NASA CR-3958, 1987.

11. Quackenbush, T. R.: Computational Studies in Low Speed Rotor Aerodynamics. Proceedings of the AHS National Specialists' Meeting on Rotor Aerodynamics and Aeroacoustics, February 1987.

12. Bliss, D. B.; Dadone, L. U.; and Wachspress, D. A.: Rotor Wake Modelling for High Speed Applications. Proceedings of the 43rd Annual Forum of the American Helicopter Society, May 1987.

13. Bliss, D. B.; and Wachspress, D. A.: A Free Wake Method for Improved Prediction of Higher Harmonic Airloads. Continuum Dynamics, Inc. Technical Report 85-1, January 1985.

14. Quackenbush, T. R.; Bliss, D. B.; and Wachspress, D. A.: Preliminary Development of an Advanced Free Wake Analysis of Rotor Unsteady Airloads. Final Report to NASA/Ames under contract NAS2-12554, August 1987.

15. Quackenbush, T. R.; Bliss, D. B.; Wachspress, D. A.; and McKillip, R. M.: Free Wake Analysis of Rotor Configurations for Reduced Vibratory Airloads. AHS National Specialists' Meeting, Arlington, Texas, November 1989.

16. Bliss, D. B.; and Miller, W. O.: Efficient Free Wake Calculations Using Analytical/Numerical Matching and Far Field Linearization. Proceedings of the 45th Annual Forum of the American Helicopter Society, May 1989.

17. Bliss, D. B.; and Miller, W. O.: Vortex Filament Calculations by Analytical/Numerical Matching with Comparison to Other Methods. AIAA Paper 89-1962, presented at the AIAA 20th Fluid Mechanics Conference, June 1989.

18. Harris, F. J.: Rotor Wing Aerodynamics – Historical Perspective and Important Issues. AHS National Specialists' Meeting on Aerodynamics and Aeroacoustics, Southwest Region, February 1987.

19. Egolf, T. A.: Helicopter Free Wake Prediction of Complex Wake Structures Under Blade-Vortex Interaction Conditions. Proceedings of the 44th Annual Forum of the American Helicopter Society, June 1988.

20. Maskew, B.: A Quadrilateral Vortex Method Applied to Configuration with High Circulation. Vortex Lattice Utilization. NASA SP-405, May 1976.

21. Johnson, W.: Helicopter Theory, Chapter 4, Princeton University Press, 1980.

22. Bliss, D. B.: Prediction of Tip Vortex Self-Induced Motion Parameters in Terms of Rotor Blade Loading. Proceedings of the American Helicopter Society National Specialists' Meeting on Aerodynamics and Aeroacoustics, February 1987.

23. Quackenbush, T. R., et al.; Free Wake Analysis of Hovering Performance Using a New Influence Coefficient Method. NASA CR-4309, July 1990.

24. Rehbach, C.: Numerical Calculation of Unsteady Three-Dimensional Flows with Vortex Sheets. AIAA Paper 78-111, presented at the AIAA 16th Aerospace Science Meeting, Huntsville, Alabama, 1978.

25. Chua, K.; Leonard, A.; Pepin, F.; and Winckelmans, G.: Robust Vortex Methods for Three-Dimensional Incompressible Flows, presented at the meeting of ASME, Chicago, Illinois, 1988. In: Recent Developments in Computational Fluid Dynamics, Tezduyar, T. and Hughes, T. eds., pp. 33-44.

26. Leonard, A.; and Chua, K.: Three-Dimensional Interactions of Vortex Tubes. Physica D, vol. 37, 1989, p. 490.

27. Anderson, C.; and Greengard, C.: On Vortex Methods. SIAM J. Numerical Analysis, vol. 22, 1984, p. 413.

28. Beale, J. T.; and Majda, A.: Vortex Methods I: Convergence in Accuracy in Two and Three Dimensions. Mathematics of Computation, vol. 39, 1982, p. 1.

29. Cottet, G. H.: Methode Particulaire pour l'Equation d'Euler dans le Plan. These de 3eme cycle, Universite Paris IV, 1982.

30. Hess, J. L.: Review of the Historical Development of Surface Source Methods, in Computational Methods in Potential Aerodynamics, Springer-Verlag, New York, 1985.

31. Johnson, F. T.; and Rubbert, P. E.: Advanced Panel-Type Influence Coefficient Methods Applied to Subsonic Flows. AIAA Paper 75-50, 1975.

32. Falkner, V. V.: The Calculation of Aerodynamic Loading on Surfaces of Any Shape. Aeronautical Research Council, R&M 1910, August 1943.

33. Rubbert, P. E., et al.: A General Method for Determining the Aerodynamic Characteristics of Fan-in-Wing Configurations, vol. 1, USAAVLABS TR 67-614, 1967.

34. Margason, R. J.; and Lamar, J. E.: Vortex Lattice FORTRAN Program for Estimating Subsonic Aerodynamic Characteristics of Complex Planforms. NASA TN-D 6142, 1971.

35. Kocurek, J. D.: A Lifting Surface Performance Analysis with Circulation Coupled Wake for Advanced Configuration Hovering Rotors. Ph.D. Thesis, Texas A&M University, May 1978.

36. Summa, J. M.; and Clark, D. R.: A Lifting Surface Method for Hover/Climb Airloads. Proceedings of the 35th Annual Forum of the American Helicopter Society, May 1979.

37. Chiu, Y. D.: Convergence of Discrete-Vortex Induced-Flow Calculations by Optimum Choice of Mesh. Ph.D. Thesis, Georgia Institute of Technology, School of Aerospace Engineering, August 1988.

38. Hough, G. R.: Lattice Arrangement of Rapid Convergence. Vortex Lattice Utilization. NASA SP-405, May 1976.

39. Wachspress, D. A.; Quackenbush, T. R.; and Boschitsch, A. H.: RotorCRAFT (Mod. 0.0) User's Manual, Continuum Dynamics, Inc., Technical Note 90-13, October 1990.

40. Celi, R.; and Friedmann, P. P.: Aeroelastic Modeling of Swept Tip Rotor Blades Using Finite Elements. J. AHS, vol. 33, no. 2, April 1988, pp. 43-52.

41. Brush, D. O.; and Almroth, B. O.: Buckling of Bars, Plates and Shells, McGraw-Hill Book Co., 1975.

42. Bathe, K. J.: Finite Element Procedures in Engineering Analysis, Prentice-Hall, Inc., 1982.

43. McCloud, J. L., III; and Biggers, J. C.: An Investigation of Full-Scale Helicopter Rotors at High Advance Ratios and Advancing Tip Mach Numbers. NASA TND-4632, July 1968.

44. Rabbott, J. P., Jr.; Lizak, A. A.; and Paglino, V. M.: A Presentation of Measured and Calculated Full-Scale Rotor Blade Aerodynamic and Structural Loads. USAAVLABS, TR-66-31, July 1966.

45. Harris, F. D.: Articulated Rotor Blade Flapping Motion at Low Advance Ratio, J. American Helicopter Society, vol. 17, no. 1, January 1972.

46. Johnson, W.: Comparison of Calculated and Measured Helicopter Rotor Lateral Flapping Angles. NASA TM-81213, July 1980.

47. Miller, W. O.; and Bliss, D. B.: Direct Periodic Solutions of Rotor Free Wake Calculations by Inversion of a Linear Periodic System. Proceedings of the 46th Annual Forum of the American Helicopter Society, Washington, D.C., May 1990.

48. Scheiman, J.: A Tabulation of Helicopter Rotor-Blade Differential Pressures, Stresses, and Motions Measured in Flight. NASA TM-X 952, March 1974.

49. Heffernan, R. M., et al.: Structural and Aerodynamic Loads and Performance Measurements of an SA349/2 Helicopter with an Advanced Geometry Rotor. NASA TM-88370, November 1986.

50. Chigier, N. A.; and Corsiglia, V. R.: Tip Vortices; Velocity Distributions. NASA TM-X-62, September 1971.

APPENDIX A

EIGENCALCULATION SOLUTION METHOD FOR ROTOR BLADE MODAL PROPERTIES

A.1 Formulation

The eigenvectors, $\{x_i\}$, specify the nodal displacements that characterize a given mode shape. It is convenient to interpolate these nodal displacements using the individual element shape functions to obtain:

$\Phi_i(r,k)$

where, i	refers to the particular mode
r	radial distance along X-axis of a point on the blade
k=1,2,3	displacements,U, V, -W in the X,Y,and -Z directions
k=4,5,6	rotations, R_X, R_Y and R_Z, about the X,Y,Z axes, or equivalently, twist, θ_X, about X, and slopes, $-\partial W/\partial X$ and $\partial V/\partial X$, respectively

XYZ are the blade-fixed coordinates as shown in Figure 5-1. Note the negative signs on the W displacement. Positive W occurs in the positive Z direction. However Φ_i should contain -W as the third coordinate. The user of the RotorCRAFT code has the option of specifying the mode shapes explicitly rather than computing these from the blade stiffness and mass properties. This amounts to evaluating the mode shapes, $\Phi_i(r,k)$, at a sequence of radial locations, r=r(ir) , to define an array:

$$\text{SHAPES}\ (i,ir,k) = \Phi_i(\ r(ir),k\ ) \tag{A.1}$$

The generalized masses are defined as:

$$GM(i) = \{x_i\}^T [\ M_{rr}\ ]\ \{x_i\} \tag{A.2a}$$

(in many eigencalculations GM(i) = 1 by virtue of the way that the eigenvectors are normalized). If assumed modeshapes have been used then the generalized mass can also be expressed as:

$$GM(i) \equiv \int_0^R \sigma_G(r)\ \{\ \Phi_i^2(r,1) + \Phi_i^2(r,2) + \Phi_i^2(r,3)\ \} + J_G^m(r)\ \Phi_i^2(r,4)\ dr \tag{A.2b}$$

where $\sigma_G(r)$ is the mass per unit length along X and $J_G^m(r)$ is the second moment of inertia per unit length about an axis parallel to the blade X-axis and intersecting the local elastic axis. (Note that σ_G and J_G^m are referred to the global axes, XYZ , whereas the cross-section input parameters in the finite element (F.E.) analysis, σ and J^m are referred to the local axes.)

A.2 Rotation Due to Cyclic Pitch

The cyclic pitch acceleration introduces a forcing term into the modal equations involving torsional deformations. In order to account for the cyclic pitch at the root additional information must be furnished.

Let the vector, $\{r_{\theta_c}\}$ be the vector describing the rigid body displacement of the structure due to a unit twist at the root. This can be either computed directly from the geometry of the blade, or from:

$$\{r_{\theta_c}\} = -[K_{rr}]^{-1}[K_{r\theta_c}] \tag{A.3}$$

where $[K_{r\theta_c}]$ is the column of the stiffness matrix associated with the twist degree of freedom of the root node. This is contained in the matrix partition, $[K_{rc}]$, defined in Equation 5.35. Then the displacement at each node due to rigid body motion arising from cyclic pitch is simply, $\{r_{\theta_c}\}\theta_c(t)$. Note that the components of the vector, $\{r_{\theta_c}\}$, can also be obtained directly from the geometry as:

$$\begin{array}{lll} U = 0 & ; \quad V = -r_Z & ; \quad W = r_Y \\ \theta_X = 1 & ; \quad R_Y = 0 & ; \quad R_Z = 0 \end{array} \tag{A.4}$$

where r_Y and r_Z are the perpendicular distances of the elastic axis from the cyclic pitch axis, X, in the Y and Z directions.

A.3 Modal Equations

The remaining derivation assumes a F.E. setting. However, those quantities required as inputs to the code for users desiring to input their own mode shapes are defined independently of F.E. parameters, as is seen below. The equations of motion defining the evolution of the DOF, $q_r(t)$, are then,

$$[M_{r\theta_c} : M_{rr}] \begin{Bmatrix} \ddot{\theta}_c \\ \cdots \\ \ddot{q}_r \end{Bmatrix} + [K_{r\theta_c} : K_{rr}] \begin{Bmatrix} \theta_c \\ \cdots \\ q_r \end{Bmatrix} = \{F^{aero}\} + \{F^{rot}\} \tag{A.5}$$

where $[M_{r\theta_c}]$ and $[K_{r\theta_c}]$ are the column of the mass and stiffness matrices associated with the root twist, $\{F^{aero}\}$ are the nodal forces due to aerodynamic loads and $\{F^{rot}\}$ the nodal forces associated with the blade rotation. Note that none of the other constrained degrees of freedom, U, V, W, etc., at the root enter Equation A.5 since there is no forcing along these directions. The only non-zero root displacements is θ_c. Furthermore, it is clear that the generalized coordinate vector, $\{q_r\}$, includes both deformation effects and the rigid body rotation due to cyclic pitch. Rearranging Equation A.5:

$$[M_{rr}]\{\ddot{q}_r\} + [K_{rr}]\{q_r\} = \{F^{aero}\} + \{F^{rot}\} - ([M_{r\theta_c}]\ddot{\theta}_c + [K_{r\theta_c}]\theta_c) \quad (A.6)$$

The elastic deformation variables $\{q\}$ are determined by subtracting out the rigid body motion arising from cyclic pitch:

$$\{q\} = \{q_r\} - \{r_{\theta_c}\}\theta_c \; ; \qquad \{\ddot{q}\} = \{\ddot{q}_r\} - \{r_{\theta_c}\}\ddot{\theta}_c \quad (A.7)$$

Then, Equation A.6 becomes,

$$\begin{aligned}[M_{rr}]\{\ddot{q}\} + [K_{rr}]\{q\} &= \{F^{aero}\} + \{F^{rot}\} \\ &\quad - ([M_{r\theta_c}]+[M_{rr}]\{r_{\theta_c}\})\ddot{\theta}_c + ([K_{r\theta_c}]+[K_{rr}]\{r_{\theta_c}\}) \theta_c \\ &= \{F^{aero}\} + \{F^{rot}\} - ([M_{r\theta_c}] + [M_{rr}]\{r_{\theta_c}\})\ddot{\theta}_c \quad (A.8)\end{aligned}$$

where expression Equation A.3 has been used

Modal coordinates, $\{\eta\}$, defined by $\{q\}=[X]\{\eta\}$, are now introduced. Here the modal matrix, $[X]=[\{x_i\}]$, is composed of the first N_m eigenvectors, $\{x_i\}$, that have been retained in the analysis. These eigenvectors and the corresponding natural frequencies, ω_i^2 are the non-trivial solutions to the generalized eigenvalue problem, Equation 5.36. Equation A.8 may then be transformed into the modal variables by pre-multiplying by $[X]^T$ and substituting $\{q\}=[X]\{\eta\}$:

$$\begin{aligned}&[X]^T[\, M_{rr}\,][X]\{\ddot{\eta}\} + [X]^T[\, K_{rr}\,][X]\{\eta\} \\ &\qquad = [X]^T [\, \{F^{aero}\} + \{F^{rot}\} - ([M_{r\theta_c}] + [M_{rr}]\{r_{\theta_c}\})\ddot{\theta}_c \,]\end{aligned}$$

$$\text{or,} \quad GM(i)\,[\,\ddot{\eta}_i + \omega_i^2\,\eta_i\,] = F^{AERO}_{(i)} + F^{ROT}_{(i)} - MRC(i)\,\ddot{\theta}_c \quad (A.9)$$

The generalized modal force due to aerodynamic loading,

$$F^{AERO}_{(i)} = \int_{HINGE}^{r=RADIUS} \{f_X^{AERO} \;\; f_Y^{AERO} \;\; f_Z^{AERO} \;\; m_X^{AERO}\} \begin{Bmatrix} \Phi_i(r,1) \\ \Phi_i(r,2) \\ -\Phi_i(r,3) \\ \Phi_i(r,4) \end{Bmatrix} dr \quad (A.10a)$$

where f_X^{AERO}, f_Y^{AERO}, and f_Z^{AERO} are the global axes components of the aerodynamic force per unit length, and m_X^{AERO} is the aerodynamic moment per unit length about an axis parallel to the X-axis and passing through the local elastic axis $F^{AERO}_{(i)}$, is approximated in RotorCRAFT via the discrete sum,

$$F^{AERO}_{(i)} = \sum_{ir} \{DDIS(ir)\ \ TDIS(ir)\ \ MDIS(ir)\} \begin{Bmatrix} SHAPES(i,ir,2) \\ SHAPES(i,ir,3) \\ SHAPES(i,ir,4) \end{Bmatrix} \qquad (A.10b)$$

where, MDIS(ir) = QMDIS(ir) - TDIS(ir)*ELOFF(ir) and DDIS(ir) , TDIS(ir) , and QMDIS(ir) , are the arrays used in RotorCRAFT to store the drag, thrust, and pitching moment of a chord segment at point, ir (see Ref.39). ELOFF(ir) is the array used in RotorCRAFT specifying the distance of the elastic axis behind the quarter chord point in the global Y-direction at radial station ir . The modal force due to blade rotation,

$$F^{ROT}_{(i)} = \{x_i\}^T \{F^{rot}\} \qquad (A.11a)$$

If mode shapes are defined by the user, then

$$F^{ROT}_{(i)} = \int_{r=HINGE}^{r=RADIUS} \{f_X^{ROT}\ \ f_Y^{ROT}\ \ f_Z^{ROT}\ \ m_X^{ROT}\} \begin{Bmatrix} \Phi_i(r,1) \\ \Phi_i(r,2) \\ -\Phi_i(r,3) \\ \Phi_i(r,4) \end{Bmatrix} dr \qquad (A.11b)$$

where f_X^{ROT} , f_Y^{ROT} , and f_Z^{ROT} are the global axes components of the force per unit length due to blade rotation, and m_X^{ROT} is the blade rotation twisting moment per unit length about an axis parallel to X and coincident with the local elastic axis. Note here the sign of $\Phi_i(r,3)$ which is due to the fact that the displacement, $\Phi_i(r,3)=-W$, is in the negative Z-direction. The quantity incorporating the inertial effects of cyclic pitch into the modal equation,

$$MRC(i) = \{x_i\}^T ([M_{r\theta_C}] + [M_{rr}]\{r_{\theta_C}\}) \qquad (A.12a)$$

or, if mode shapes are input separately,

$$MRC(i) = \int_{r=HINGE}^{r=RADIUS} \{ -\sigma_G(r) r_Z\ \ \sigma_G(r) r_Y\ \ J_G^m\} \begin{Bmatrix} \Phi_i(r,2) \\ -\Phi_i(r,3) \\ \Phi_i(r,4) \end{Bmatrix} dr \qquad (A.12b)$$

where σ_G and J_G^m have already been defined for Equation A.2b and the moment arms, r_Y and r_Z , are defined in Equations A.4.

Finally by dividing through by GM(i) and normalizing the time by $\tau=t/\Omega$, one obtains the modal equations:

$$\eta_i'' + \omega_\eta^2 \eta_i = \frac{1}{GM(i)\,\Omega^2} [F^{AERO}_{(i)} + F^{ROT}_{(i)} - MRC(i)\,\ddot{\theta}_C] \qquad (A.13)$$

where the normalized angular frequency, $\omega_\eta = \omega_i/\Omega$.

APPENDIX B

ACCURACY OF MEASURED LOADING ON BLADE SECTIONS IN TRANSONIC FLOW

Assessment of the overall predictive capability of the RotorCRAFT code has been primarily based on comparisons of measured airloads with code predictions. These airloads were obtained by measuring the pressures at discrete chordwise locations for a specified radial station with pressure transducers and then integrating over the chord. As a result of spatial constraints, these chordwise pressure transducer locations are often limited to relatively small numbers (between five and eleven in a typical test, such as Ref. 44) and it is the purpose of this limited study to estimate the error in airloads associated with integrating these discrete pressures over the blade chord.

Transonic airfoil pressure distributions have been measured extensively on NACA 0012 airfoils in several carefully controlled tests (Ref. B-1). Characteristic of transonic pressure distributions on this airfoil is a strong shock wave which leads to pressure recovery on the airfoil as the flow approaches the trailing edge. Data is reproduced in Figure B-1 which gives the measured pressure distribution at Mach .747 angle of attack of about 3°. This Mach number and angle of attack were judged to be reasonably representative of the blade operating condition at stations near the advancing tip of rotors in high speed flight. Pressure taps used to obtain this data in Reference B-1 were on the average, at a spacing of 3% of chord, much higher than is typically used in helicopter flight or wind tunnel tests.

Since substantial use was made of the Sikorsky H-34 full-scale data, an estimate of the error in computed airload was undertaken in an attempt to quantify what constitutes acceptable data / rotorcraft airloads comparisons. Table B-1 below shows the chordwise locations of pressure taps as a function of radial position on the blade. It is significant that the tip of the blade is sparsely instrumented and that the highest chordwise resolution of pressure is located at 85% of rotor radius.

Figure B-2 shows the results of integrating the pressure data of Figure B-1 as a function of discretization of the load distribution. The error presented here is the deviation of total sectional load computed with various discretizations of the chordwise load distribution to the total load measured by the wind tunnel balance in Reference B-1. The error denoted by plus signs results when the load is uniformly discretized in the chord direction, while the triangular symbols denote the discretization resulting from the pressure tap locations in Table B-1. Note that integration of the chordwise pressure distribution can introduce significant errors in the sectional load. These errors will in general be greater still for larger angle of attack or for higher Mach number. It is reasonably safe to conclude that for higher Mach number data outboard of the 85% radial position, errors in excess of ± 8% may exist in the integrated data.

Reference:

B-1. Thibert, J.J., Grandjacques, M. and Ohman, L.H.: "NACA 0012 Airfoil" AGARD-AR-138, Report of the Fluid Dynamics Panel Working Group 4, May 1979.

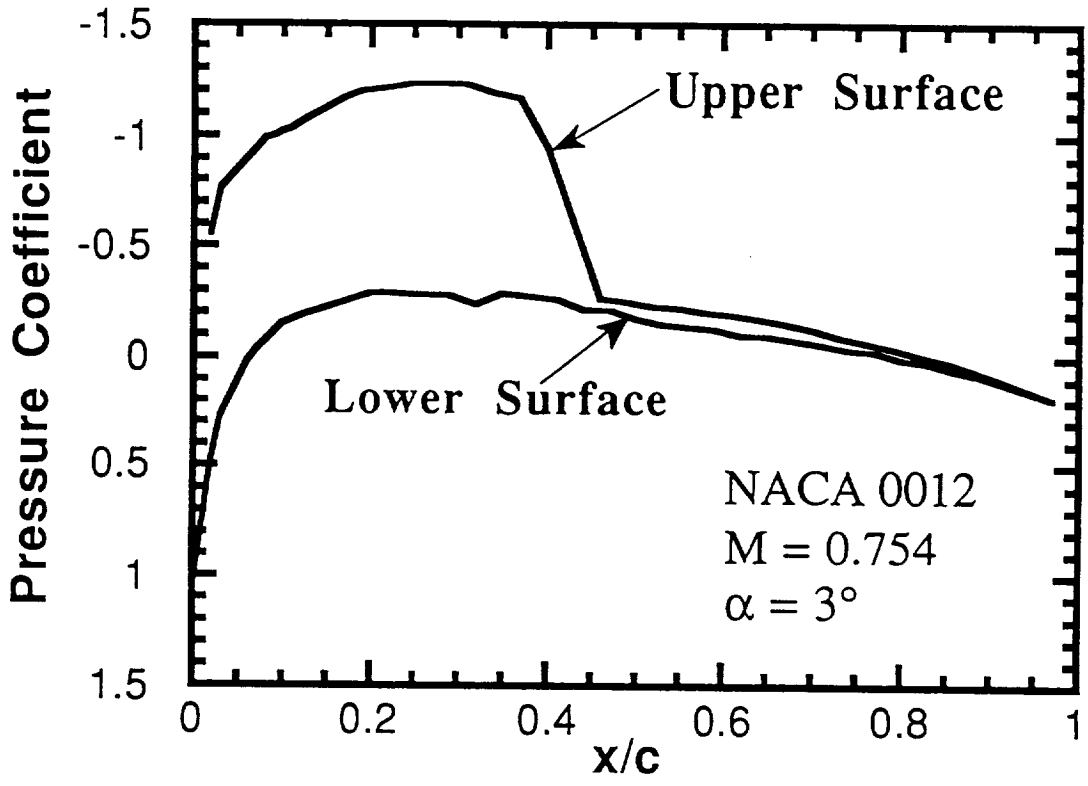

Figure B-1. Chordwise pressure distribution over a NACA 0012 airfoil.

TABLE B-1

Location of Pressure Taps (Ref. 44)

X/C AT r/R =	.25	.40	.55	.75	.85	.90	.95	.97	.99
	.042	.042	.017	.017	.017	.017	.017	.090	.101
	.158	.158	.090	.090	.040	.090	.090	.230	.290
	.300	.300	.168	.168	.090	.158	.168	.565	.737
	.600	.600	.233	.233	.130	.233	.233	.850	
	.910	.910	.335	.335	.168	.333	.335		
			.625	.625	.233	.625	.625		
			.915	.915	.335	.915	.915		
					.500				
					.625				
					.769				
					.915				

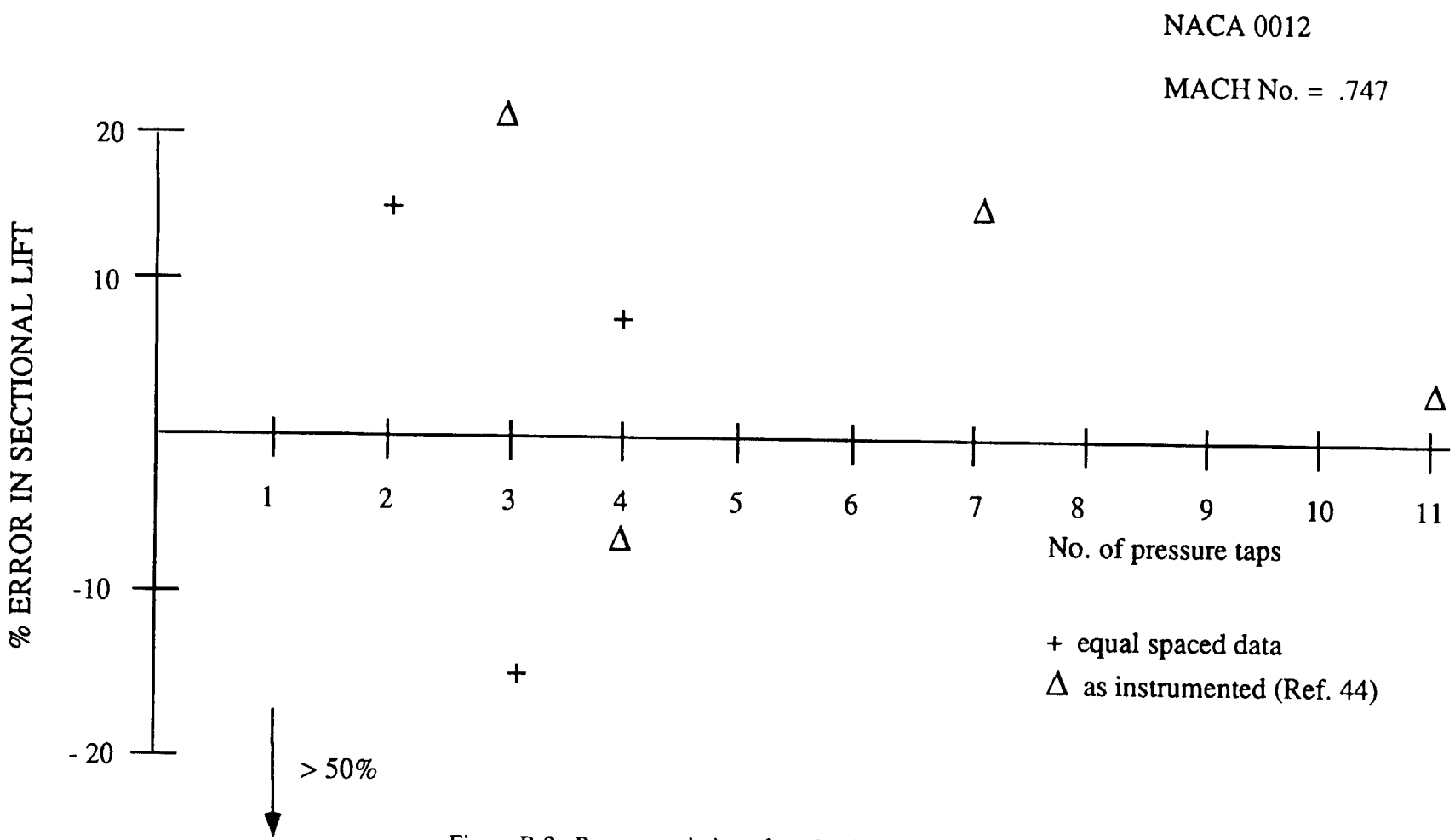

Figure B-2. Percent variation of section load (from integration) divided by measured sectional load.

REPORT DOCUMENTATION PAGE

Form Approved
OMB No. 0704-0188

Public reporting burden for this collection of information is estimated to average 1 hour per response, including the time for reviewing instructions, searching existing data sources, gathering and maintaining the data needed, and completing and reviewing the collection of information. Send comments regarding this burden estimate or any other aspect of this collection of information, including suggestions for reducing this burden, to Washington Headquarters Services, Directorate for Information Operations and Reports, 1215 Jefferson Davis Highway, Suite 1204, Arlington, VA 22202-4302, and to the Office of Management and Budget, Paperwork Reduction Project (0704-0188), Washington, DC 20503.

1. AGENCY USE ONLY *(Leave blank)*	2. REPORT DATE	3. REPORT TYPE AND DATES COVERED
	October 1990	Contractor Report

4. TITLE AND SUBTITLE

Computation of Rotor Aerodynamic Loads in Forward Flight Using a Full-Span Free Wake Analysis

5. FUNDING NUMBERS

505-59-36

6. AUTHOR(S)

Todd R. Quackenbush, Donald B. Bliss, Daniel A. Wachspress, Alexander H. Boschitsch, and Kiat Chua

7. PERFORMING ORGANIZATION NAME(S) AND ADDRESS(ES)

Continuum Dynamics, Inc.
P. O. Box 3073
Princeton, New Jersey 08543

8. PERFORMING ORGANIZATION REPORT NUMBER

A-91136

9. SPONSORING/MONITORING AGENCY NAME(S) AND ADDRESS(ES)

National Aeronautics and Space Administration
Washington, DC 20546-0001

10. SPONSORING/MONITORING AGENCY REPORT NUMBER

NASA CR-177611

11. SUPPLEMENTARY NOTES

Point of Contact: Ruth Heffernan, Ames Research Center, MS T042, Moffett Field, CA 94035-1000

12a. DISTRIBUTION/AVAILABILITY STATEMENT

Unclassified-Unlimited
Subject Category – 02

12b. DISTRIBUTION CODE

13. ABSTRACT ***(Maximum 200 words)***

The development of an advanced computational analysis of unsteady aerodynamic loads on isolated helicopter rotors in forward flight is described. The primary technical focus of the development was the implementation of a freely distorting filamentary wake model composed of curved vortex elements laid out along contours of constant vortex sheet strength in the wake. This model captures the wake generated by the full span of each rotor blade and makes possible a unified treatment of the shed and trailed vorticity in the wake. This wake model was coupled to a modal analysis of the rotor blade dynamics and a vortex lattice treatment of the aerodynamic loads to produce a comprehensive model for rotor performance and airloads in forward flight dubbed RotorCRAFT (Computation of Rotor Aerodynamics in Forward Flight). The technical background on the major components of this analysis are discussed and the correlation of predictions of performance, trim, and unsteady airloads with experimental data from several representative rotor configurations is examined. The primary conclusions of this study are that the RotorCRAFT analysis correlates well with measured loads on a variety of configurations and that application of the full span free wake model is required to capture several important features of the vibratory loading on rotor blades in forward flight.

14. SUBJECT TERMS	15. NUMBER OF PAGES
Helicopter aerodynamics, Free wake analysis	139
	16. PRICE CODE: A07

17. SECURITY CLASSIFICATION OF REPORT	18. SECURITY CLASSIFICATION OF THIS PAGE	19. SECURITY CLASSIFICATION OF ABSTRACT	20. LIMITATION OF ABSTRACT
Unclassified	Unclassified		